In-Situ Observation of Heavy-Oil Cracking using Backscattering Optical Techniques

By

David Dinh

A thesis submitted in partial fulfillment of the requirements for the degree of

Master of Science

in

Chemical Engineering

Department of Chemical and Materials Engineering

University of Alberta

ABSTRACT

An investigation was conducted on heavy oil cracking using polarized hot stage microscopy and laser dynamic backscattering. Both of these *in-situ* techniques were used to monitor cracking reactions through the use of backscattering. The use of hot stage microscopy resulted in a series of micrographs that were analyzed using the mean grey value (MGV). MGV is a parameter that reflects the average brightness of micrographs taken. Laser dynamic backscattering was also used and reported results using the depolarization ratio (DPR). DPR is the quotient of the parallel and perpendicular components of light after the initial incoming linearly polarized light is backscattered. Both optical techniques allowed for an examination of cracking kinetics, fouling behavior, mesophase onset and the effect of added water.

The activation energies of low conversion cracking for several feeds (Cerro Negro crude oil, Safaniya vacuum residue (VR), Cold Lake VR, Athabasca VR, Gudao VR and Columbian VR), were calculated from several experiments at various temperatures (420°C to 450 °C) using both apparatus.

Mesophase are anisotropic materials that appear as light domains on the micrographs, and were observed for all feeds given sufficient time for reaction. A second type of fouling only observed for Gudao VR and Columbian VR was dark film fouling which appeared as dark deposits and was observed before mesophase onset.

Finally, water in the range of 12.9-23.4 wt% was added to Athabasca VR to investigate if water had any effect on cracking. It was found that the added water introduces phase instability and causes Athabasca VR to exhibit dark film fouling.

Acknowledgements

First and foremost, I would like to thank Dr. William McCaffrey and Dr. Murray Gray for their supervision and suggestions during my studies. Many of the successes during this work can be attributed to their guidance as their insights greatly aided in the completion of this work.

I would also like to acknowledge Dr. Cedric Laborde-Boutet for his guidance for the development of the experimental setup. Without his training and input, the development the laser setup and execution of experiments would be greatly delayed.

I would also like to recognize Fabian Bender and Miguel Medina. Both individuals have greatly assisted in data collection of the following work. In addition, I would like to give my thanks to Sam Cardozo for his help in running the simulated distillation.

My gratitude also goes to Lisa Brandt, Jeremiah Bryska, Xiaoli Tan and Andree Koenig for all of their support in the laboratory. From helping me replenish chemicals to equipment training and day to day support, their efforts ensured for a safe workplace and allowed for a smooth journey.

To all of the staff, students and friends who have made this experience truly enjoyable and unforgettable you have my appreciation and thanks.

Finally, I would like to mention my parents who have provided with support and encouragement. I would not be here today without you and will always be here for you.

TABLE OF CONTENTS

LIST OF FIGURES

LIST OF TABLES

Chapter 1 INTRODUCTION AND THESIS OBJECTIVES

SECTION 1.1: INTRODUCTION

The U.S. Energy Information Administration predicts an average of 1.5% yearly increase in global energy demand and approximates that 70-80% of the energy is fulfilled by fossil fuels [1]. Consequently, the growing demand makes the production of unconventional oils such as those from the Alberta oil sands, increasingly more competitive in the international market. The Canadian Association of Petroleum Producers (CAPP) predicted in 2014 that the Canadian oil sands production would more than double from 1.9 to 4.1 million barrels per day by 2025 [2].

However, oils must be upgraded before it can be used as feedstock for petrochemicals or as transportation fuels. Upgrading can be categorized into two types, primary and secondary. In the former, primary upgrading is the initial step taken to increase the hydrogen to carbon ratio in the feed by heating the oil to temperatures of 420°C or greater [3]. The breaking of chemical bonds that generates smaller molecules and a lighter product is referred to as cracking and results in a viscosity reduction. Visbreaking and is normally completed without the use of a catalyst but can also employ the use of hydrogen to minimize coke formation. Due to the severe operating conditions, research is being carried out to minimize environmental impacts of these processes by reducing process severity and increasing product yield and quality.

Secondary upgrading involves catalytic hydrogenation, which results in several different classes of reactions that include: hydrodesulfurisaion, hydrodenitrogentation, hydrodeoxygenation, hydrodemetallisation and hydrogenation of unsaturated compounds [4]. Secondary upgrading processes are normally tailored to operate at less severe conditions relative to primary processes and are focused on the removal of heteroatoms. Regardless of the type of upgrading,

one area of interest is troublesome formation of toluene insoluble carbon-rich coke. Coke formation has serious detrimental effects on heavy oil extraction/upgrading processes as it can deactivate catalyst and foul pipes and process vessels resulting in costly shutdowns [3]. As such reduction in coke yield may result in significant economic benefit.

Most processes determine coke yield using ex-situ methods by collecting some sample and then sending the sample away for analysis. However, interest in the development of an in-situ detection method for coke precursors or mesophase has been expressed by industry. Mesophase is a carbonaceous liquid phase that is optically anisotropic. Mesophase is a subset of liquid crystal compounds and appears during the reactive conversion of heavy oils when temperature exceeds cracking temperatures. As a liquid crystal, mesophase exhibits both properties of crystalline solids and isotropic liquids, with unit structures that are typically around a few nanometers, are non-spherical, and have positional order and also some orientation order [5]. Mesophases' positional and orientation order give rise to its optical anisotropy making techniques like polarized light hot stage microscopy excellent for characterization. Previous work using hot stage microscopy has shown that submicron sized mesophase domains form during heavy oil cracking reactions due to oligomerization. The submicron units gradually coalesce into larger domains and ultimately deposits as coke on equipment surfaces [6]. Regardless of advances in mesophase research, there are still many shortcomings due to the multitude of reactions that can occur, variety of operational conditions, and feed compositions that can be applied. However, using polarized light as an observation tool, it is possible to observe the rate of mesophase formation as a function of temperature. As such it is possible use hot stage microscopy as technique to examine heavy oil kinetics.

Since mesophase is optically active, one method to monitor its evolution is through the depolarization ratio, which is the quotient of the intensity of the perpendicular and parallel components of backscattered light. Previous work completed using inverted bight field microscopy has approximated that the parallel component of

backscattered light remains relatively constant during cracking. However, it was found using polarized microscopy that the perpendicular intensity increases as mesophase domains appear and coalesce [6]. Unfortunately, the use of microscopy does not allow for the determination of the depolarization ratio. As such, a new technique using dynamic laser backscattering was developed to be used as a complement to the microscopy. This new technique is not be limited by optical resolution, as even the smallest domains not visible under the microscope's resolution are able to scatter light. In addition, the use of backscattering presents the opportunity for the development of a mesophase detection device that can be used in a refinery.

There has also been interest in determining the effect of water on coke induction periods. One theory proposes that asphaltene coalescences producing coke insolubles may be hindered in the presence of water [7]. As such, one question behind this investigation is the effect of water at aquathermal conditions on the growth of mesophase.

SECTION 1.2: THESIS OBJECTIVES

As mentioned, previous work in this research group has been carried out using the hot stage microscopy [6]. In summary, the objective of this thesis is to continue building on that work by aiming to:

1) Develop an experimental setup that uses laser dynamic backscattering to observe *in-situ* mesophase formation.
2) Conduct visbreaking reactions using both hot stage microscopy and dynamic laser backscattering setups.
3) Determine kinetic parameters such as activation energy of several different feeds though the use of hot stage microscopy.
4) Investigate the effect of water on mesophase formation.

Chapter 2 : LITERATURE REVIEW

The literature review begins with coverage of general topics that are relevant to this investigation. Background topics include: heavy oil composition, properties and formation mechanism of anisotropic mesophase and backscattering phenomena. A subsequent section provides a review of various investigations that examine the kinetics of heavy oil cracking reactions. Finally, a discussion with studies showcasing cracking with water is given.

SECTION 2.1 BACKGROUND

Diminishing reserves of light crude oils has forced refiners to process increasingly heavier crudes. Heavy crudes are typically defined by a °API gravity of less than 27 with extra heavy oils and bitumen having °APIs of less than 10 and are characterized by their high viscosities. Usually they are distilled to separate the more valuable products from the residue. The fraction that does not distill under vacuum which boils at 525°C or higher is known as vacuum residue. This fraction of heavy oil is the most problematic as it has the highest concentrations of heteroatoms and asphaltenes, both of which present difficulties for refining.

SECTION 2.1.1 HEAVY OIL COMPOSITION

From a process design perspective for refineries, it is often helpful to know the composition of heavy oil that is to be processed. However, the exact composition of heavy oil is difficult to obtain as it is a complex mixture comprised of very many components. Each feed has components with a large range of elemental composition, molar mass and chemical structure. As such, the task of being able to classify each individual chemical moiety becomes essentially impossible. Instead components are often broken into groups that are of similar physicochemical properties such as boiling points or solubility.

SECTION 2.1.1.1 SARA ANALYSIS

One method to characterize oil is through a SARA analysis, which separates the oil into four different classes of compounds including saturates, aromatics, resins and asphaltenes. The technique begins with the separation of the maltenes

(deasphaltened oil) from other insolubles though the use of n-heptane or n-pentane. This insoluble material is composed of mainly asphaltenes as well as carboids and carbenes. For further separation, carboids and carbenes can be removed from asphaltenes though the use of toluene and carbon disulfide as shown in Figure 2.1.

The maltenes are soluble in n-hexane, n-pentane and toluene, and can be further separated using chromatography. Silica gel adsorption can remove the resins portion of the maltenes, leaving behind oils that can be further separated into aromatics and saturates again using adsorption [8]. These three fractions are roughly divided based on their polarity, with resins being the most polar followed by aromatics and then saturates. Figure 2.1 is a schematic of the separation process for a SARA analysis which includes carbenes and carboids although these two components are not commonly isolated.

Even so, this technique does not separate components on any clear distinguishing physical or chemical properties leaving room for ambiguity. It becomes apparent then that procedure and methodology becomes very important when conducting the analysis as this can affect results. The obtained maltenes to asphaltene ratio can vary based on the feed to solvent ratio used as well as whether n-pentane or n-heptane is used as a solvent.

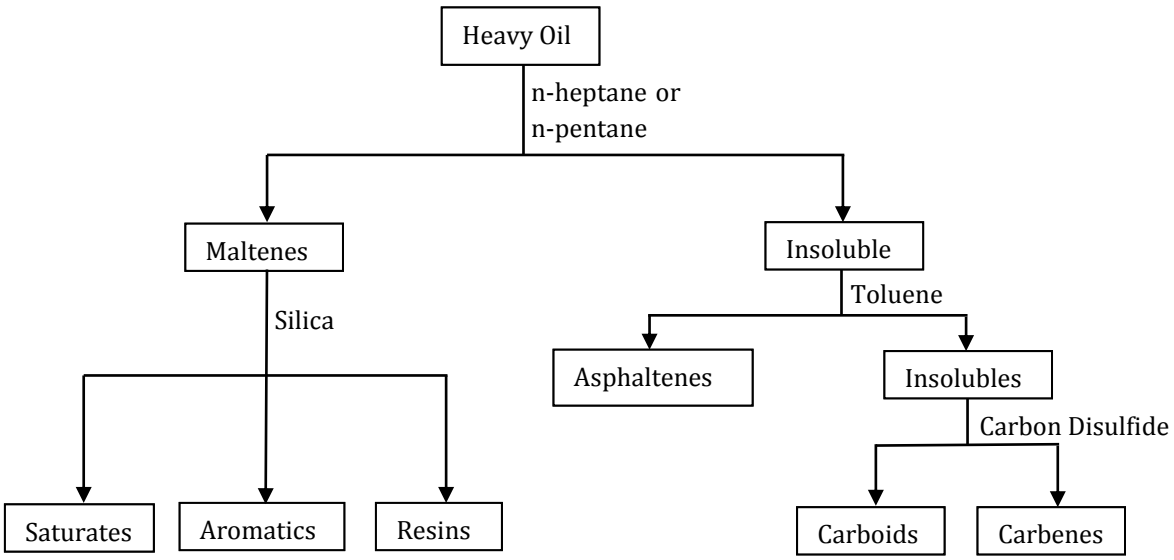

Figure 2.1: Fractionation schematic of heavy oil [8]

SECTION 2.1.1.2 ASPHALTENES

Of the SARA components, asphaltenes are the heaviest and most complex of the four fractions. As stated before due to the imprecise nature of SARA analysis, the solubility definition of asphaltenes allows for a diverse spectrum of possible molecular structures. Polycyclic aromatic hydrocarbons (PAHs) form the basic building block for asphaltenes. Other chemical moieties, however, such as polar functional groups and matello-organic compounds are also commonly found. These compounds are a group of molecules where metals such as vanadium, nickel and iron bind to organic molecules known as polphyrins. Asphaltenes are also known to be rich in heteroatoms including nitrogen, sulfur and oxygen. This broad diversity of chemical functionality, allows asphaltenes to have a large degree of heterogeneity and complexity. Although much research [8] has gone into determining representative structures for this class of compounds, there is still much debate.

There are two general motifs that have been proposed for the structural arrangement of asphaltenes. One type is an archipelago arrangement where multiple small polycyclic aromatic cores and cycloalkyl groups are linked together by alkyl bridges. It is estimated that the constituent cores contain on average of seven rings [9]. The existence of the bridges has been demonstrated though thermal cracking studies which show that they are made of paraffins or iso-paraffins and may contain sulfur atoms [10] [11]. Figure 2.2 is an example of the proposed archipelago motif. An alternative structural motif is the pericondensed model also known as a continental or island structure. This model features a single condensed aromatic core that forms the main body of the asphaltene with several alkyl pendant chains that extend out from the island. A study by Groenzin and Mullins [12] suggest that thermal treatment of such structures is likely to result in light naphthalene and heavy vacuum residue as liquid products. However, this is not the result when actually cracking asphaltenes as shown both by simulation [13] and by a thin film cracking experiments [11].

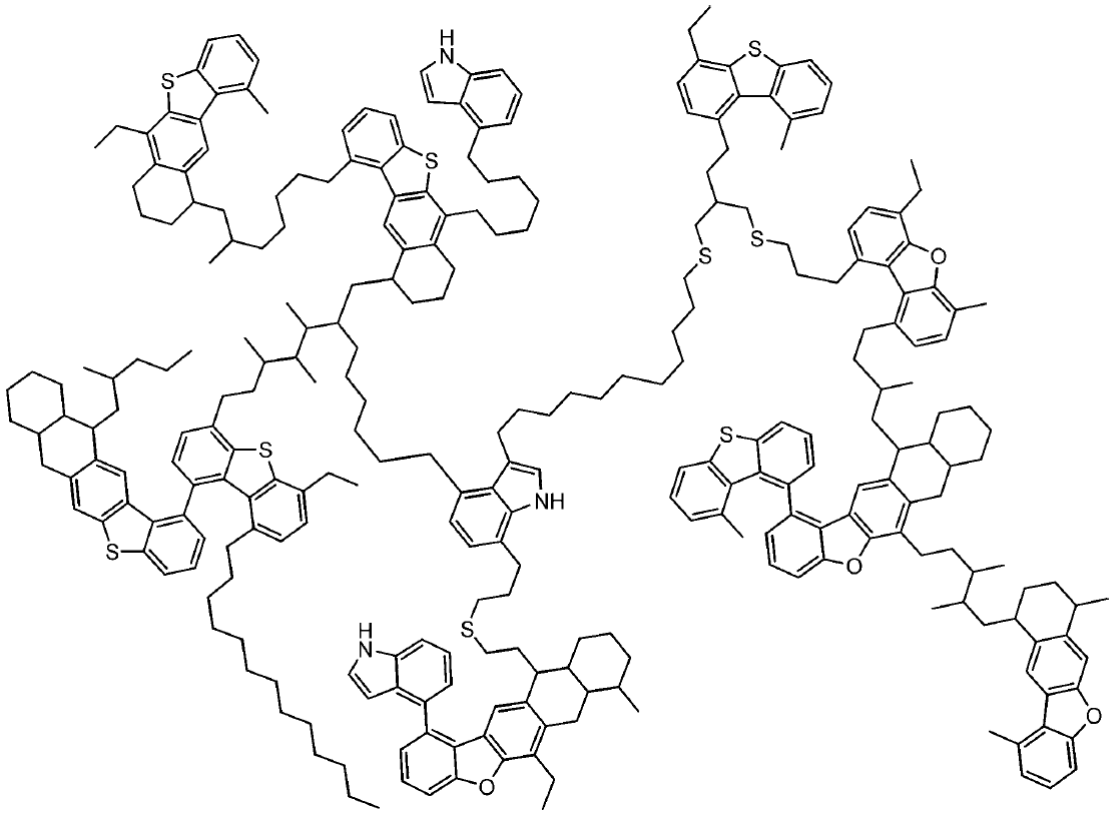

Figure 2.3: Example of an archipelago arrangement asphaltene molecule [13]

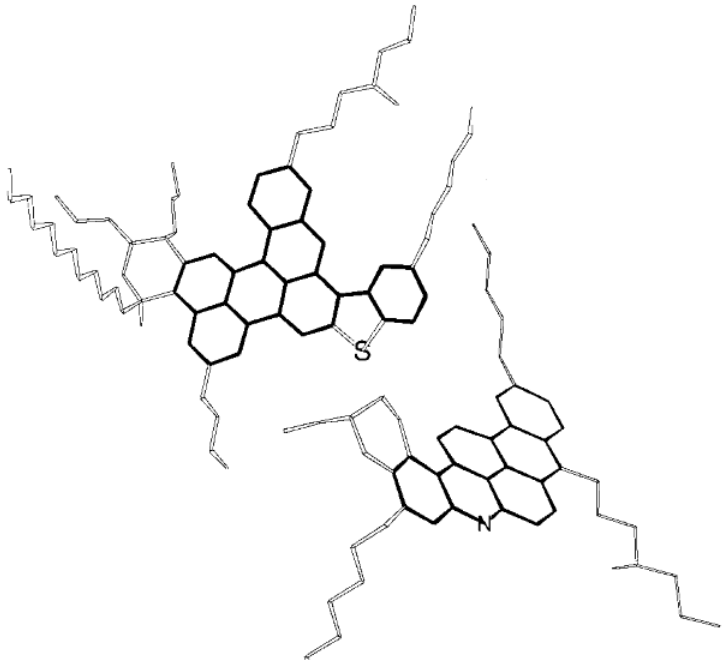

Figure 2.2: Example of a pericondensed arrangement asphaltene molecule [12]

SECTION 2.1.2 THERMAL CRACKING

The cleavage of carbon-carbon bonds to produce lighter products is achieved by thermal cracking at elevated temperatures. It is proposed that the decomposition of larger molecules is the result of free radical chain reactions [14]. These radicals are produced when sufficient energy is added to the system, which is commonly achieved by heating the oil. It has been observed that at very little reactions occur below 375°C [15]. Therefore, typical industrial operations is carried out at temperatures in excess of 400-450°C [16] [17].

The major by product from thermal cracking of oils is carbonaceous coke. One method of reducing coke formation during thermal cracking is to use hydroconversion type processes that employ catalyst and hydrogen. Hydroconversion not only provides the benefit of reducing coke formation but also several side reactions that reduces the amount of heteroatoms and metallic compounds [4]. The main industrial hydroconversion technologies involve the use of ebullated bed reactors. Although hydroconversion of heavy oil can delay coke formation, high conversion operation will still ultimately result in coke.

SECTION 2.1.2.1 COKE FORMATION

Coke is a high carbon material that is insoluble in organic solvents. Although in general coke has found its use in aluminum and synthetic graphite production, cokes from heavy oil processing has relatively high contaminant levels and as a result has relatively low value when compared to other products [18]. In addition to reducing liquid yield, coke formation also has serious detrimental effects on heavy oil upgrading processes because it can deactivate catalysts, foul pipes and heat exchangers [6]. The removal of coke from equipment is often done during process shutdowns though physical means such as manual labor, cable or hydraulic removal [18].

Formation of carbonaceous coke is speculated to be a result of liquid-liquid phase separation. Abedi *et al*. [19] were able to produce a phase diagram using Athabasca tower bottoms, dodecane and hydrogen. It was shown that the system traversed reversibly between a liquid-vapour to a liquid-liquid-vapour system where the

heavier liquid phase appeared and disappeared within the light liquid phase based on the temperature and pressure. At temperatures of 385°C and higher there is an irreversible precipitation from the heavier liquid phase. They suggest that multiphase behavior has some correlation with asphaltene precipitation.

A liquid-liquid phase separation kinetic model proposed by Wiehe [20] explains that free radicals during cracking break the side alkyl chains from the poly nuclear aromatic cores of asphaltenes. The free radicals are terminated by abstracting hydrogen from the aromatics in the residue, which in turn results in an increase in the number of cores while decreasing the available maltenes. Eventually there is an insufficient amount maltenes to solvate the cores and these cores precipitate out of solution. The time it takes for this precipitation to occur is often referred to as the onset period.

SECTION 2.1.2.2 MESOPHASE A SUBSET OF COKE

The solubility definition of coke gives rise to a diverse range chemical species. From a physical perspective it is possible to categorize coke into sub-phases. One classification is carbonaceous mesophase which is defined by its anisotropy and has been discovered to exist in petroleum pitch as shown in studies by Brooks and Taylor [21]. This unique property allows for the detection of such species using light scattering techniques covered in subsequent sections [6]. Carbonaceous mesophase has found its use in the production of high performance carbon fibers [22], unfortunately the mesophase formed during upgrading is of low quality and cannot be used for such an application.

Mesophase which may also be referred to as liquid crystals or anisotropic liquids are an intermediate phase that possesses properties of both a crystalline solid and an isotropic liquid. This state of matter is characterized by the ability to flow like a liquid, but unlike a conventional isotropic liquid that has no long range order, mesophase exhibit some optical anisotropic properties reminiscent of a solid. The term may also be adopted for biological structures that have defined order such as layers in a cell membrane. Thus, the term carbonaceous mesophase is used to

distinguish mesophase that is derived from the thermal treatment of petroleum pitch. For simplicity, carbonaceous mesophase will just be referred to as mesophase for the remainder of this thesis.

Section 2.1.3 Liquid Crystals

In the later part of the 19th century, Austrian botanist Friedrich Reinitzer noticed that cholesteryl benzolate exhibited two different melting points [23]. The solid substance would initially melt into a cloudy liquid and then into a clear one upon further heating. This behavior was unexpected as melting of crystalline solids were expected to directly result in an isotropic liquid. The phase transition from a solid into a liquid crystal results in loss of translation order while maintaining some orientation order as shown by Figure 2.4.

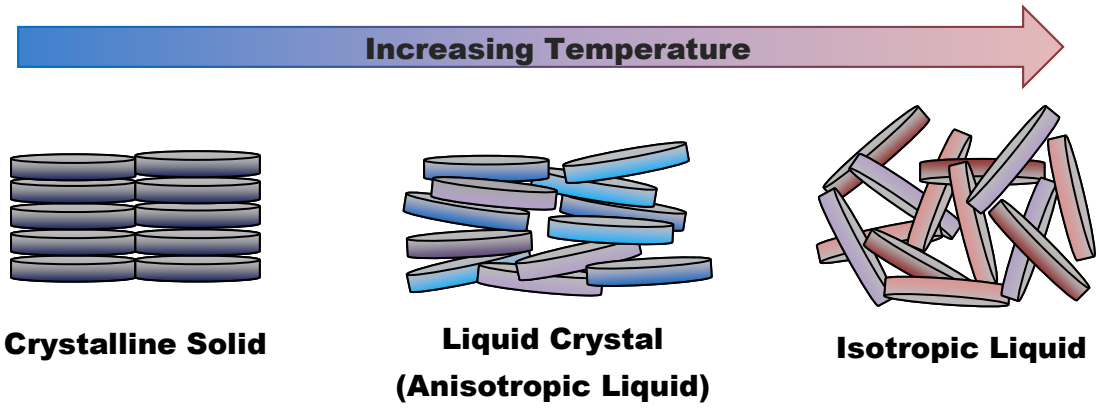

Figure 2.4: Phase transition behavior of a liquid crystal

Liquid crystal unit structures or mesogens have two important properties, the aspect ratio and their flexibility. A sufficiently large aspect ratio is one defining characteristic that results in a non-spherical unit structure that may possess orientation order. It is also important that the mesogens contain both ridged core(s) and flexible tail(s) [5]. Molecules that are completely ridged will become an isotropic liquid directly. Conversely, unit structures that are fully flexible will not be able to maintain orientation order. Due to non-spherical unit structures, the orientation position of each mesogens can be described by a direction vector. Liquid crystal attain their unique optical anisotropic properties relative to an

isotropic liquid, due to the tendency for the directional vector of each individual mesogen to align in a particular direction [24].

Section 2.1.3.1 Liquid Crystal Classification

Liquid crystal phenomenon can be induced in a variety of ways. One possibility is the addition of heat to a crystalline solid or the removal in the case of an isotropic liquid. When changes in heat are used to induce liquid crystal behavior it is referred to as themotropic. There are also substances where liquid crystal formation is observed as solvent in added in an isothermal manner, in which then the behavior is referred to as lyotropic [25]. Finally, amphotropic behaviors are for cases where liquid crystal transition is influence by both temperature and solvent concentration [26].

Mesogens also come in two varieties. In the case depicted by Figure 2.5A the unit structure is rod shaped and is termed calamitic mesogens. Unit structures may also appear be discotic if they are disked shaped as depicted in Figure 2.5B [5].

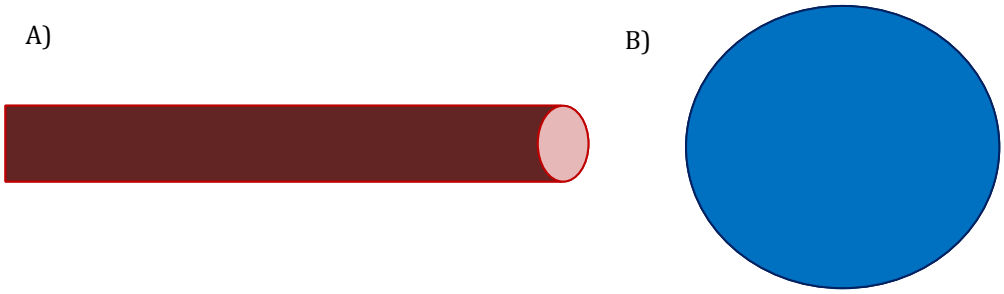

Figure 2.5: Example molecules of (A) calamitic and (B) discotic mesogens [5]

Section 2.1.3.2 Liquid Crystal Phases

Anisotropic properties of liquid crystals are a result of their direction vector which arises from the unified tendency for the mesogens to align. Several liquid crystal phases can be distinguished based on amount of anisotropy that is encountered [27]. For calamitic mesogens, rods that points along a direction vector with no positional order are referred to as a nematic phase. Calamitic mesogens that also present translational order, such as the rearrangement of the unit structures into layers, possess a higher degree of orientation resulting in a semetic phase. Sometimes

calamitic mesogens are not only organized in layers, but additionally have a chiral center where each layer is slightly rotated relative to the layers around it. This type of order is known as a cholesteric phase or a chiral nematic liquid crystal. Discotic mesogens tend to stack in columns resulting in a columnar phase. Visual representation of each type of liquid crystal phase described is shown in Figure 2.6.

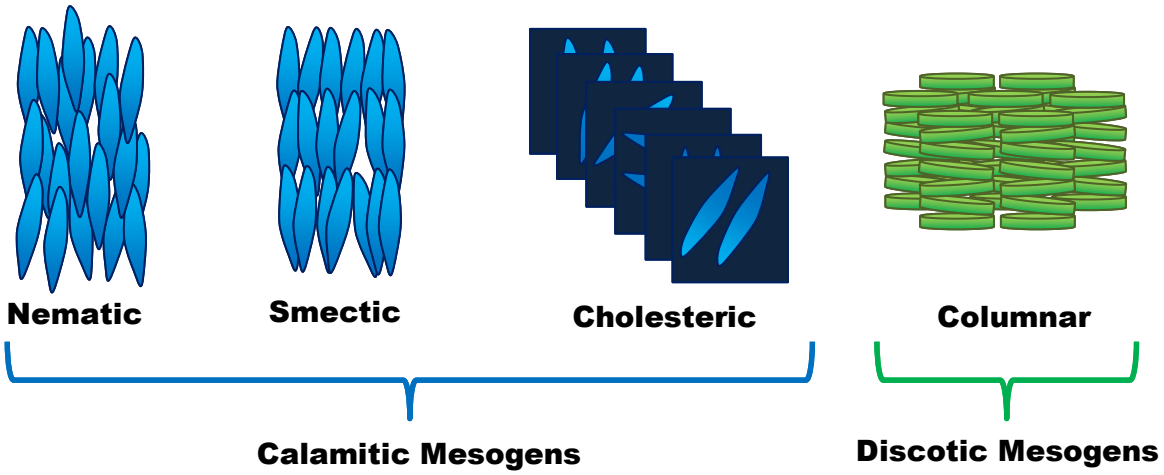

Figure 2.6: Various liquid crystal phases

Section 2.1.4 Polarized Light Techniques

One of the defining qualities of a liquid crystal is its anisotropic nature. Although liquid crystals contain orientation order to a lesser extent, it is possible to use characterization techniques such as transmitted polarized light microscopy or polarized light backscattering for detection.

Visible light is an electromagnetic wave with wavelengths between 380-750nm. As an electromagnetic wave, light is composed of perpendicular electric and magnetic field that oscillate as it propagates forward [28]. To simplify drawings, only the electric field vector is shown in subsequent figures as it is known that the magnetic field is always perpendicular to this component. Natural light from sources such as the sun or light bulbs is not polarized meaning that the electric field component is vibrating in all directions. A polarizer is used to produce linearly polarized light, as it extinguishes all light except for the rays that vibrate

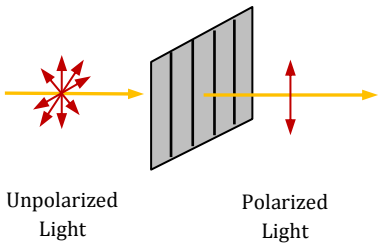

Figure 2.7: Polarization of natural light

parallel to the polarizer's optical axis as shown in Figure 2.7

Materials that are anisotropic such as liquid crystals have refractive indices that are dependent on the polarization of the light [29]. Light that is parallel to the crystal axis (vector direction) will behave differently to light that is perpendicular to the director [30]. Thus, resulting in the double refraction where an entering ray of light splits into two wave fronts. The polarized ray that is perpendicular to the director is known as the ordinary ray and follows Snell's law of refraction [28]. The secondary ray polarized parallel to the director is termed the extraordinary ray. Both the extraordinary and ordinary rays are each subjected to their own index of refraction resulting in different rates of propagation though the anisotropic material. Consequently, when the rays exit the material they will no long be in phase with each other and the polarization state of the light is changed as shown in Figure 2.8. This double refraction phenomenon is known as birefringence.

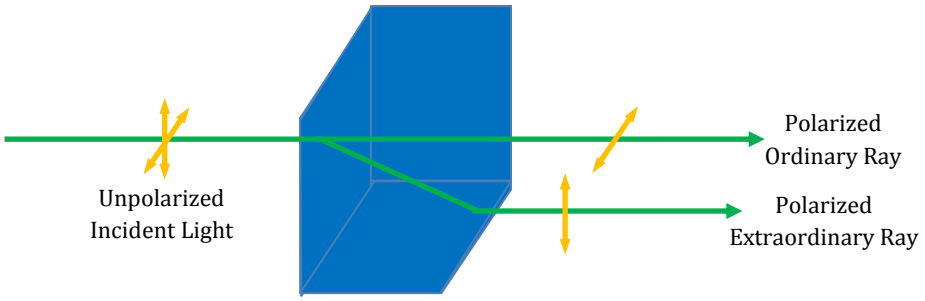

Figure 2.8: Double refraction phenomena due to birefringence

SECTION 2.1.4.1 DETECTION OF ANISOTROPIC USING POLARIZED LIGHT

Using the concept of birefringence, one possible method of detecting the presence of anisotropic materials is the use of a linear crossed polarizer and analyzer [31]. In the event where two polarizers are set up in series and with their optical axis perpendicular to each other, the light which is linearly polarized by the first is completely extinguished by the second polarizer. The placement of an isotropic material in between the two polarizers will not change the polarization of the incoming light. This means that light leaving the sample will be extinguished as it passes through the second polarizer as illustrated in Figure 2.9.

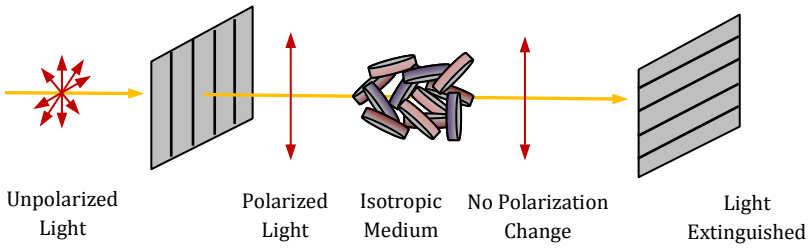

Figure 2.9: Cross polarized setup for an isotropic medium

Anisotropic materials that are placed in between the series of polarizer will change the polarization of the light as it passes through the medium (Figure 2.10) [32]. The change in polarization results in only partial light extinguishment when it passes through the second polarizer allowing for detection. Extra caution must be applied if the direction vector of the liquid crystal is parallel with the polarization of the incoming light. In this scenario, polarization of the incoming light is not changed as it passes thru the material and thus results may indicate a false negative when in actuality the material is anisotropic.

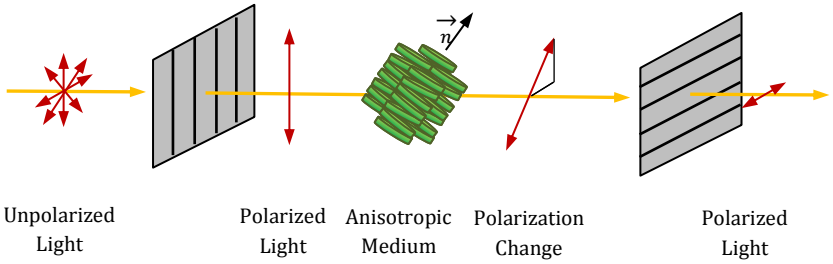

Figure 2.10: Cross polarized setup for an anisotropic medium

SECTION 2.1.4.2 DEPOLARIZATION OF LIGHT SCATTERING

With the knowledge that anisotropic materials can change the polarization of light, the use of depolarization light backscattering becomes a powerful technique that can be used for analysis of mesophase. This technique is conducted through utilization of a linearly polarized light that is focused on a sample. Particles in the sample scatter the light. The backscatter light is collected for subsequent analysis. Stokes parameters can be used to fully characterize electromagnetic radiation though the use of four parameters that describe the polarization as shown by the Stokes vector [33].

$$I = \begin{bmatrix} I \\ Q \\ U \\ V \end{bmatrix} \ (Eq.\ 2.1)$$

The first three parameters I, U and Q are designated for the linearized polarization state while the fourth variable V expresses the circular polarization. Since incoming light in this experiment is linearly polarized, the Stokes vector simplifies into Equation 2.2.

$$I^0 = \begin{bmatrix} 1 \\ 1 \\ 0 \\ 0 \end{bmatrix} \ (Eq.\ 2.2)$$

It is possible to transform the Stokes vector into a 4x4 matrix that can describe scattered light function of scattering angle [34]. Assuming that the studied sample is composed of randomly oriented particles with symmetrical planes of symmetry, the scattering matrix that is given by:

$$f(\theta) = \begin{bmatrix} f_{11}(\theta) & f_{12}(\theta) & 0 & 0 \\ f_{12}(\theta) & f_{22}(\theta) & 0 & 0 \\ 0 & 0 & f_{33}(\theta) & f_{34}(\theta) \\ 0 & 0 & -f_{34}(\theta) & f_{44}(\theta) \end{bmatrix} \ (Eq.\ 2.3)$$

Although particles may scatter light in all directions, only the backscattered light is collected and as such, the angle of interest is 180°. This particular scattering direction transforms the scattering matrix into a simplified version and is given by Equation 2.4.

$$f(180°) = \begin{bmatrix} f(180°) & 0 & 0 & 0 \\ 0 & f_{22}(180°) & 0 & 0 \\ 0 & 0 & f_{33}(180°) & 0 \\ 0 & 0 & 0 & f_{44}(180°) \end{bmatrix} \ (Eq.\ 2.4)$$

The degree of depolarization of the backscattered light is captured by the linear depolarization ratio, δ. It is the quotient of the perpendicular and parallel intensity of the backscattered light with the parallel component having the same linearized

polarization state of the initial incoming light. The depolarization ratio can also be written in terms of the backscattered matrix elements as shown below.

$$\delta = \frac{I_{\perp}}{I_{\parallel}} = \frac{f_{11}(180°) - f_{22}(180°)}{f_{11}(180°) + f_{22}(180°)} \ (Eq. 2.5)$$

For spherical isotropic particles there is no depolarization, as the backscattered light has the same orientating as the incident light [35]. Molecular backscattering of various molecules has been studied and it was shown that spherical particles have a very low depolarization ratios. Deviation from sphericity such as the addition of planar aromatic molecules greatly increases the depolarization ratio.

Section 2.1.5 Mesophase Formation Mechanism

Brooks and Taylor [21] used polarized microscopy to find that the initial heating of hydrocarbon pitch resulted in a dark liquid isotropic material. Small light anisotropic domains were found at higher temperatures, which gradually became more numerous and larger in size during prolonged heating. Eventually the spheres grew to such a size that further enlargement was hindered. Micrographs taken at this point show a mosaic texture. Similar behavior was also observed by Bagheri *et al.* [36]. Based on these observations, it was proposed that during the cracking of crudes, single aromatic molecules oligomerize to form larger planar polyaromatics. Eventually the planar units grow into clusters and submicometer domains. Continual growth results in domain sizes large enough to be observable under optical microscope resolution and further coalescence produces bulk mesophase that appear as a mosaic as described by Taylor and Brooks. The proposed mesophase formation mechanism is depicted in Figure 2.11.

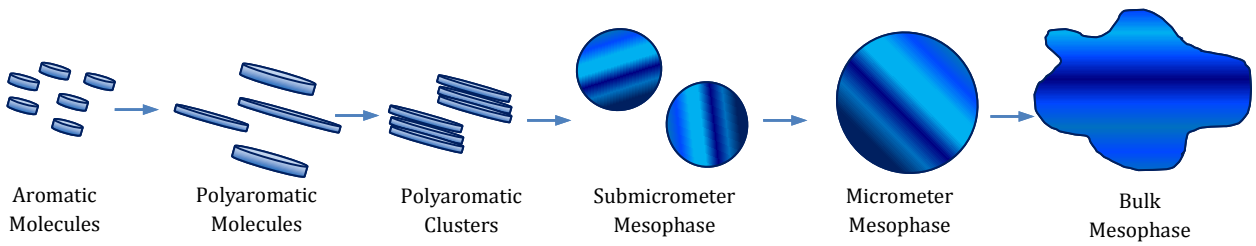

Figure 2.11: Bagheri *et al.*'s proposed mechanism for mesophase formation and growth [36]

Bagheri`s later work continued to develope this concept by using depolarized scattering to study mesophase formation [37]. Experiments with vacuum residue at 435°C and at 4.1MPa were completed. Micrographs from polarized microscopy were taken throughout the experiment. Image analysis of the micrographs showed that once the reaction temperature was reached, the intensity of the backscattered light progressively decreased with increasing reaction time. This darkening was attributed the initial steps of the proposed mechanism in Figure 2.11 where aromatic molecules are rearranged in larger polyaromatics and clusters. This phenomenon reduces the number of scatters and thus the amount of backscattered light. Eventually the appearance of bight mesophase domains was observed. Brightness of these domains under polarized light is associated with the anisotropic nature of liquid crystals.

In a related field, the carbonization of coking coals was also investigated by Marsh [38]. It was seen that during the heat temperature treatment, sematic liquid crystals were formed. Four different types of mesophase growth were observed:

1. Mesophase spheres form and grow in size while maintaining consistent uniformity.
2. Mesophase spheres originate at different times resulting in a distribution of possible sizes.
3. Mesophase initiates uniformly but stay small in size and do not grow.
4. Mesophase formation can be influenced by the presence of solids. Smaller solids can interfere with mesophase coalescence, reducing formation rate. Larger solids have a tendency to increase the size of domains of coalesced material.

Another study by Hu and Hurt [39] suggested that structural features of polycyclic aromatic hydrocarbons strongly influence mesophase behavior. This was examined by determining the theoretical clearing temperature, which was the maximum temperature a nematic liquid crystal phase can exist. It was suggested that pure aromatic molecules that have melting points that are higher than the clearing

temperature are not likely to exhibit liquid crystal behavior. Simulation of binary systems results, however, shows that multicomponent mixtures do have the tendency to form liquid crystals even if the clearing temperatures of each component in the mixture are below the melting points of several of the individual components. Shishido *et al*. [40] developed phase diagrams for mixtures benzene soluble and insoluble pitches at different ratios and developed a model using liquid crystal theory to predict their phase boundaries. Hurt and Hu expanded their previous study by combining theirs with Shishido *et al*. and successfully produced a model that predicted mesophase formation by applying liquid crystal theory with Flory-Huggins theory [41].

It is interesting to note that the mesophase onset can be changed with the addition of carbon additives as shown by Gentzis *et al*. [42]. When solid coke was added to Athabasca bitumen, bulk fluidity increased allowing for faster coalescence, thus reducing onset time. Conversely, onset time was extended when fullerene soot was mixed in. It was rationalized that the fullerene`s pore structure was able to absorb mesogens which also was accompanied by a marked increase in viscosity of the bulk phase.

SECTION 2.2 KINETICS LITERATURE REVIEW

Thermal cracking is a fundamental process for converting heavy oils into lighter product through homolytic bond scission. This process is used in visbreaking, delayed and fluidized coking, and the hydroconversion reactors. By doing so, high viscosity and pour points are reduced making the feeds easier to process, and ultimately produce higher value middle distillates and light fuels. Thermal cracking can be differentiated from catalytic cracking which employs the use of catalyst. For the remainder of this thesis, cracking will be used to exclusively refer to thermal cracking.

Cracking is proposed to occur though free radicals chain reactions [14]. The radicals are produced though cleavage of primarily carbon-carbon bonds when enough energy is added to overcome bond dissociation energy. A less common method that is used for initiation is the addition of a radial initiator as shown by Chang *et al*. [43].

Radical species continue to propagate though several classes of reactions such as hydrogen abstraction where a hydrogen free radical is taken from substrate. Radical decomposition, when the radical decomposes into an alkene and hydrogen radical. β-scission is when free radicals decompose into a smaller alkene and smaller radical. Radical addition, on the other hand, is when a radical combines with an alkene to form a larger radical. β-scission and hydrogen abstraction primarily dominate during cracking.

Radicals are terminated when two radicals combine to produce a larger alkane during recombination. Termination may also occur due to disproportionation where a hydrogen atom is relocated from one radical to another resulting in an alkane and alkene. The examples below are generalized forms of each of the aforementioned reaction types. Propagation reactions are considerably faster than the both initiation and termination reactions. A summary of the free radical propagation is given in Table 2.1.

Table 2.1: Free radical propagation of thermal treatment of crude oil

Reaction Class	Generalized Example
Initiation	
Homolytic Cleavage	$n_1 - CH_3CH_3 - n_2 \rightarrow n_1 - CH_3^{\cdot} + n_2 - CH_3^{\cdot}$
Propagation	
Hydrogen Abstraction	$n_1^{\cdot} + n_2 \rightarrow n_1 + n_2^{\cdot}$
Radical decomposition	$n_1CH_3^{\cdot} \rightarrow n_1 = CH_3 + H^{\cdot}$
β-scission	$n_1^{\cdot} \rightarrow n_2 = n_3 + n_4^{\cdot}$
Radical Addition	$n_1^{\cdot} + n_2 = n_3 \rightarrow n_1 - n_2 - n_3^{\cdot}$
Termination	
Recombination	$n_1 - CH_3^{\cdot} + n_2 - CH_3^{\cdot} \rightarrow n_1 - CH_3CH_3 - n_2$
Disproportionation	$n_1 - CH_3CH_3^{\cdot} + n_2 - CH_3^{\cdot} \rightarrow n_1 - CH_3 = CH_3 + n_2 - CH_4$

Due to the sheer amount of chemical species available for reactions and the variety of reaction classes available, the development of true kinetics for each and every individual molecule would be impossible. To simplify the problem, many studies adopt the use of pseudo components and lumped kinetics. Pseudo components are groups of compounds that are divided based on similar physicochemical properties such as boiling point, volatility, molecular weights, etc. Using pseudo components many lumped kinetic models were developed. These models can further be categorized into parallel reaction models or parallel-consecutive reaction models. In addition, more recent work has focused on the development of continuous models using probability distribution functions.

Section 2.2.1 Parallel Models

Parallel models are characterized by feed conversion into a set of product(s), with the assumption that these product(s) do not undergo further reaction. Although this assumption is crude, it can greatly simplify modeling work as shown by some of the following works.

A visbreaking study by Al-Soufi *et al*. [44] was conducted in a soaker-type reactor with temperatures ranging from 435 to 480°C at 1.7 MPa and residue times of 151-379 seconds on Iraqi residue. Cracked product was defined at any cut that boiled below 350°C. At operating conditions it was found that the thermal treatment fell

under a first order regime with activation energy of 99.1 kJ/mol. The lower activation energy is the result of very short residence times.

Carlos and Janis [45] also found after testing three different residues (Rospo di maren Belaym, Es Eider) that the visbreaking kinetics again exhibited apparent first order kinetics. Using a similar kinetic model to Al-Soufi *et al*. [44] it was found that the activation energies for the Es Eider, Belaym and Rospo di mare residue were 329.7, 284.5 and 130.6 kJ/mol respectively. They concluded that feedstocks rich in asphaltenes, resins and polar compounds showed higher kinetic constants at lower temperature relative to temperatures typically used in industry. Furthermore, thermal treatment of asphaltene rich crudes favors dealkylation resulting in higher selectivity towards gas. In contrast, paraffinic feeds are dominated by scission reactions yielding more gasoil relative to gaseous products. The authors attributed cracking effectiveness of thermal treatment with larger differences in the aromaticity of the asphaltene and maltene phases.

Aghajari atmospheric residue was used in a continuous reactor by Krishna *et al*. [46] at a pressure of 1.7 MPa with temperatures between 427 to 500°C. Residue time of the feed was controlled by the inlet flowrate. It was concluded that there were two regimes of reaction, with the first occurring when the conversion is below 7% where dealkylation predominates. This process sharply reduces the viscosity of lighter distillates while minutely increasing the viscosity of heavier components. Higher conversions in the second stage are dominated by condensation and polymerization reactions, which results in a dramatic increase in viscosity of the heavier distillates.

The kinetic models presented by Al-Soufi *et al*. [44], Carlos and Janis [45] and Krishna *et al*. [46] lumped reacted products into a single pseudo component. The difference between each study is the chosen maximum boiling point that defined which cut would be considered as product, as shown in Figure 2.12A.

Using a microstatic reactor designed for 400-500°C, Xiao *et al.* [47]used a 12 lumped reaction model for product distribution for the visbreaking of heavy oil. It was assumed that all cracking and condensation reactions are first order and that, once reacted there are no secondary reactions. The final product distribution is broken down into lumped distillation cuts are shown in Figure 2.12C, with the activation energy determined to be 274.8 kJ/mol.

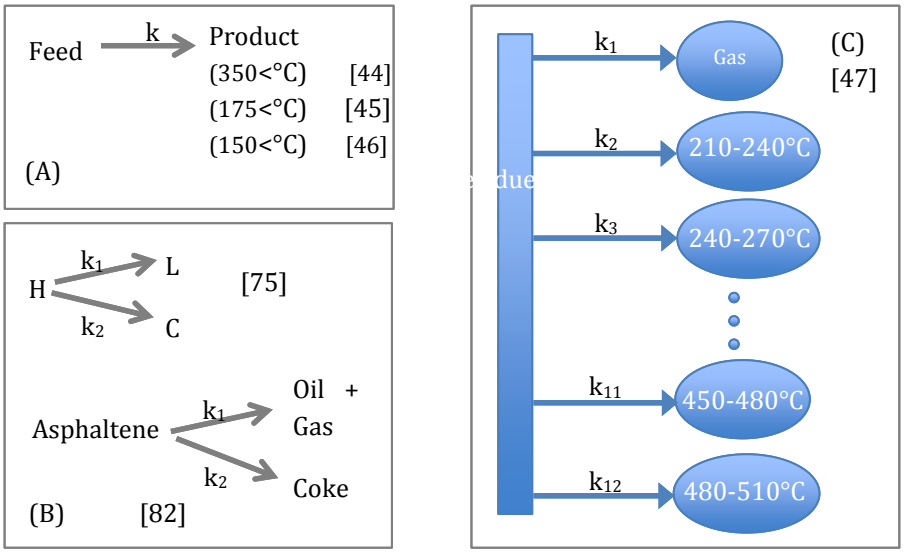

Figure 2.12: Various parallel kinetic models

SECTION 2.2.2 PARALLEL CONSECUTIVE MODELS

Relative to parallel models, parallel consecutive models allow for reacted products to undergo further reaction. This means that middle distillate products may continue to break into lighter components. Conversely, reacted components are also able to oligomerize into larger constituents. This added complexity allows for more flexibility in modeling that is likely to be more realistic, although at the cost of an increased number of variables.

Trauth *et al.* [48] reacted Hondo and Maya vacuum residues and their extracted asphaltenes at temperatures from 400 to 450 °C in a batch reactor with residue times ranging from 20 to 180 minutes. Using solvent extraction and thermogravametic analysis, they were able to resolve reacted components into: gases, coke, maltenes and asphaltenes. Figure 2.13 shows their proposed reaction

cracking mechanism and the kinetic parameters that were determined. The authors evaluated both first and second order models and found that the first order parameters were much better at capturing the reaction phenomenon.

Yasar *et al* [49] continued this work, using Arabian heavy residue and Arabian light residue in addition to the Hondo and Myan VR. They found that all of the isolated asphaltenes from the samples selectively reacted to maltenes between 400 and 425°C due to dealkylation reactions. At 450°C the rate of maltene formation was highly dependent on initial aromaticity.

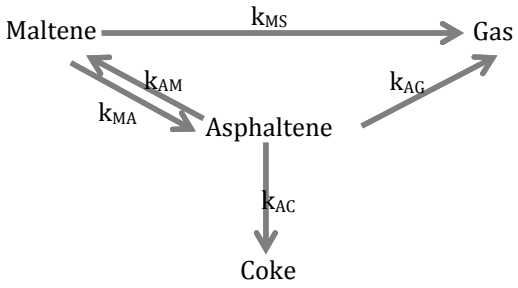

Figure 2.13 Kinetic model of Trauth *et al*. and [48] Yasar *et al*. [49]

Using Middle Eastern residues, Kataria *et al*. [50] developed a five lumped model based on the highest value added products: gas, gasoline, light gas oil and vacuum gas oil as shown in Figure 2.14A. The study used five vacuum residues, North Gujarat Residue, Bombay High Residue, Arab Mix Residue, and Visbreaker Mathura feed, and two asphalts, Haldia Asphlt and AM Asphalt. It was assumed that cracking kinetics fell under a first order regime. A five parameter model for low severity cracking for vacuum residue times of up to fifteen minutes for a temperatures range of 400 to 430°C was developed. Initial pressure was kept constant throughout the experiment at 1.2MPa using nitrogen. As these runs were low severity, no coke formation was observed and as consistent gas compositions were obtained regardless of feed used. However, the maximum conversion was directly related to the asphaltene content, with the feed stability decreasing with increasing conversion. It was also found that while gas, gasoline and light gas oils fractions were stable, vacuum gas oil underwent significant cracking at higher severity. Using

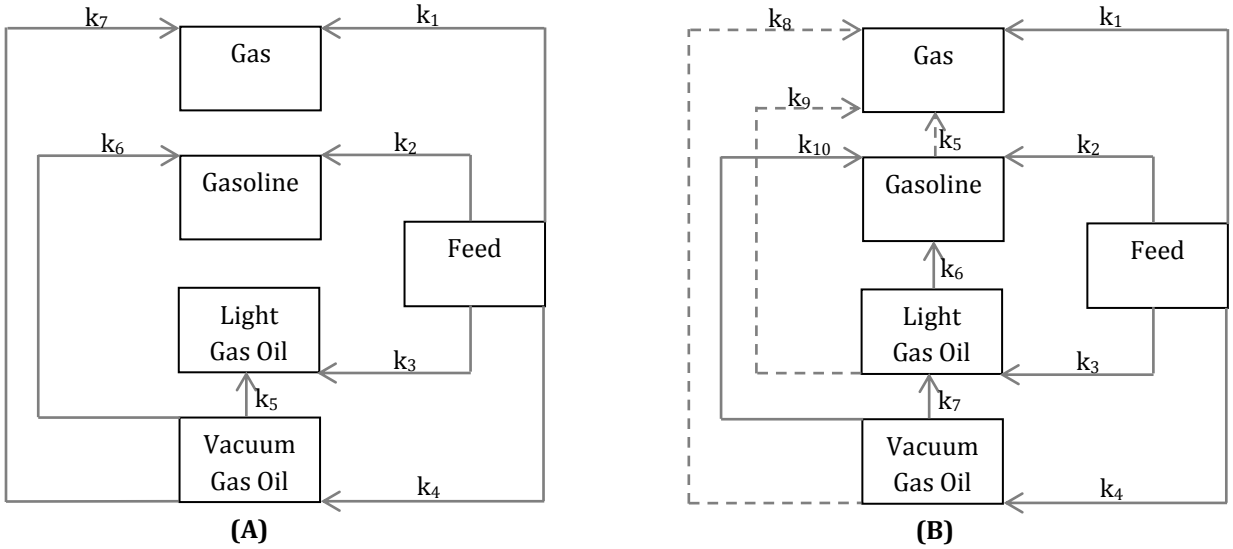

Figure 2.14: A seven parameter kinetic model as use by Kateria *et al.* (a) [50] and Singh *et al.* (b) [51]

their data they were able to accurately model the kinetic behavior with only seven parameters as shown in Figure 2.14A. The modeling shows that produced VGO was able to further react to produce lighter components of the other lumped classes.

Singh *et al*. [51] used several of the same feeds as Kataria *et al*. [50], and operated at similar temperatures and residue times of 400°C to 430°C and 3 to 15 minutes respectively and also used five lumped classes in their model. Initially, their model was significantly more complex as compared to Kateria's model as shown in Figure 2.14B. However, upon further analysis it was found that their results were still modeled effectively with seven kinetic parameters. As such, k_8, k_5 and k_9 were found to be negligible as shown by the dotted lines in Figure 2.14B. For low severity reactions it was found that gases are not likely from gasoline, LGO or VGO. Instead the bulk formations of gases were created directly from of the feed material. Deviation from this behavior was expected at higher severities. Regardless, the authors concluded that all reactions for each parameter follow first order kinetics. However considering both studies used similar feeds, and operating conditions there is discrepancy between these two proposed models, but this this is likely due to the nature of the modeling. Even if the proposed kinetic models are slightly different, both models had some reactions that converted heavier products into

lighter products. As long as there is any reactions that can account for conversion, it is likely that there are other combinations of seven kinetic parameters models that are able to accurately capture the experimental results.

Another parallel consecutive model proposed by Takatsuka *et al*. [52] was aimed at being able to capture the condensation and polymerization of residue while the feed was cracked. This was carried out by taking into account the degree of aromatization and polycondensation of the residue which was measured by changes in the solvent-insoluble content as reflected by their model shown in Figure 2.15.

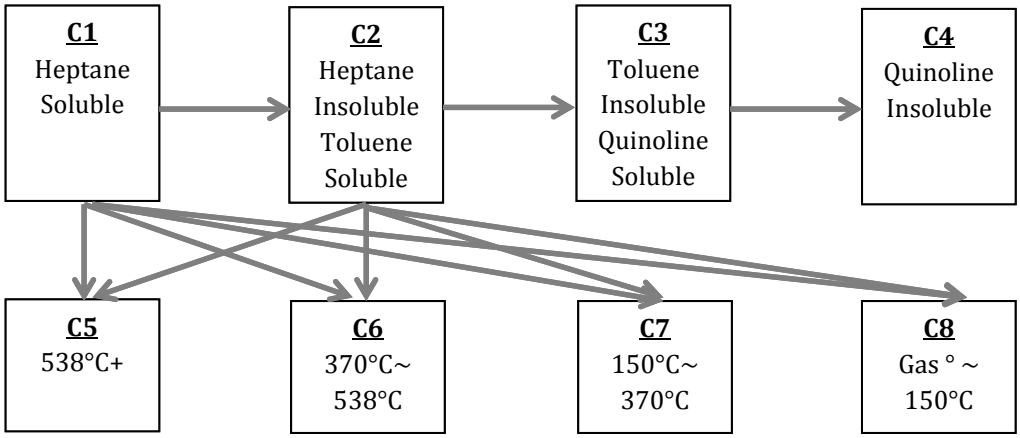

Figure 2.15: Eight lumped model as proposed by Takatsuka *et al.* [52]

Experimental results determined that the polycondensation reactions proceeds by consecutive reactions results in higher amount of quinolone insoluble products at longer residue times. In addition, hydrocarbon partial pressure can slow condensations reactions while conversion is increased with increasing reactor pressure. The study estimated 251 kJ/mol for cracking reactions and 40 to 50 kcal/mol for condensation reactions.

Working with Daqing, Tube-Trans and Liao He residue, Zhou *et al*. [53] used solvent fractionation to separate each residue into saturates, light/heavy aromatics, soft/hard resins and asphaltenes. Each separated class was reacted separately in a batch reactor at temperatures of 400 to 460 °C with residence times of up to 90 minutes. The thermal behavior of each separated fraction was examined alone

resulting in a reaction network that can capture any inter-conversion behavior as shown Figure 2.16 for the case of saturates.

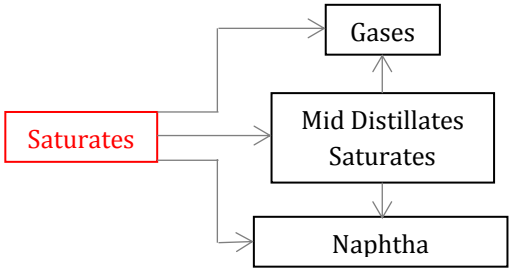

Figure 2.17: Reaction network for saturates [53]

Eventually all six of the feeds classes were tested and combinations of all of the networks resulted in a complex model as shown in Figure 2.17. The reaction scheme contains 11 lumped species as shown in the diagram. Colored species are the initial reactants, while the black species are the resulting products due to thermal cracking. They found that the kinetic parameters of the separated components were independent of the initial unseparated residue. Thus, the final overall product composition tends to be the sum of products of each individual reactant class. This conclusion seems valid, because even if the ratio of the six separated classes (saturates, light/heavy aromatics, soft/hard resins and asphaltenes) may vary from residue to residue, the behavior of the individual class of compounds should be similar regardless of the residue they were obtained from since they were separated based on their solubilities.

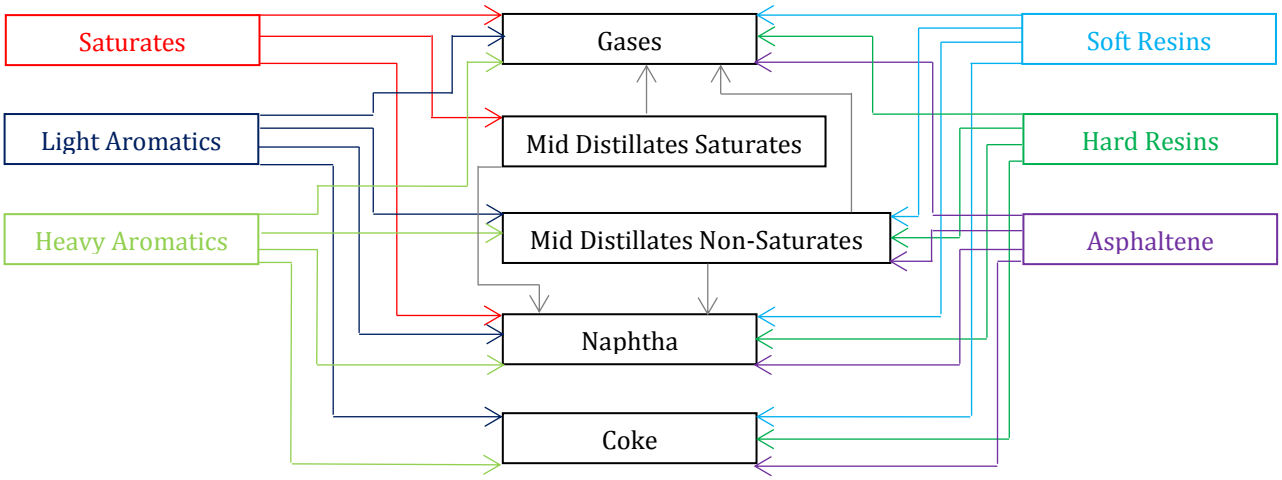

Figure 2.16: Combined reaction networks of all separated classes [53]

Section 2.2.3 Continuous Models

The majority of literature reports fitted first order parameters to a kinetic model with lumped discretized residue cuts. Shadbhahr *et al*. [54] developed a continuous kinetic model that uses probability distribution functions that are tunable using five parameters. Using a normalized boiling point curve, each feed was modeled as a continuous mixture with a concentration distribution that would evolve as the reaction progressed. The data extracted from literature at temperatures of 400 to 430 °C was applied to show that their model was able to match experimental data with reasonable accuracy. Equation 2.6 is their generalized rate expression for the changes in concentration of any species as a function of time.

$$\frac{dc(k,t)}{dt} = -kc(k,t) + \int_{k}^{k_{max}} p(k,K)\,Kc(k,t)D(K)dK \quad (Eq.\,2.6)$$

Where: c is the concentration of the component at a given reaction activity of k; p is the yield distribution for the formation of a component at a given k; D is the species type distribution. Although the works of Shadbhahr *et al*. models the oil as a distribution, there are other works such as those of Montane *et al.* [55] that even goes as far as modeling the activation energy of the oil as a distribution rather than a single value. From a modeling perspective, the use of probability distribution is likely to be the most accurate approach, but is not experimentally practical because it is essentially impossible to fully capture oil behavior as a distribution with current techniques and practices. Consequently, as presented in Section 2.2.1 and 2.2.2, the use of lumped kinetics is commonly applied in lieu.

SECTION 2.2.4 KINETICS SUMMARY

Kinetic studies on petroleum residue are a difficult task as feed compositions can vary greatly and have a multitude of possible and unmeasurable chemical species. Consequently, this problem is dealt with by lumping components into pseudo components of similar physicochemical properties such as boiling point or solubility. At this point the problem becomes greatly simplified and models can be made to describe experimental data. Parallel or consecutive parallel models are the two types of lumped models that are commonly used. In parallel models, reacted products do not undergo further reaction, making these models the simpler and easy to compute. In contrast, consecutive parallel models do allow distillates to undergo further reaction resulting in a more complex model with better flexibility. Some recent work has been completed on producing a model that employs probability distributions with success.

From the works presented above several important conclusions were made. Firstly, paraffins are mainly subjected to carbon-carbon scission reactions. This can be contrasted against asphaltenes which have a preponderance of alkylaromatic functionality that generally undergoes dealkylation reactions. Gas composition from thermal cracking is usually independent of severity and reactivity of a feed and was found to be highly dependent on its asphaltene content at low conversion. In addition, studies show that the formations of distillate products exhibit apparent first order kinetics [50]. There is a significant deviation, however, from this trend at higher severity. Finally, although there is a broad range of activation energies reported for both cracking and condensation reactions, this variation is likely due to the degree of lumping as well as the compositional differences within the considered lump.

SECTION 2.3 AQUATHERMAL CRACKING REVIEW

Due to the large variety of terminology used to describe heavy oil upgrading processes, especially those involving water or hydrogen, it is important to clearly define the terminology to avoid confusion. In this thesis, the use of water added to heavy oil during strictly thermal conversion is referred to as aquathermal treatment. A literature review has shown that aquathermal treatment may also be referred to as hydrous pyrolysis or hydrothermal treatment. This thesis avoids the use of hydrothermal, because the term is most often used to describe processes that involve molecular hydrogen. Although there is debate whether water plays a physical, chemical or catalytic role, aquathermal treatment is distinguished from those systems that use both water and catalyst in a process sometimes referred to as aquaconversion.

Conventionally, water is a poor solvent for oils due to their polarity differences. However, the polarizability of water is greatly dependent on temperature and pressure as reflected in its dielectic constant. Keger *et al*. [56] found that water`s dielectic constant greatly decreased with increasing temperature implying that water becomes more miscible with oil systems at elevated temperatures, particularly as the critical temperature is approached. Work by Griswold and Kasch [57] confirmed this observation, as the authors found that water solubility in petroleum residue is independent of the molecular weight of the oil. It was also determined that water in oil solubility is greater than that of oil in water. This result was also shown in Amani *et al*. [58] where it was seen that the solubility of water in Athabasca bitumen was greatly enhanced with increasing temperatures.

Since water at high temperatures and pressures is conducive to its miscibility with oil it is implied that for water to be effective, reacting conditions should be at supercritical or near critical conditions. Kruse and Dinjus [59] examined water at both near and supercritical conditions as a reaction medium. They found that super critical water (SCW) makes a good reaction medium as it reduces coke formation on heterogeneous catalyst while maintaining good mass transfer rates. Water tends to

form cages when used in excess. As such, it was found that cracking reactions were slowed due to the decreased collision frequency between reactants.

Relative to a nitrogen atmosphere, Cheng *et al*. [7] observed a significant reduction of coke formation when vacuum residue was pyrolyzed in SCW. Using high water to oil ratios from 2:1 to 4:1, temperatures of 380 to 420 °C and reaction times from 25 to 60 minutes, they discovered that the product had higher conversion and lower viscosities. The increased conversion was attributed to the solvent effect, as low density of SCW not only has good solubilities for light oil components but also low mass transfer resistances. While reduced coke formation was attributed to dispersed micro-emulsions which can hinder condensation reactions. Observed increased conversion due high water concentrations reported by Cheng *et al.,* however, is a result that contradicts the Kruse and Dinjus' suggestion that higher water conversion may slow cracking reaction.

Comparable results were found by Han *et al*. [60] when conversion of coal tar pitch was subjected to reacting conditions of 400 to 480 °C, pressures at 22 to 40 MPa and residence times of 1 to 80 minutes. SCW was found to heighten maltenes yield while diminishing coke formation. It was determined that pressure had only a minimal effect on maltene yield and asphaltene conversion, but high pressures reduced formation of gaseous product. In contrast, temperature had a more significant effect on final product composition. Zhao *et al*. [61] also found that higher temperatures and residence times resulted in large yields of saturates when cracking with SCW at a water concentration of approximately 43 wt.%.

Aquathermal treatment of asphalt carried out in an autoclave at temperatures of 200 to 350°C, 50 MPa over a 72 hour period was conducted by Schlepp *et al*. [62]. Water was added gradually to ensure there was a liquid phase at reaction setpoint. Significant conversion was only observed at temperatures of 330 °C or higher with a marked increase in aliphatics at 350 °C. Authors contend that water plays a physicochemical role in reactions, where it acts as a hydrogen source during radical chain reactions aiding in the maturation of the oil. Thus, slightly increasing

conversion as reflected in their results. It was also suggested delayed coke formation was a result of the hydrogen donation which can stabilize free radicals to reduce condensation reactions.

In order to determine if water had a chemical role in cracking reactions, Morimoto *et al*. [63] conducted a series of experiments using SCW, supercritical toluene and nitrogen atmospheres. Products composition from the SCW and nitrogen tests were very similar relative toluene tests leading to the conclusion that water does not participate in chemical reactions. Enhanced conversion in SCW relative to the nitrogen run was attributed to the solvent effect. Morimoto continued to work with SCW [64] and also found that less toluene insolubles were produced and, similarly to Cheng *et al*. [43], rationalized that this was due to the dispersion effect.

Conflicting results presented by Sato *et al*. [65] claim that water does participate during the thermal cracking of asphalt by providing hydrogen used for capping of free radicals. As such it is claimed that SCW can be used for partial oxidation of organic complexes. Experiments were conducted 340 to 400 °C with water under an argon or air atmosphere. Higher maltene yields were formed under an argon atmosphere and were attributed to water being an additional hydrogen source that cap radicals. Using air, it was determined the oxygen increased the desulfurization of asphalt by enhancing sulfur mass transfer to the toluene insolubles. Sato *et al*. completed addition work dealing with SCW with hydrogen and carbon dioxide atmospheres [66]. It was proposed that coke formation was suppressed though was reverse water gas shift reaction when the presence of hydrogen and carbon dioxide was added to SCW.

Studies containing salt additives were also conducted. Clark and Kirk [15] used iron or ruthenium chlorides on Peace River and Cold Lake bitumen. Water alone was found to reduce insolubles formation in Cold Lake but not in Peace River sample. The addition of ruthenium additives enhanced the amount of desulfurization that took place at the cost of increased coke formation, the authors hypothesize that ruthenium promotes carbon-sulfur bond cleavage. This cleavage, however, leaves

many reactive fragments that can polymerize into coke. In contrast, iron was found to reduce coke products by inhibiting coupling reactions. Similar work by Gregoli *et al*. [67] found that the use of brine solutions at supercritical conditions for thermal treatment resulted in higher yields of lighter product at lower viscosities. However, caution should be exercised when using chlorides as it may promote corrosion.

A recent study by Nhieu [68] investigated the effect of water on Athabasca tower bottoms cracking at aquathermal conditions. Reacting at a temperature of 420 °C and water concentrations varying from 17 to 33 wt.% the operating pressure was dependent on the amount of water added to the system. Results show that onset time of coke formation was only slightly increased or decreased based on the added water content. In addition, coke yield did not appreciably change with varying water content. It seems then that the solvent effect observed by many of the previous papers is only effective at high water content systems. In addition, Nhieu`s results indicate that water does not change final product composition once again suggesting that water does not play a chemical role in thermal cracking.

In conclusion, there is general agreement that water does have an effect on heavy oil cracking at higher water to oil ratios. There are conflicting results however, that report whether water participates as a chemical reactant. It seems that most studies do concur that water does play a physical role when the thermal treatment was carried out for oil in water systems. At these concentrations, water can either provide a solvent or dispersion effect, both of which can result in benefits of increase conversion and reduced coke formation.

Chapter 3 : Experimental Methodology and Apparatus

Chapter three presents the equipment and the experimental procedure used. Section 3.1 presents the various heavy oils that underwent cracking reactions along with chemical reagents that were used. Descriptions of the microreactor and Parr reactor design along with supporting equipment are given in Section 3.2. A report of both the hot stage microscopy and laser backlight scattering equipment used as techniques for the *in situ* observation of cracking reactions is covered in Section 3.3. Also provided in this section are techniques used for feed characterization. The chapter concludes with the experimental procedure and the operating conditions tested during this thesis.

Section 3.1 Heavy Oil Feeds and Chemicals

Section 3.1.1 Heavy Oil Feed

This study uses a variety of heavy oil feed stocks, a summary of which are listed in Table 3.1. Athabasca vacuum residue was the most extensively studied as it will be used for both the kinetic and aquathermal investigations. The other five feed stocks were exclusively used for the kinetic studies with the polarized microscopy setup.

Table 3.1: Heavy oil feeds

Heavy Oil	Location
Athabasca Vacuum Residue	Athabasca Basin, Canada
Cold Lake Bitumen	Cold Lake Basin, Canada
Safaniya Vacuum Residue	Safaniya Oil Field, Saudi Arabia
Cerro Negro Crude Oil	Venezuela
Guado Vacuum Residue	China
Columbian Vacuum Residue	Columbia

Section 3.1.2 Chemical Reagents

In addition to the heavy oil feeds, other chemicals were used as reagents to clean the reactor or add to the reactor. Table 3.2 is a summary of the compounds used, their purity and where they were obtained. Nitrogen, for example, was used to purge the reactor of oxygen and to provide a pressurized inert atmosphere. Water was added

to specific experiments for the aquathermal investigation. Toluene and methylene chloride were used as washing solvents, with ethanol and acetone used specifically to clean the sapphire windows or any optical devices such as probe tips and objective lens. Carbon disulfide was only used to flush the reactor when the sample collection was required for simulated distillation.

Table 3.2 Chemical reagents used in this investigation

Chemical Compound	Manufacture	Grade or Purity	Intended Use
Water	In House from Milli-Q	Deionized	Reactor Feed
Nitrogen	PRAXAIR Canada Inc.	High Purity 4.8 99.998%	Reactor Feed
Helium	PRAXAIR Canada Inc.	Ultrahigh Purity 5.0	Simulated Distillation
Toluene	Fisher Scientific	ACS Certified 99.9>	Cleaning
Methylene Chloride	Fisher Scientific	ACS Certified 99.9%>	Cleaning
Carbon Disulfide	Sigma-Aldrich Co.	99.9% >	Cleaning
Acetone	Fisher Scientific	99.7%	Cleaning
Ethanol	Bio Basic Inc.	Denature, Anhydrous 85% >	Cleaning

Section 3.2 Reactors Setups

Descriptions below are provided for two different reactors designs that were used to conduct experiments. Microreactors were used for experiments involving the *in-situ* observation of heavy oil cracking monitored using backscattering phenomenon. The Parr reactor was used to experimentally validate simulated pressures for aquathermal trials calculated using process simulation software.

Section 3.2.1 Microreactor Design and Supporting Equipment

Microreactors used in experiments are composed, in part, of stainless steel parts from Swagelock®. Reactors are the vessels where samples are heated up and pressurized under a nitrogen atmosphere. A listing of individual components of the

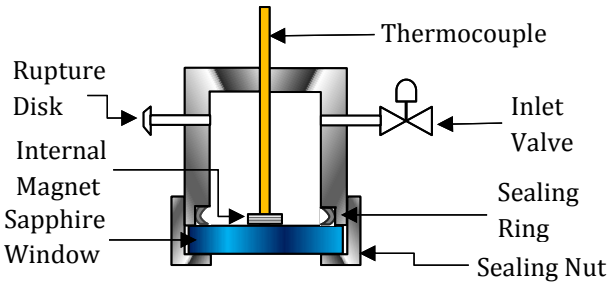

Figure 3.1: Sideview schematic of reactor

reactors can be found in Appendix B. All reactors have a thermocouple threaded down the center. The thermocouple serves the dual purposes of measuring the temperature while also acting as a shaft for the magnet stirrer. Mixing inside the reactor is achieved by the rotation of the internal magnet. The mixing speed is controlled by a larger external magnet attached to the end of a shaft of a speed adjustable motor. Total volume of the reactor cavity and rupture disk assembly was measured to be 6.4 mL. At the bottom of each reactor is a small groove where a metal sealing ring sits. Upon placement of the sapphire window and sealing nut, the sealing ring will deform as the sealing nut is tightened. This will produce a seal that can withstand reaction pressures and prevent sample leakage during experiments. Metal sealing rings are single use only, as their permanent deformation prevents them being used again. Users have a choice of the type of window, sealing ring and sealing nut, as the types used will be determined by pressures expected during experiments and polarizations state of the illuminating light. The table below summarizes the two options available:

Table 3.3 Reactor sealing options

Component	High Pressures (P>5MPa)	Low Pressure (P<5 MPa)
Sealing Ring	C-Ring	O-Ring
Sapphire Window Thickness [mm]	8	5
Sealing Nut	Parker Ultraseal Reducer	Swagelok® VCO Nut

Sapphire windows manufactured by Meller Optics are selected based on thickness and crystal axis orientation. The crystal axis is orientated in a manner that is parallel with the incoming light in order to minimize sapphire crystal birefringence. Another important factor is window thickness, which must be designed to be able to withstand experimental pressures at elevated temperatures. A study by Wachtman and Maxwell, measured the modulus of rupture for sapphire crystal of different crystal orientations [69]. Calculations using these results determined that a window thickness of 5 mm is adequate for pressures up to 6 MPa and 8 mm is sufficient for pressures up to 16 MPa. It is important to use the correct sealing ring with the proper window thickness as incorrect use will lead to leakage or window failure.

There are several pieces of supporting equipment for the use of microreactors, these include reactor casings, temperature controllers and rupture disk assemblies. Documentation is provided regarding each piece of supporting equipment.

Section 3.2.1.1 Reactor Casing

Two different experimental apparatuses were used to characterize the backscattered light: polarized hot stage microscopy and laser dynamic light backscattering. The reactor described in Section 3.1.2 was used in both setups. Reactors are positioned vertically (as shown in Figure 3.2) on a platform. The platforms are made in an inverted configuration with a hole where the window is situated above, as the observation of the liquid phase phenomena is made from below the reactor. It is important to note that observations are not made from above of the reactor. If this were the case observations would be influence by both the vapour and liquid phases. Also, reactors are placed within a band heater connected to a temperature regulator. All heaters are encased with a layer of glass wool insulation and are held in place by a metal case as shown in Figure 3.2.

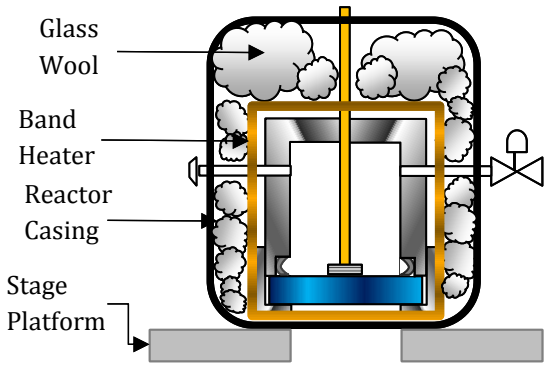

Figure 3.2: Sideview schematic of reactor with casing

Section 3.2.1.2 Section 3.2.1.4 Temperature Controllers

Both reactor setups used a two mode, OMRON E5CK temperature regulator. The regulator uses a K-type thermocouple that reports temperatures with a precision to the tenth decimal place. The first mode is manual where the user is able to set the output of the controller to an exact value. The second mode of operation is the automatic setting where the controller will regulate and achieve the desired setpoint on its own. The automatic mode may be operated at a constant temperature ramp rate, or may also be set to reach a setpoint as quickly as possible based on the PID parameters. On average heating ramps took approximately 10 to 15 minutes from 350 °C to the desired setpoint.

Section 3.2.1.3 Rupture Disk Assembly

Experiments that operated at aquathermal conditions required a rupture disk assembly to prevent over pressurization. Inconel rupture disks procured from Zook® were nominally rated for 22 MPa at 22.2 °C. Based on calculations, the disk was estimated to be able to withstand 16 MPa of pressure at the reaction temperatures used in this study. To prevent condensation of water during experiments, the rupture disk assembly required additional heating as the assembly adds a significant amount of volume to the setup. As such the rupture disk assembly is heated by a second band heater connected to its own temperature controller. COMSOL simulations were carried out to show that temperatures in all sections of the reactor remained above the water dew temperature. Additional simulation information is provided in Section 4.4.1.

Section 3.2.2 Parr Reactor

One important parameter of the aquathermal investigation is the operating pressure which is highly dependent on the amount of water loaded. Although Bordon pressure gauges are equipped to both setups, these devices are not appropriate for the aquathermal study. Since pressure gauges and transducers are not designed to be heated, the usage of such devices introduces a cold sink in the system, allowing for considerable water condensation. Due to the small amount of water loaded in the microreactors, even the slightest amount of condensation can greatly lower

pressures, skewing results. Since pressure was not directly measureable without the introduction a cold sink, final operating pressures were predicted using process modeling software (VMGSim). In order to validate simulated results, aquathermal tests at similar operating conditions, were conducted using a Parr reactor. Unfortunately, there are still cold surfaces on the head of the Parr reactor, but since the Parr reactor has a considerably larger working volume than the microreactor setup, the final pressure is not as sensitive to small amounts of water condensation.

The Parr reactor used in this study was 500 mL in volume with a head cover that closes on top of the cylinder. This particular reactor was designed to withstand pressures and temperatures of up to 30 MPa and 500 °C respectively. It is sealed with a graphite gasket that is compressed in between the cylindrical body and the head. There are two semicircular clamps that lock the cover to the body, which results in the deformation of the gasket in order to form the seal. The body of the reactor is inserted into a heater, while the reactor cover and extremities are kept above and outside heater. The Parr reactor head has several openings, which allow for various functions as shown in the side view profile in Figure 3.3. In the center of the reactor is a thermowell for the insertion of a thermocouple that measures the internal temperature. The thermocouple in the thermowell is never in direct contact with the sample and is used for monitoring purposes only. A second thermocouple inserted near the pressure gauge, was positioned to report wall temperatures to a temperature regulator for control purposes. There is also a u-tube inside the reactor for cooling water in the event that immediate cooling is required. Finally the reactor head also contains a stirring shaft with an impeller located at the bottom of shaft. The stirring speed was controlled by an external controller attached to the temperature controller.

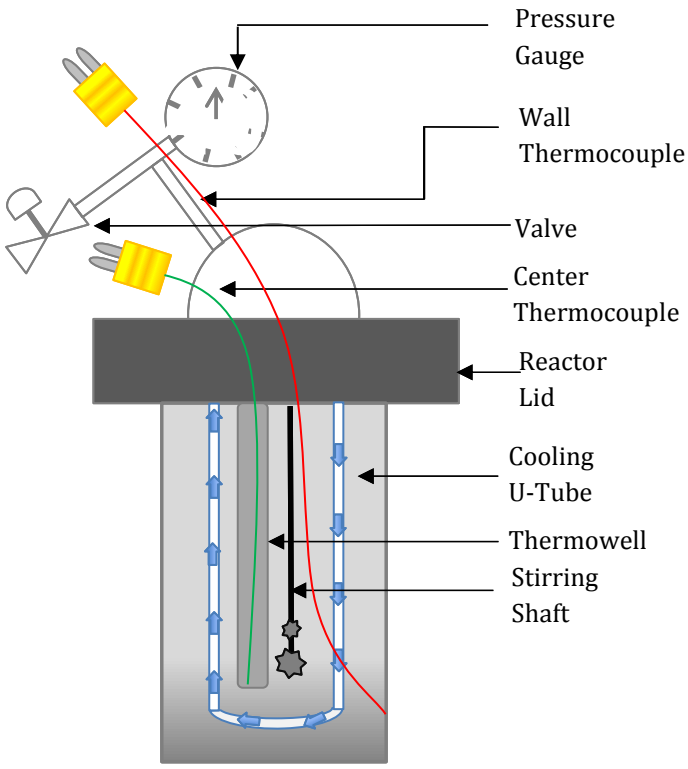

Figure 3.3 Crosssection of the Parr reactor

SECTION 3.3 EXPERIMENTAL APPARATUS

SECTION 3.3.1 POLARIZED HOT STAGE MICROSCOPY

Polarized hot stage microscopy is a powerful detection technique for mesophase, as the anisotropic nature of the substance appears as bright domains in the micrographs. This experimental setup consists of an Axio Observer.D1m inverted microscope equipped with a Zeiss AxioCam lcc3. Situated above the microscope is a soundproof enclosure in which the reactor is located. There are four different objective lens attached to the microscope with different magnifications including: 50x, 100x, 150x and 200x. Higher magnification allows for increased optical resolution and earlier detection of mesophase. Increased magnification however, also resulted in decreased viewing coverage. It was decided that only the 50x and 100x magnifications would be used so that observation of the bulk oil phase can be

monitored. In addition, the microscope has the option of viewing the sample through the objective or passing the image through the Zeiss AxioCam lcc3 to a computer where micrographs can be recorded. The light used to illuminate the sample is passed through a series of filters which can alter the polarization of the light before arriving at the objectives. One set of filters which are used for bright field observation do not change the polarization of the light. The other filters linearly polarize the passing light and were used for all of the experiments in this work. Light brightness was controlled by a dial which determines the amount of voltage supplied to the bulb. Figure 3.4 is a side view of and a schematic of the microscopy setup.

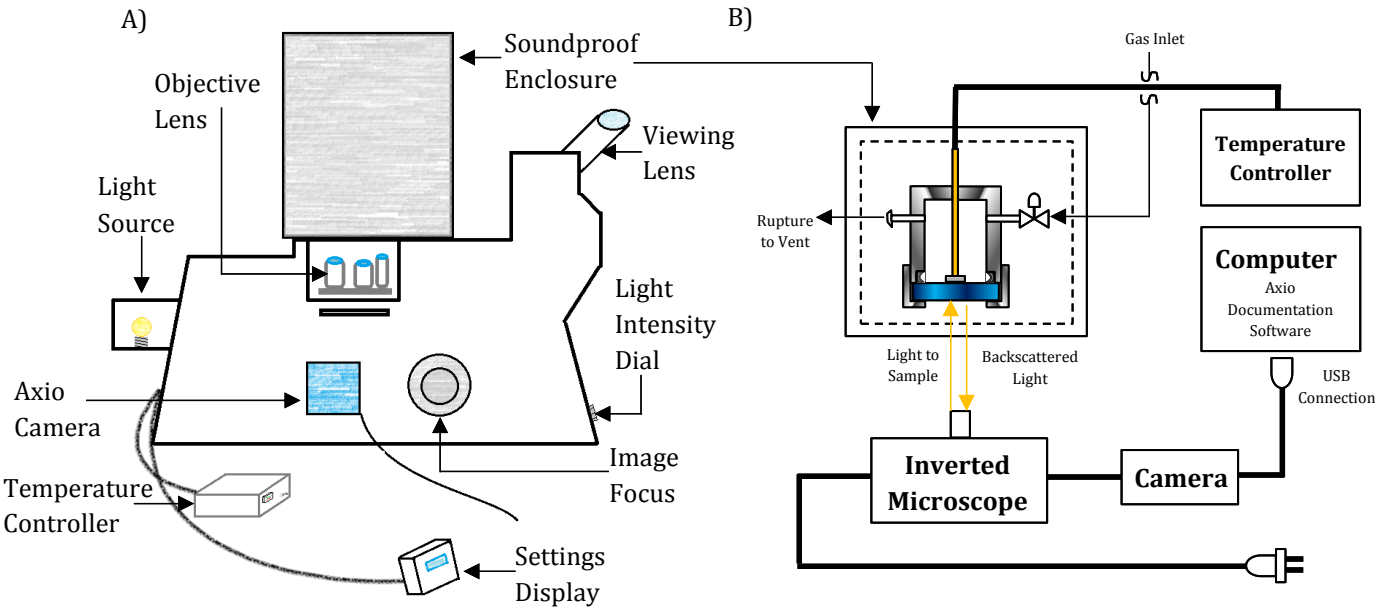

Figure 3.4: A) Sideview of microscopy setup B) schematic of microscopy setup

Micrographs taken at one minute stages were analyzed using a photo editing software named Gimp Version 2.1. The image processing software determined a value in a range of 0 to 255. Higher values indicate greater intensity of the color in question. The average of the RGB values is defined as the mean grey value (MGV). This parameter describes the average brightness of the picture and evolves during the reaction.

SECTION 3.3.2 LASER DYNAMIC BACKSCATTERING

The laser dynamic backscattering apparatus monitors also monitor the intensity of backscattered light. Since mesophase formation is strongly correlated with backscattering intensities, this method is an alternative technique that can characterize mesophase formation. An MGL III 532 100 mW DPSSL driver provided the power needed to a diode-pumped solid-state (DPSS) MGL III 532 laser that produced a green light at a wavelength of 523 nm. The intensity of the laser can be adjusted using the driver. The monochromatic light from the laser is transferred to a probe by a 100 μm SMA to FC-PC fiber optic cable. The probe is a device used to polarize the incoming green light as it enters the EX input port. As this point the light is sent to a stainless steel probe tip that has a focal point of 20 mm and a spot diameter of the point of 0.3 mm. The focal point of the probe tip is positioned at the sapphire-oil interface where the green light is scattered by the chemical moieties in the residue. Additional information on the laser focal point positioning is provided in the Appendix.

Once the light is backscattered it is collected at the probe tip, and is separated into its perpendicular and parallel components. At this point the separated light exits the probe at two different ports and is sent to the detector by a 500 μm multimode FC-PC fiber optic cable. The detector converts the light into a signal which can be processed by the dual channel Newport Powermeter 290-36R. The powermeter is able to send the measurements to a computer for further processing. A schematic of the laser setup is provided in Figure 3.5.

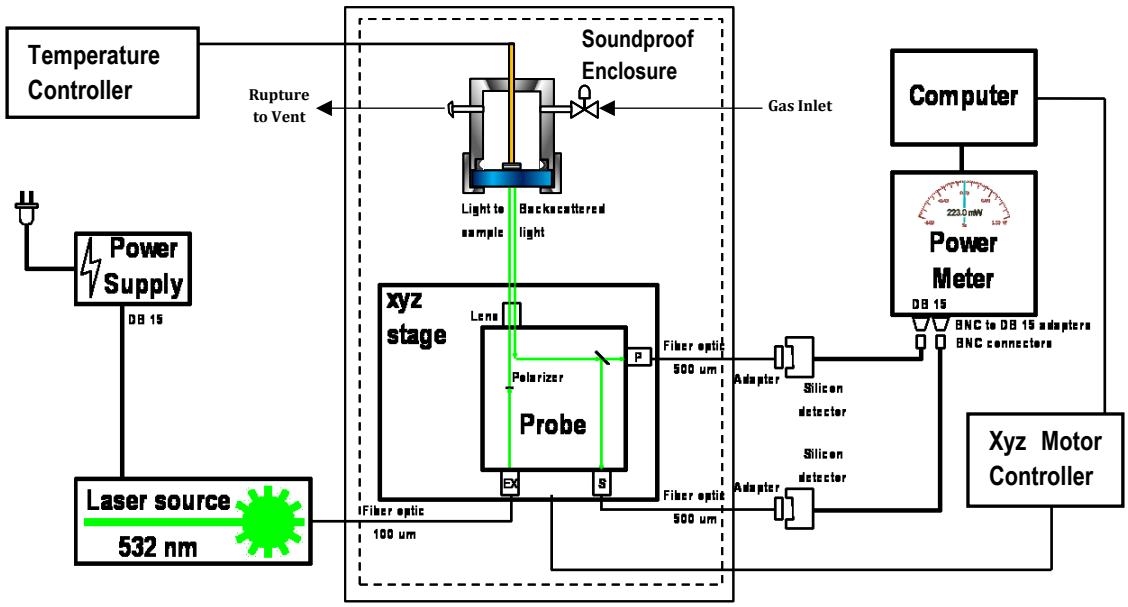

Figure 3.5: Schematic of laser backscattering system [6]

In order to obtain proper probe positioning, this setup also features a motorized xyz stage. Each axis is composed of a Thorlab MTS50-Z8 motorized stage that is able to move 50 mm through both software and mechanical control. The motorized stage was used in conjunction with a LabVIEW program that recorded the temperature and depolarization ratio. This program reports data approximately every 15 seconds, by averaging four sample points taken during the 15 seconds. Data in a text file for further analysis.

Section 3.3.3 Simulated Distillation

Simulated distillation was carried out using a Varian 450-gas chromatograph which used an Agilent capillary column with the dimensions of 5 m x 0.53 µm x 0.09 µm for the length, inner diameter and film thickness respectively. Using CampassCD, Version 4.0.0 from Burker, several sequences were created to determine the boiling point curve for various feeds. The GC uses helium as a carrier gas at a flow rate of 20 mL/min and is referenced against a standard reference sample ASTM D6325/D7169 reference material. Samples are diluted in carbon disulfide at low concentrations of 0.8 to 1 wt. %, and are prepared immediately before analysis as to minimize any losses of the carbon disulfide solvent. Then samples was subjected to a temperature program that heated the feed from -20°C to 430°C at a rate of

15 °C/min for 15 minutes. At this point the sample is held at 430°C for 30 minutes for a total time of 45 minutes. This methodology follows the procedure recommended by the ASTM 7169.

Section 3.3.4 Elemental Analysis

Carbon, hydrogen, nitrogen and sulfur (CHNS) elemental analysis on feeds was conducted using a FLASH 2000 compact elemental analyzer. The analyzer uses a Thermo-Scientific MAS 200R autosampler that injects the desired amount of sample from tin containers into a combustion chamber where a 250 mL/min of oxygen is injected for 5 seconds. The sample is left to combust and resulting gases are carried by a helium flowrate of 140 mL/min into a column filled with copper for further reduction before gases elute at various rates in the GC column. Gaseous products eventually reach a thermal conductivity detector that sends data to the computer that uses Eager Xperience to analyze the results. Elemental analysis were conducted by members in the IOSI laboratory.

Section 3.4 Experimental Procedure and Methods

Section 3.4.1 Loading and Cleaning Procedures

The loading and cleaning procedure for the reactor setup is similar for all types of experiments. A clean reactor, with the appropriate window thickness and sealing ring designed for the expected pressure, is loaded with sample. Once loaded the reactor is sealed and then leak tested with nitrogen pressure up to 5 MPa or 15 MPa dependent on sealing ring used. Contingent on a successful leak test, the experiment is carried out. Specifics of each reaction are described in subsequent sections.

Once the experiment is completed, the reactor is cooled, opened and cleaned. Thorough cleaning was achieved both by physical and chemical means. The reactor was subjected to polishing using sandpaper and cotton swabs and rinsing with chemicals such as toluene and methylene chloride. Since the reactors are reused, proper cleaning is important to prevent cross contamination between experiments.

SECTION 3.4.2 KINETIC EXPERIMENTS

The objective behind these experiments is to determine the activation energy of visbreaking reactions for various crude oils. In total, six oils were tested as shown in Table 3.1. To gain a better understanding a variety of trials were conducted on both setups.

Thermal cracking of Athabasca vacuum residue was studied by loading low pressure reactors with approximately 0.7 g of sample. Reactions were conducted under nitrogen at atmospheric pressure. The reactor was operated in semi-batch mode venting any gaseous products formed during the reaction to maintain atmospheric pressure. Once reactors were loaded, thermal cracking was carried out at 410 °C, 420 °C, 435 °C and 450 °C until mesophase was observed. The temperature ramp from 350 °C to the reaction setpoint takes approximately 10 to 20 minutes depending on the desired temperature. Starting at 350 °C, micrographs were recorded every minute until the completion of the experiment. Similar trials were also completed with the laser setup. For experiments carried out using the laser, the depolarization ratio and temperature was recorded using the LabVIEW program described above.

Experiments using the other feeds were conducted only on the microscopy setup. Again, the reactor was operated in semi-batch mode and was loaded with approximately 0.7 g of sample and left to react under nitrogen at atmospheric pressure. Trials for each feed was operated at 410 °C, 420 °C, 435 °C and 450 °C with no replicates due to time constrains. Micrographs were taken at one minute stages starting at 350 °C until the end of the experiment.

SECTION 3.4.2 AQUATHERMAL EXPERIMENTS

Aquathermal experiments are focused on examining the effect of water on mesophase formation during cracking reactions. Athabasca vacuum residue was studied in a batch mode operation as the current system is not designed for continuous addition of water. A Consequence of a batch operation is that, the loaded water had a large impact on the reaction pressure. To maintain subcritical conditions enough water is added to the reactor to obtain pressures up to 16 MPa.

SECTION 3.4.2.1 AQUATHERMAL PRESSURE TESTING

Several different reacting conditions were tested in the 500 mL Parr reactor. One trial operated with 40 mL of water and heated the system to 435 °C. Another trial used 170 g of Athabasca residue with 1.3 MPa of nitrogen examined the vapour pressure of the residue as it was heated to 420°C where it was left to reactor for 60 minutes. Aquathermal trials were also completed by loading the Parr reactor with 170 g of Athabasca residue with varying water concentrations of 8.1 mL, 14 mL and 17 mL. The system was then heated up a setpoint of 435 °C and left to react for 60 to 90 minutes. All experiments conducted with the Parr reactor pressurized the with 1.3 MPa of nitrogen before any heating.

SECTION 3.4.2.1 AQUATHERMAL EXPERIMENTS WITH MICROREACTOR

For higher pressure aquathermal experiments, the reactors described in Section 3.1 are loaded with roughly 0.6 g of sample and then subjected to a leak test using nitrogen up to 16 MPa. Contingent on a successful leak test, the Swagelock® VCR fitting was opened and the appropriate amount of water was loaded. The VCR fitting was chosen to be opened and resealed as it uses a deformable washer to form a consistent and reliable seal that does not need to be tested a second time. Water was not loaded before this step to prevent water stripping during the leak test.

The microcreactor was then pressurized at the desired initial nitrogen pressure, and the loading valve was closed. As aforementioned, due to the lack of design that allows for continuous water addition, all aquathermal experiments were operated in batch mode. Aquathermal experiments heated both the microreactor and rupture disk assembly to prevent the formation of cold sinks. Reactions are conducted on both microscopy and laser apparatus. Three sets of experimental conditions were conducted as follows:

- 14wt% water and 1.5MPa of nitrogen pressure initially
- 28wt% water and 1.5MPa of nitrogen pressure initially
- 14wt% water and 3.0 MPa of nitrogen pressure initially

Chapter 4 : Results and Discussion

This chapter reports the results of the experiments, the methodology used to analyze the data and a general discussion of the important findings. Section 4.1 presents the results of the residue feed characterization using simulated distillation and CHNS elemental analysis. The following portion of the chapter is separated into a kinetics study of low conversion thermal cracking and the effect of added water on reaction dynamics. The determination of activation energy is determined in Section 4.2 followed by a discussion of the mesophase onset period in Section 4.3. Next, simulation results that validate the aquathermal experimental condition are provided in Section 4.4 with the results and a discussion of the aquathermal experiments given in Section 4.5.

Section 4.1 Feed Characterization

The low conversion kinetics of six different feeds was examined using the microscopy setup. CHNS elemental analysis of each of the feeds is summarized below in Table 4.1. Results are reported in weight percent, with a 95% confidence stage from three samples.

Table 4.1: Elemental analysis of vacuum residue feeds with 95% confidence intervals

Feed	Carbon	Hydrogen	Sulfur	Nitrogen
	[wt. %]	[wt. %]	[wt. %]	[wt. %]
Safaniya VR	84.39 ± 0.24	10.07 ± 0.01	5.00 ± 0.24	0.53 ± 0.02
Gudao VR	85.27 ± 0.12	11.36 ± 0.08	2.46 ± 0.20	0.89 ± 0.02
Columbian VR	87.86 ± 0.91	9.74 ± 0.06	1.65 ± 0.14	0.73 ± 0.04
Athabasca VR	83.92 ± 0.28	9.93 ± 0.15	5.38 ± 0.39	0.75 ± 0.02
Cold Lake Bitumen	85.73 ± 0.50	9.11 ± 4.51	5.00 ± 0.10	0.59 ± 0.02
Cerro Negro Crude Oil	88.46 ± 0.93	9.40 ± 4.93	3.61 ± 0.36	0.73 ± 0.03

Boiling point distributions of each raw feed was characterized using simulated distillation with the results shown in Figure 4.1. Results indicate that the Cold Lake and Cerro Negro samples are composed of a wider range of boiling components relative to the other samples as their initial boiling points are lower as well as a higher volume of sample was boiled at the end point.

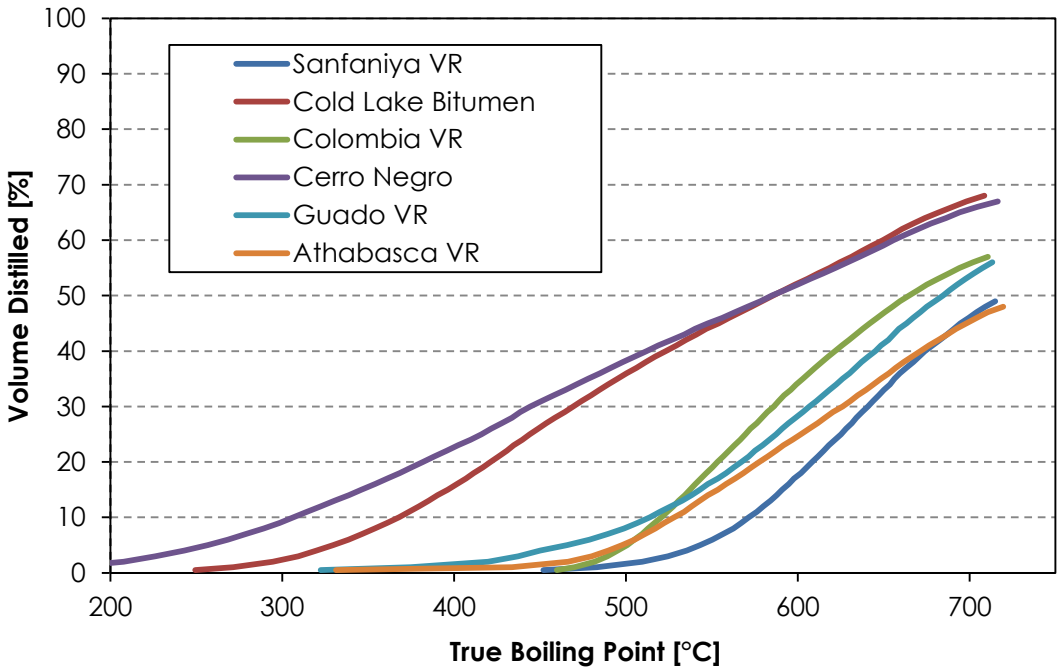

Figure 4.1: Simulated distillation results of various oil feeds

SARA analysis data was also procured from literature for the various feeds with findings summarized in Table 4.2

Table 4.2: SARA analysis data for various feeds from literature

Feed	Saturates	Aromatics	Resins	Asphaltenes
[-]	[wt. %]	[wt. %]	[wt. %]	[wt. %]
Safaniya VR [70]	10	50	26.6	13.4
Gudao VR [71]	14.5	34.8	47.2	3.5
Columbian VR				
Athabasca VR [72]	16.1	48.5	16.8	18.6
Athabasca VR [73]	17.3	39.7	25.8	17.3
Cold Lake Bitumen [73]	20.7	39.2	24.8	15.3
Cerro Negro Crude Oil [74]	15	38	35	12

In addition to the characterization presented above the Athabasca VR is also known to contain 2 wt.% fine solids [68]. The other feeds used in this study have negligible fines content.

SECTION 4.2 DETERMINATION OF ACTIVATION ENERGY OF CRACKING REACTIONS

SECTION 4.2.1 MEAN GREY VALUE AND SEVERITY FACTOR

SECTION 4.2.1.1 CONVERSION OF MICROGRAPHS INTO MEAN GREY VALUE

Sample micrographs, nominally taken at five or ten minutes stages to show the general behavior of Cerro Negro crude, Cold Lake bitumen, Safaniya and Athabasca vacuum residue are presented in Figures 4.2, 4,4 ,4.6 and 4.8 respectively. Each micrograph has a mean grey value (MGV) which reflects the average brightness of the red, green and blue components of the micrograph. The MGV is determined from image analysis as previously explained in Section 3.3.1. In this manner, MGV plots are generated to monitor the residue as it reacts. These accompanying plots are given in Figures 4.3, 4.5, 4.7 and 4.9. Time zero on the MGV graphs corresponds to the time at which the reaction medium reached 350 °C. The feeds are generally not reactive at this temperature.

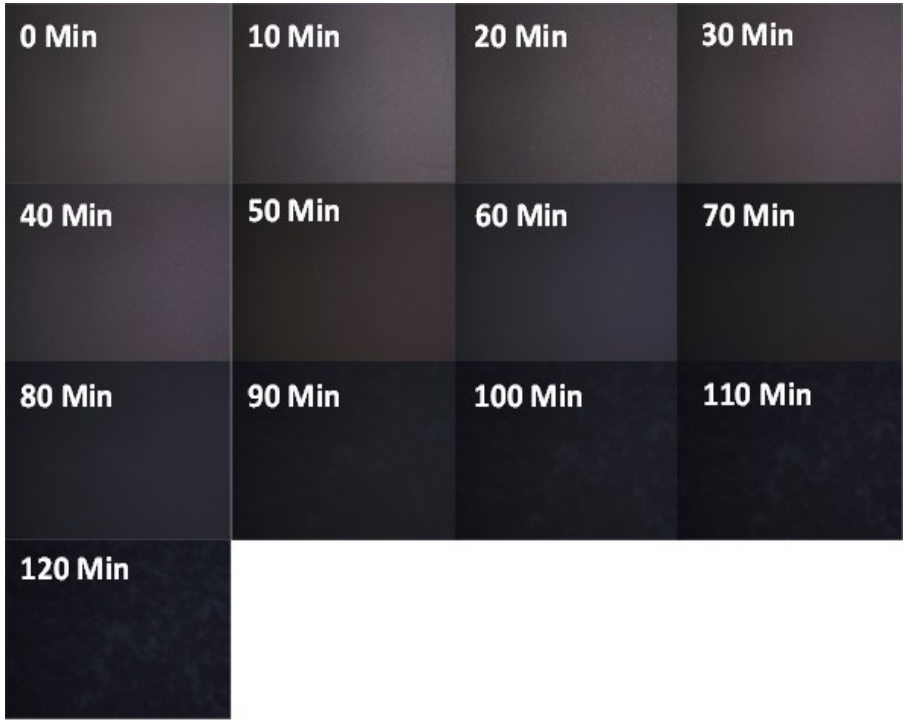

Figure 4.3: Selected micrographs for Cerro Negro crude oil at 420 °C

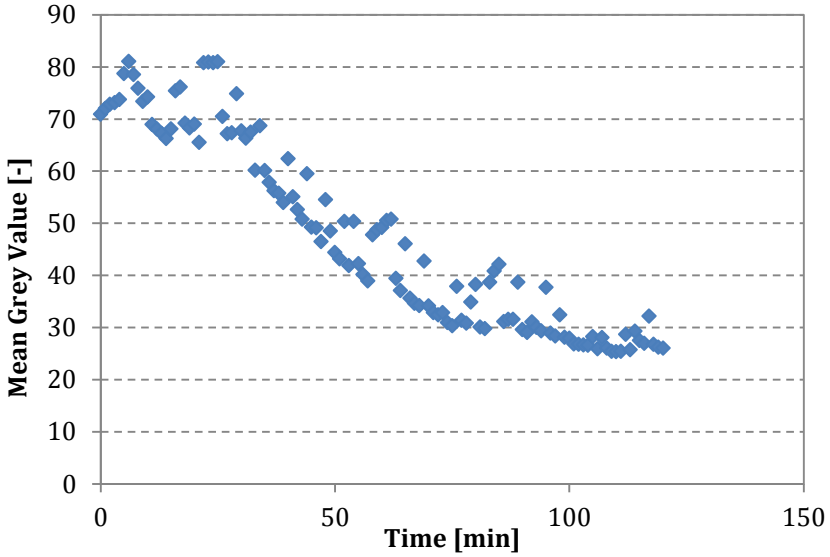

Figure 4.2: The MGV evolution for Cerro Negro crude oil at 420 °C

Figure 4.5: The MGV evolution for Cold Lake bitumen residue at 420 °C

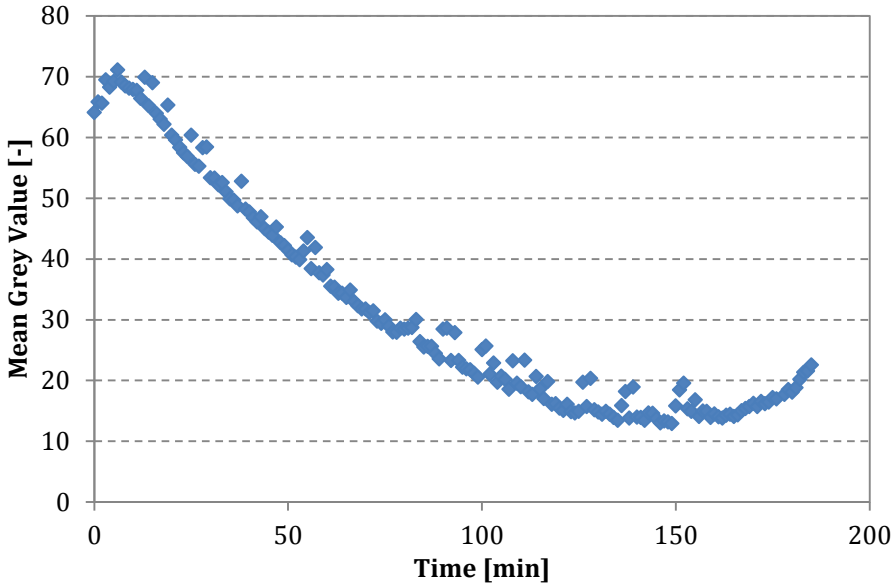

Figure 4.4: The MGV evolution for Cold Lake bitumen residue at 420 °C

Figure 4.7: Selected micrographs for Safaniya Vacuum Residue at 420 °C

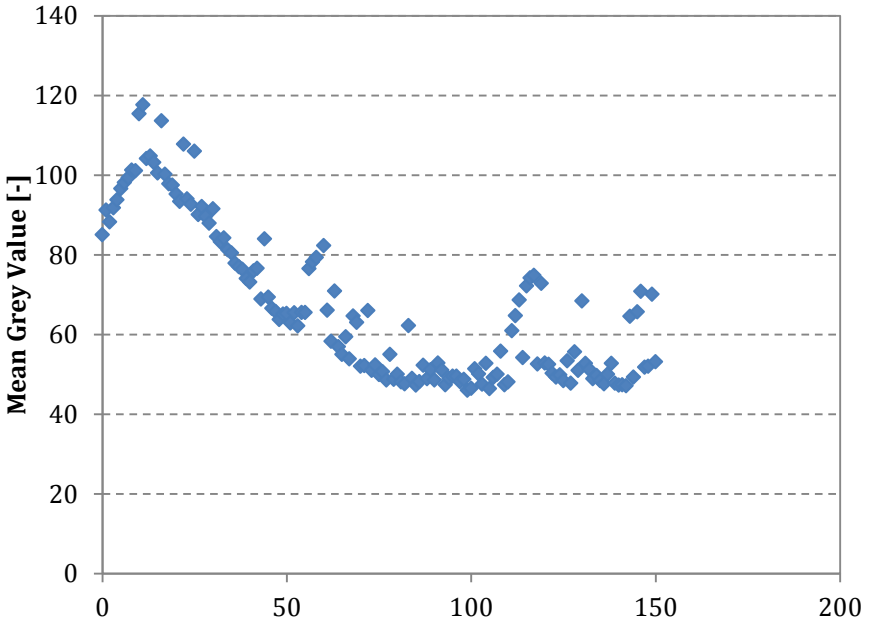

Figure 4.6: The MGV evolution for Safaniya Vacuum Residue at 420 °C

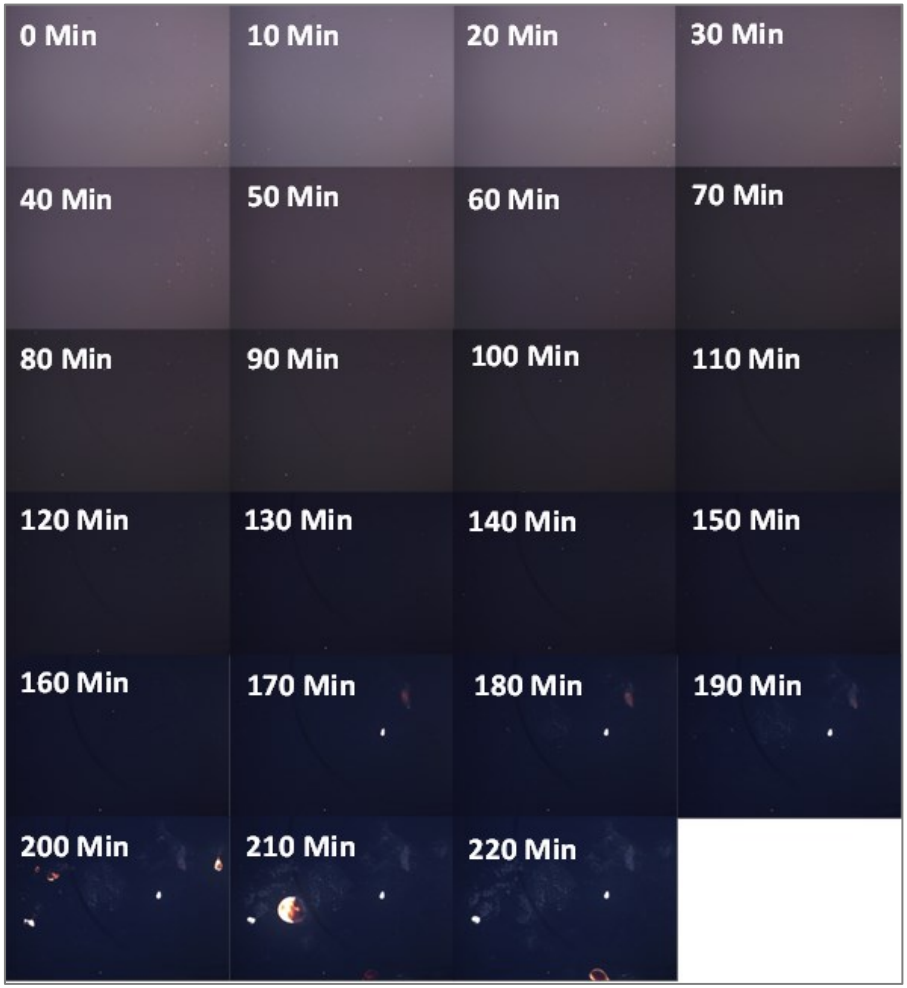

Figure 4.9: Selected micrographs for Athabasca vacuum residue at 420 °C

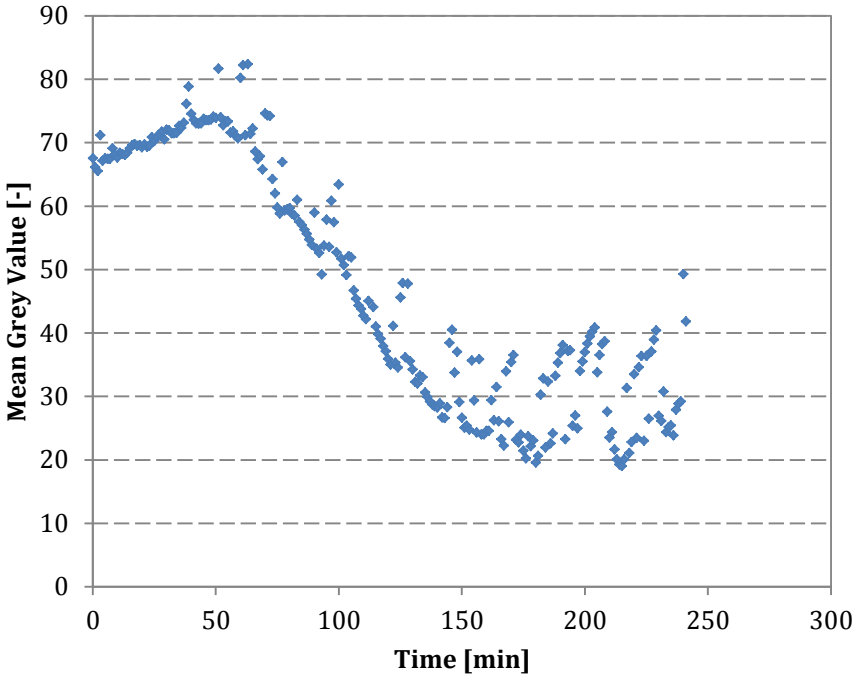

Figure 4.8: The MGV evolution for Athabasca vacuum residue at 420 °C

The MGV plots in Figures 4.3, 4.5, 4.7 and 4.9 all follow a similar trend that begins with an increase in MGV during the heating of the oil from 350 °C to the desired reaction setpoint. This initial increase in MGV is associated with the enhanced backscattering of light by the reaction medium during the heating of the system. Once the system at attained its final reaction temperature, the MGV reaches a maximum and then begins to decline for a period of time. Eventually, the rate of the decreasing MGV slows until the curve reaches a minimum. The decline in brightness is associated with reduced backscattering. During this phase of the reaction, components within the feed are reported to oligomerize, associate or coalesce into larger molecules or domains, ultimately reducing the back scattering of polarized light [37]. At extended reaction times, mesophase domains are observed, and appear as bight domains due to their optical anisotropy under polarized light. The overall brightness of the sample increases as mesophase domains grow, resulting in the leveling off of the MGV and then eventual increase. The homogeneous system becomes a heterogeneous one upon the appearance of the mesophase signifying the end of the experiment for most cases.

It is also important to note that there is noise in the MGV data. One example of this noise is shown Figure 4.8, where there seems to be two possible trendlines. While the majority of the data forms a baseline, there are artifacts that seem to form an additional trendline above the baseline. Possible artifact that result in MGV measurement error include: light bulb effects, vibration and sample movement. Light bulb artifacts, due to an overused or older bulb, can greatly introduce lighting instabilities in the system. Additionally, optical equipment is very sensitive to heating and movement during testing. Upon replacement of the bulb, and the development of a more stringent operating procedure to minimize these variables, it was found that the observed noise was greatly diminished. One example of noisy data is given in Figure 4.9 which can be contrasted against Figure 4.4 after the technique is improved.

Two general trajectories for the evolution of MGV with time were observed. Samples including, Athabasca, Cold Lake, Safaniya and Cerro Negro residue all

exhibited similar trends. There was a departure from this behavior for the residues from Gudao and Columbia, as presented in Figure 4.10 and 4.12.

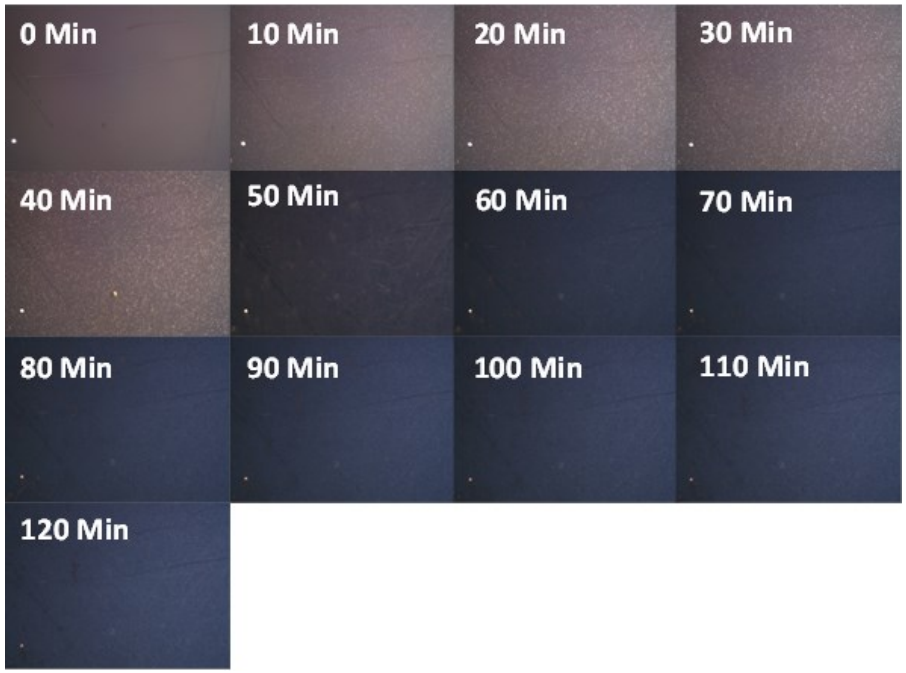

Figure 4.11: Selected micrographs for Gudao vacuum residue AT 420 °C

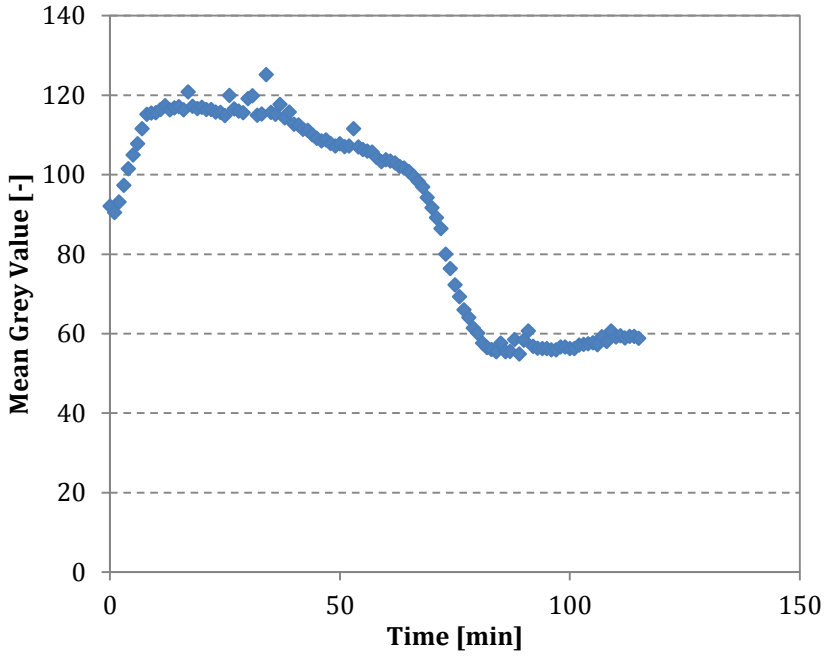

Figure 4.10: The MGV evolution for Gudao vacuum residue at 420 °C

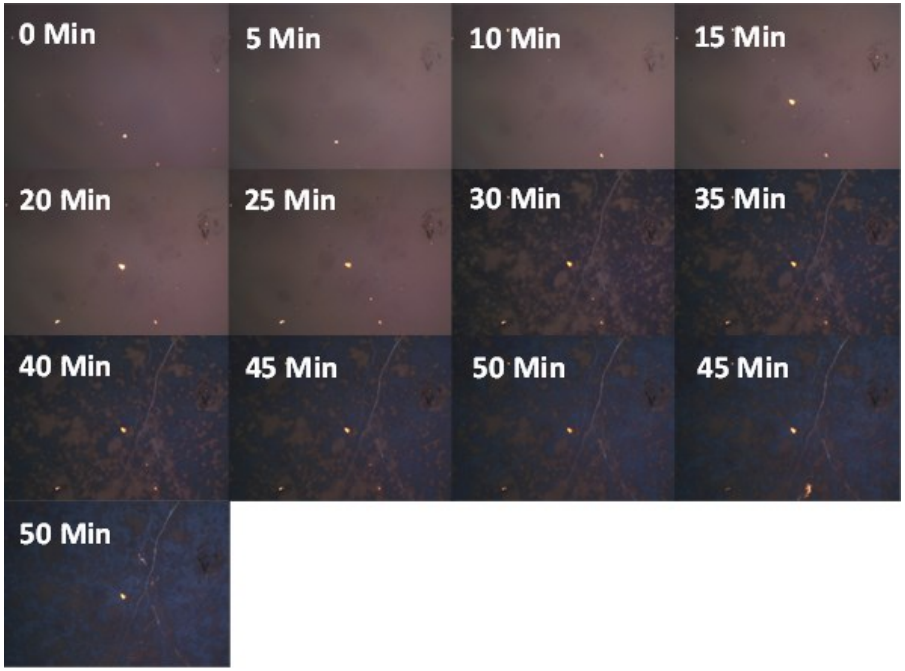

Figure 4.13: The selected micrographs for Columbian

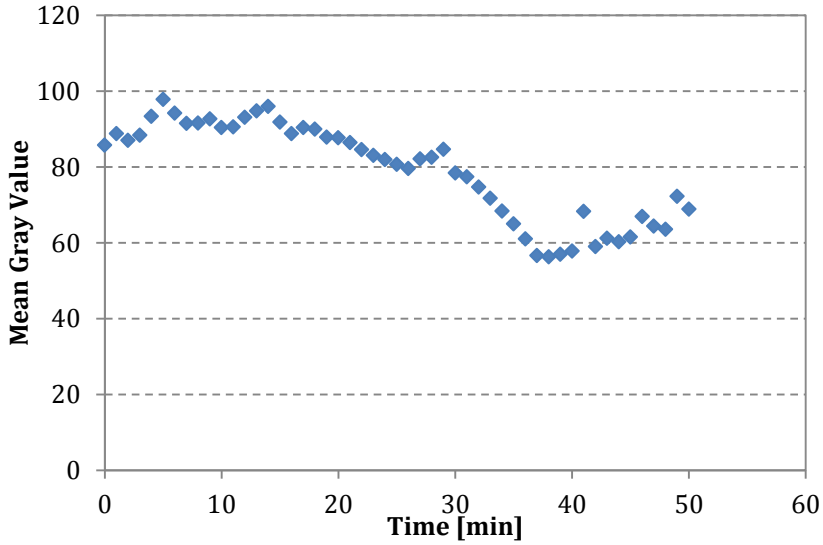

Figure 4.12: The MGV evolution for Columbian residue at 420 °C

Similarly to the feeds in Figures 4.2-4.9, both Columbian and Gudao feeds also ultimately results in mesophase formation upon extended reaction times. However, as shown at the 50 and 30 minute marks for the Gudao and Columbian feeds respectively, these feeds experience an initial phase separation before mesophase onset. The initial phase separation results in the deposition of an uneven dark patchy film on the sapphire window resulting in a different MGV trend as shown in Figures 4.11 and 4.13. The MGV graphs in these cases reveal that once the feeds have attained their maximum MGV, a much slower decline is initially observed followed by a sharp drop before the curves reach their minimum.

In summary, all feeds tested result in the formation of mesophase if given sufficient time for the residue to react. The mesophase formation turns the otherwise single homogeneous phase into heterogeneous multiphase system. There is a distinction to be made, however, when the appearance of the multiphase system occurs. In the cases of Cold Lake bitumen, Athabasca VR, Cerro Negro and Safaniya where the bulk oil phase is observed to gradually darken as a whole before the mesophase fouling. This is different in the cases of Columbian and Gudao where earlier phase separation is seen before the observation on mesophase. In this case, the early dark patchy deposits are referred to as film fouling.

Section 4.2.1.2 Mean Grey Value Normalization and Truncation

The MGV plots in Figures 4.2-4.7 show that while the trends are consistent from experiment to experiment, the absolute MGV may vary due to the experimental setup and alignment of the microscope. Additionally, the brightness of the pictures can be greatly influence by many of the settings on the microscope. Although settings were kept as consistent as possible during the runs, considerable run-to-run variability was still observed as shown in Table 4.3.

Table 4.3: MGV values at various runs and feeds at 350 °C

Run	Cold Lake	Athabasca	Cerro Negro	Safaniya	Columbian	Gudao
1	64.1	67.5	61.7	103.6	82.5	126.5
2	141.2	58.1	70.9	85.0	85.8	89.7
3	61.9	70.3	93.6	39.6	92.4	124.4
4	66.2	64.3	82.1	90.1	65.8	100.5
Average	83.4±38.6	65.0±5.2	77.1±13.8	79.6±27.8	81.6±11.3	110.3±18.1

Due to the relatively significant run-to-run variability, the MGV was normalized so that relative changes during the MGV evolution could be compared. The normalized MGV is the quotient of the raw MGV and the MVG at 370 °C as shown in Equation 4.1.

$$MGV_{Norm}(t) = \frac{MGV(t)}{MGV_{370°C}} \quad (Eq. 4.1)$$

The MGV at 370 °C was chosen to be the reference as this temperature is the approximate threshold at which cracking reactions initiate. More information on cracking temperature threshold is given in Appendix C. The result of this normalization reduces the variability due to microscopy settings or bulb performance between different experiments. An example of normalized data is presented in Figure 4.14.

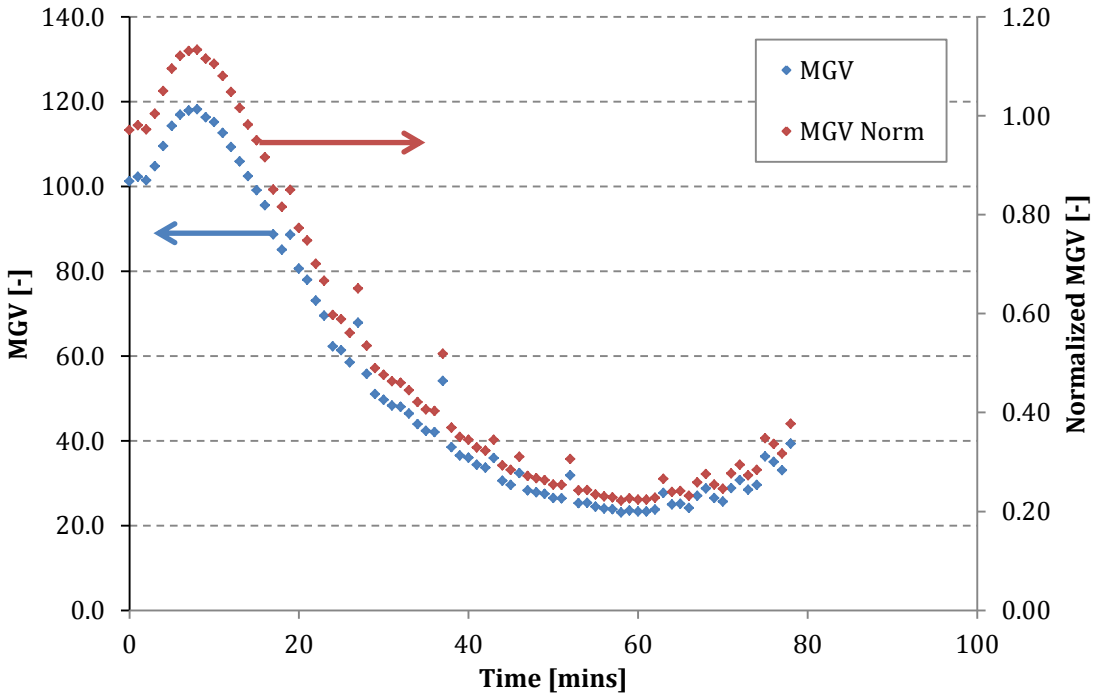

Figure 4.14: Normalization of MGV of Athabasca vacuum residue at 435°C

The initial portion of a MGV plots in Section 4.2.1.1 show the MVG increasing due to the effects of the heating ramp. For clarity, Figure 4.15 additionally plots the temperature along with MGV to demonstrate this effect.

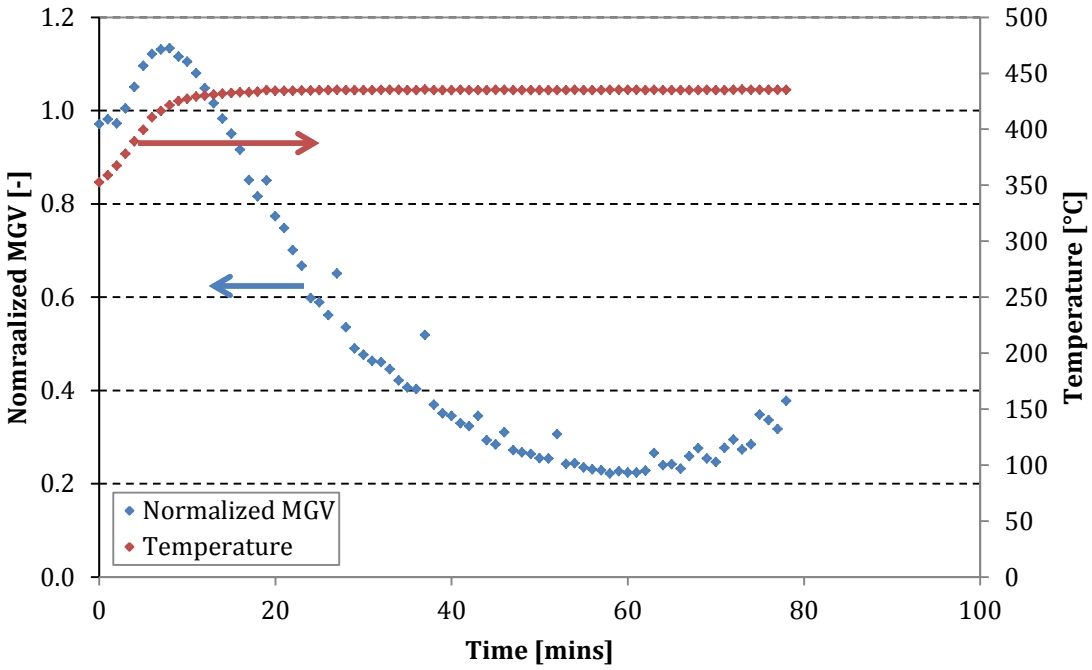

Figure 4.15: MGV temperature dependency during the heating ramp of an experiment

The MGV temperature dependence shown in Figure 4.15 raises concerns for comparisons of experiments conducted at different temperatures. In order to account for temperature effects, a trial was conducted to examine MGV as a function temperature at non-reactive conditions below 370°C. A slow heating rate of 1°C/min was used to allow for the system to thermally equilibrate. Results are presented in Figure 4.16 are normalized using the MVG at 370°C appears to follow a linear trend.

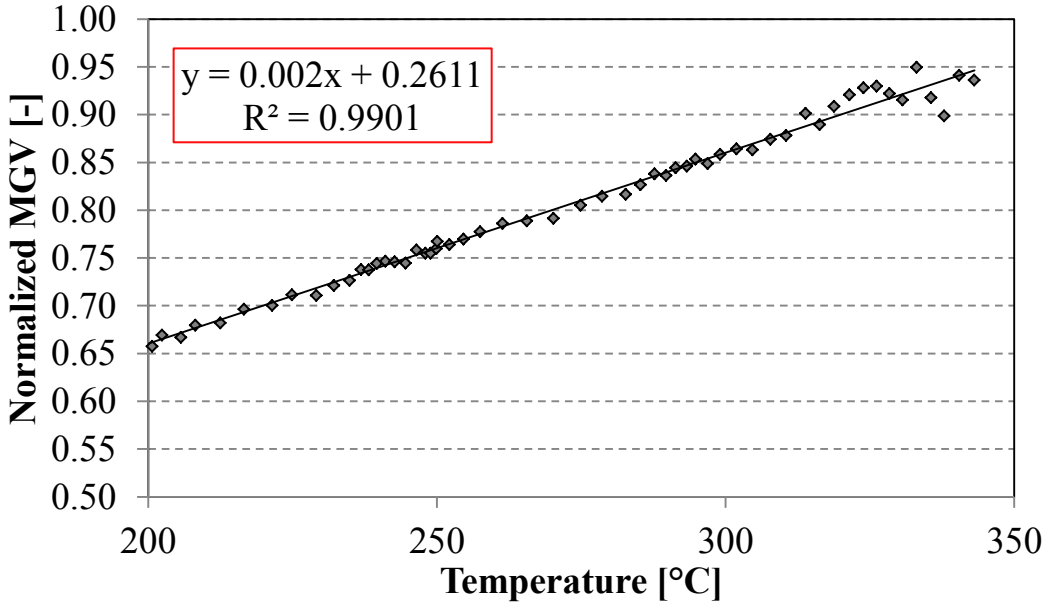

Figure 4.16: MGV as a function of temperature for Athabasca VR

Using the results from Figure 4.16, temperature effects from operation at different temperatures was negated though temperature normalization. This normalization extrapolates the linear data from Figure 4.16 into the reaction temperatures:

$$MGV_{Norm2}(t) = \frac{MGV_{Norm}(t)}{0.002T + 0.2611} \quad (Eq.\ 4.2)$$

Relative changes that in normalized MGV can be compared with the use of the normalization in Equation 4.2. Unless otherwise indicated, all plots for the remainder of this thesis that uses the normalized MGV refers to the normalized MGV derived from Equation 4.2. The use of the extrapolation assumes the trend remains linear as the medium progresses into reaction temperatures of 370 °C and higher. It is essentially impossible, to experimentally confirm this hypothesis because once reaction temperatures are reached, the MGV is also subjected to change due to cracking reactions. It is possible, however, to model this phenomenon by superimposing several terms that accounts for the MGV as a function of temperature, the decrease in MGV as it reacts and MGV increase upon the appearance of mesophase. This modeling work is not in the scope of this investigation and was not conducted. The concept of MGV curve deconstruction, however, is still useful as it provides a framework to determine which data is relevant for analysis. For feeds that undergo homogeneous fouling, the MGV can be divided into three separate stages:

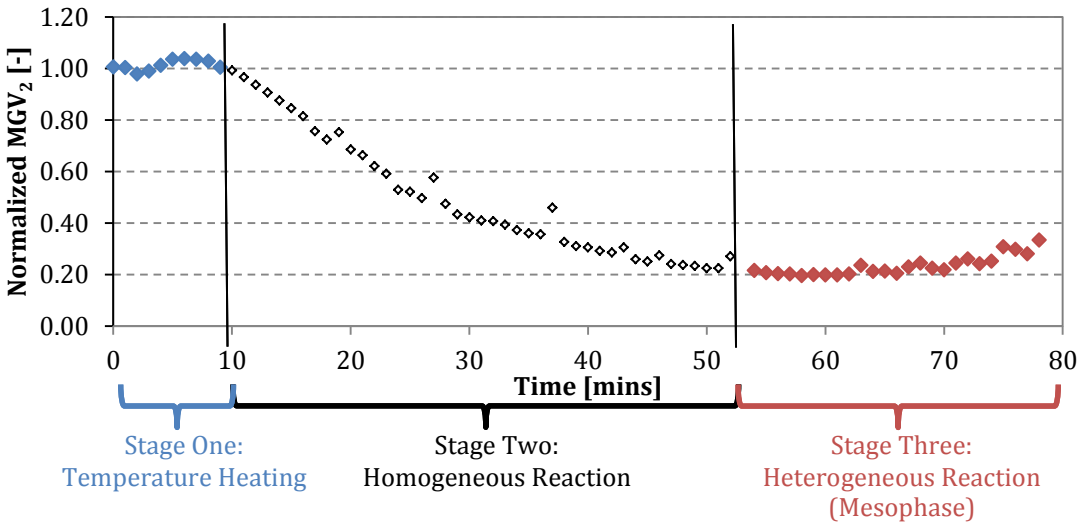

Figure 4.17: The three stages of a MGV plot for a homogeneous fouling feed

As previously discussed, stage one is characterized by an increase in MGV as this portion is subjected to the heating of the reaction medium. Stage two, is established after the desired reaction temperature is obtained and cracking reactions commence. Stage three starts once the onset of mesophase has occurred and the observation two distinct phases are detected. For a feed that undergoes dark film fouling, in the cases of Columbian and Gudao, the MGV curve also is sectioned into three stages.

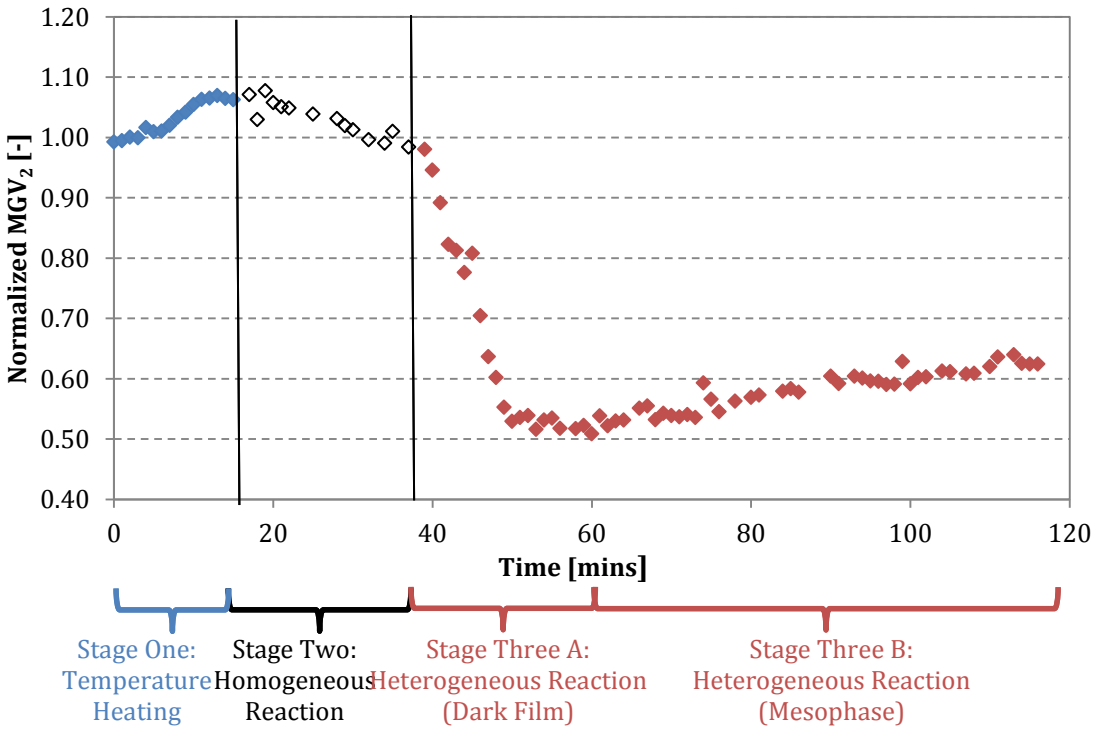

Figure 4.18: Various stages of a MGV plot for a heterogeneous fouling feed

The key difference being that stage three is subcategorized into two separate classes, with the first representing the appearance of the deposition of a dark film and the second the onset and growth of mesophase domains. It should be noted that the homogeneous and heterogeneous reaction stages are defined by their optical detection. As such these stages are limited to the optical resolution of the microscope. It is likely that smaller mesophase domains can exist before its optical onset.

In summary Section 4.2.1.2 presents a methodology to normalized the MGV though the use a quotient that is referred to as the normalization factor. The result of this normalization reduces the run-to-run variability due to light bulb artifacts or minute changes in microscopy settings as well as transient temperature effects. Additionally, the MGV curve was portioned into several sections for easy reference based on visual observations.

SECTION 4.2.1.3 MGV FITTING TO POWER LAW KINETICS

Mass based first order kinetics is commonly reported when investigating cracking reactions [44] [45] [46] [75] [47] [48] [50] [51]. It is unclear, however, if MGV is a first order phenomenon as it based on backscattering. To determine the kinetics of the change in MGV, the homogenous reaction stage experimental data is fitted to the integrated from of generalized rate expression to the n^{th} order. Assuming batch kinetics and an n^{th} order power law model the rate expression in terms of concentration, C, is developed as follows:

$$\frac{dC}{dt} = kC^n \ (Eq. 4.3)$$

$$\int_{C_0}^{C} \frac{dC}{C^n} = \int_0^t kdt \ (Eq. 4.4)$$

$$\frac{C^{1-n} - C_O^{1-n}}{(1-n)} = kt \ (Eq. 4.5)$$

Where C is the concentration, n is the order, t is the time elapse and k is the reaction rate constant for the n^{th} order. It is important to note that the generalized rate expression does not work for first order reactions. For first order reactions, the following was used instead:

$$\frac{dC}{dt} = kC \ (Eq. 4.6)$$

$$\int_{C_0}^{C} \frac{dC}{C} = \int_0^t kdt \ (Eq. 4.7)$$

$$ln\left(\frac{C}{C_0}\right) = kt \ (Eq\ 4.8)$$

Using Equations 4.3-4.8, the MGV was substituted for the concentration and fitted at various reaction orders. Previous studies report that the residue conversion is first order with respect to mass at low conversions. Results from this work agree with this assertion. The MGV data shows that the steady decrease in MGV is only for homogeneous reaction stage. At higher conversions the heterogeneous mesophase reverses this trend and the MGV starts its increase. Consequently, the heterogeneous section is not used for the subsequent analysis. Additionally, stage one was discarded as this portion was subjected to a heating ramp.

Using only the low conversion isothermal data, the MGV was fitted to various reaction orders using the integrated generalized form of the rate expression. Evaluations of the resulting fits were determined using the following error function:

$$Error\ Function = \sum abs\left(\frac{MGV_{i.Model} - MGV_{i.Experimental}}{MGV_{i.Model}}\right) \ (Eq.4.9)$$

Resulting fits are given in Figures 4.19-4.23 with parameters used to evaluate each order given in Table 4.4. Results show that the MGV linearizes best when first order kinetics is applied as indicated by both the minimal error and largest R^2 value.

Table 4.4: Results from MVG fitting to various orders

Order	Slope	R^2	Error
Zero Order	-2.54	0.97	0.2
0.5 Order	-3.03e-1	0.98	0.12
First Order	-3.82e-2	0.99	0.1
1.5 Order	-4.73e-3	0.98	0.14
Second Order	-6.20e-4	0.97	0.23

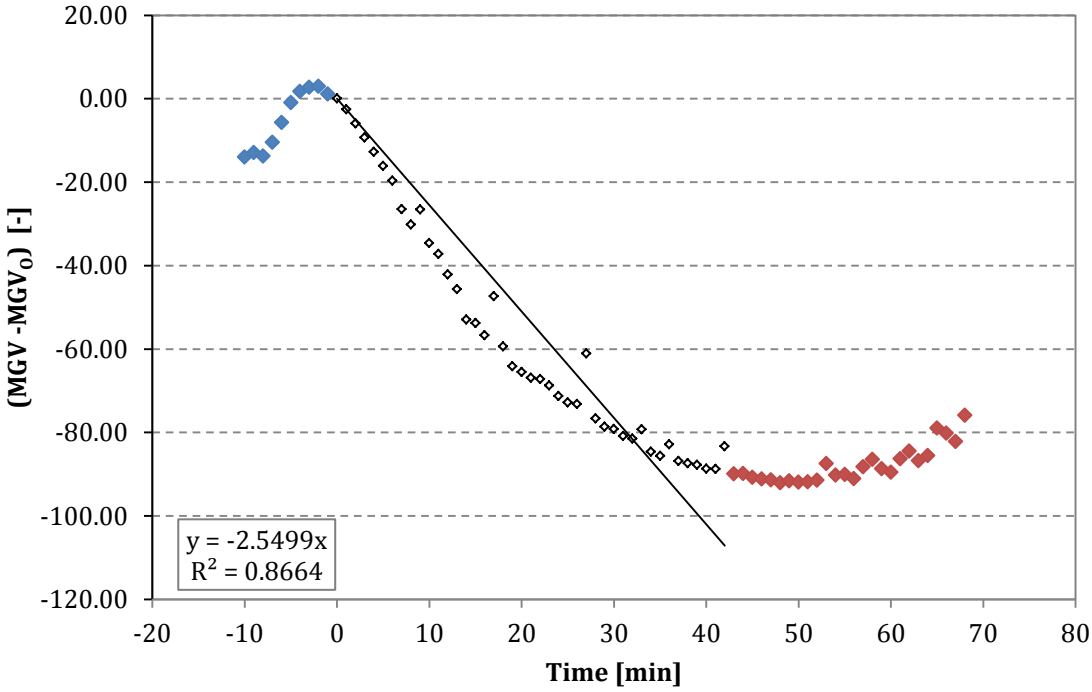

Figure 4.19: MGV data of Athabasca VR at 435 °C fitted to the zeroth order

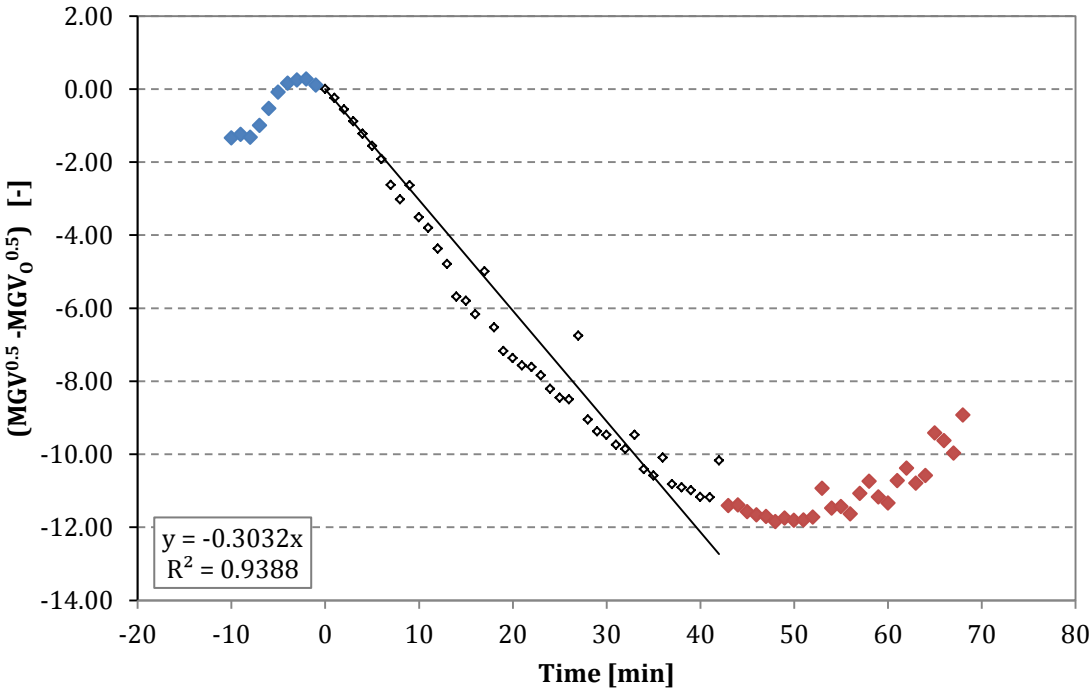

Figure 4.20: MGV data of Athabasca VR at 435 °C fitted to the 0.5th order

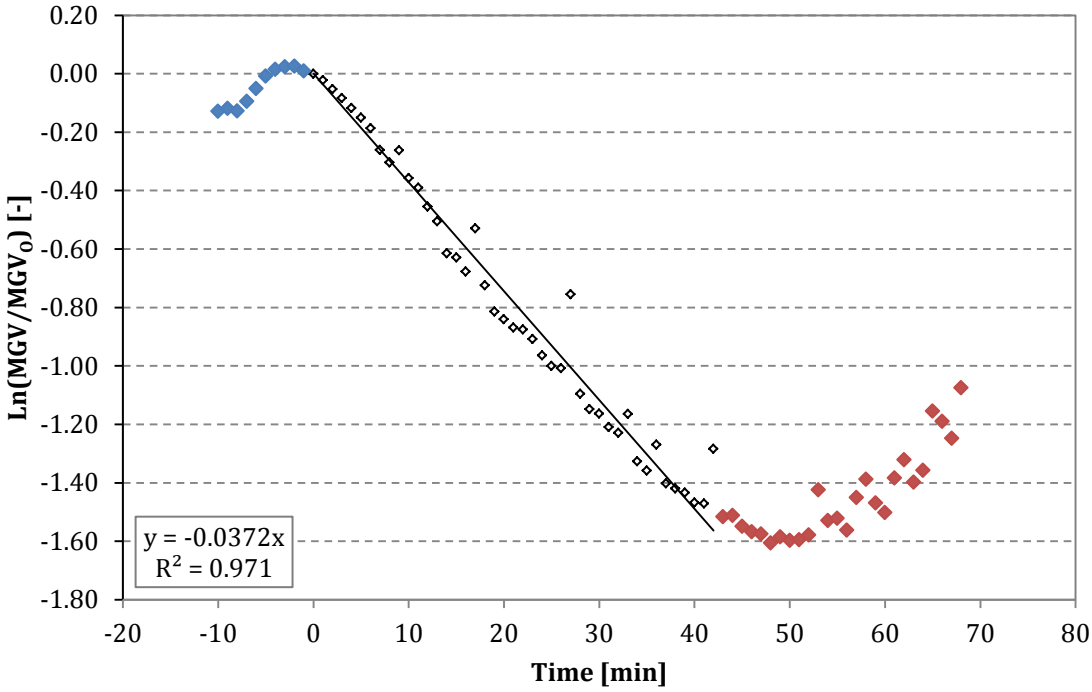

Figure 4.21: MGV data of Athabasca VR at 435 °C fitted to the first order

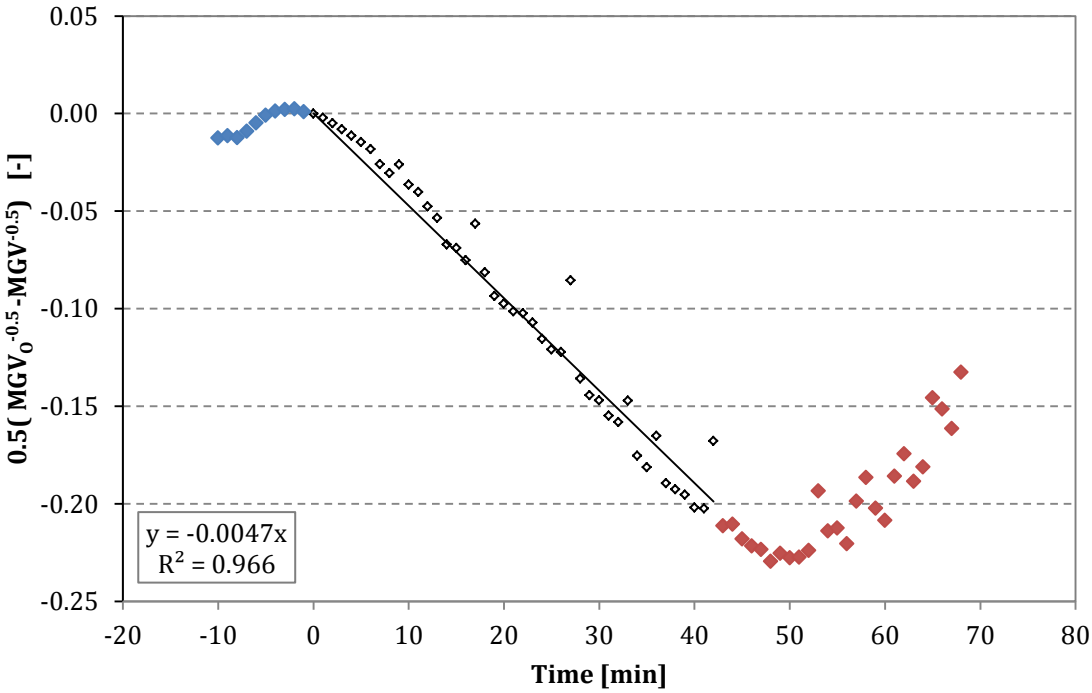

Figure 4.22: MGV of Athabasca VR at 435 °C data fitted to the 1.5th order

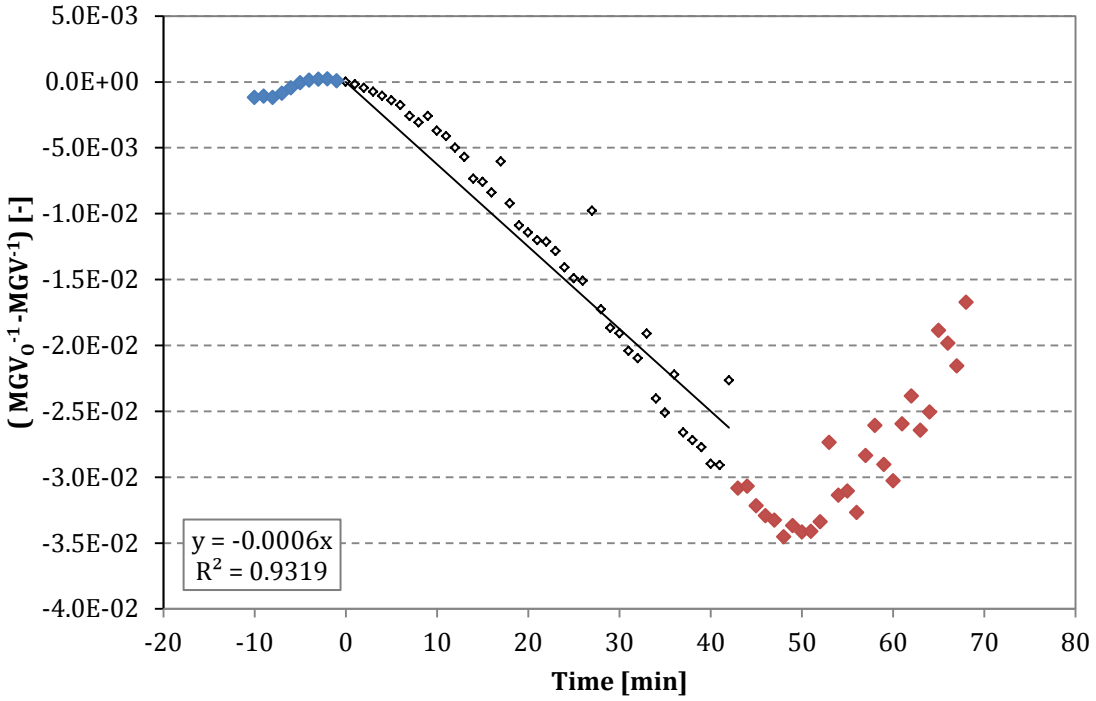

Figure 4.23: MGV data of Athabasca VR at 435 °C fitted to the second order

SECTION 4.2.1.4 SEVERITY INDEX

In an effort to compare different experiments at various temperatures, the severity index is introduced. The severity index captures the time temperature history of a reaction in a single parameter. This concept has been widely used in literature with varying complexity [76]. A simple model proposed by Geniesse and Reuter [77] suggested that the severity index is the real time multiplied by a power factor that doubles the reaction rate with an increase with every 17 °C with respect to their reference temperature of 480°C.

$$Severity\ Index = \left(2^{\frac{T-480}{17}}\right)(Real\ time)\ (Eq.4.10)$$

Of course, the doubling factor presented in Equation 4.10 is a crude approximation. A more complex model suggested Montane *et al*. [55] introduced a time dependent rate constant that changed as the reaction is carried out by modeling the overall activation energy as a distribution that changes with time. For this investigation the

severity index is derived from the integrated from of the generalized rate expression as follows:

$$\frac{C^{1-n} - C_O^{1-n}}{(1-n)} = kt \; (Eq. 4.5)$$

$$C^{1-n} = (1-n)k_1t_1 + C_O^{1-n} = (1-n)k_2t_2 + C_O^{1-n} \; (Eq. 4.11)$$

$$t_2 = \frac{k_1}{k_2}t_1 \; (Eq. 4.12)$$

Where k_1 and k_2 are the reaction rate constants at temperatures T_1 and T_2 respectively. Times t_1 and t_2 in Equation 4.12 are times at which equivalent conversion is achieved at the respective temperatures. The Arrhenius relationship can be substituted in for the rate constants:

$$k_i = Ae^{\left(\frac{-E_a}{RT_i}\right)} \; (Eq \; 4.13)$$

Where A is the pre-exponential factor, R is the universal gas constant and E_a is the activation energy. Resulting in the severity index:

$$Severity\ Index = SI_{T_2} = t_2 = \frac{k_1}{k_2}t_1 = e^{\frac{-E_a}{R}\left(\frac{1}{T_1} - \frac{1}{T_2}\right)}t_1 \; (Eq. 4.14)$$

The use of the generalized rate expression for the severity index derivation shows that the index is reaction order independent. For experiments that are non-isothermal, Equation 4.14 can be used in the integral form:

$$Severity\ Index = SI_{T_R} = \int e^{\left[\left(\frac{-E_a}{R}\right)\left(\frac{1}{T(t)} - \frac{1}{T_R}\right)\right]}dt \quad (Eq. 4.15)$$

For this investigation, the severity index was used in its summation form, as a result of only obtaining discretized data at one minute stages:

$$Severity\ Index = SI_{T_R} = \sum_{n=i}^{N} e^{\left[\left(\frac{-E_a}{R}\right)\left(\frac{1}{T_{ave}(t)_i} - \frac{1}{T_R}\right)\right]}\Delta t \; (Eq. 4.16)$$

Where Δt is the elapsed time stage and T_{ave} is the average temperature over this interval. The severity index was used to compare reactions at several temperatures by converting real time into an equivalent time at a given reference temperature. For this investigation, the reference temperature used was 420 °C. It follows that real times and severity index are equivalent when the reaction is carried out at reference temperature. For cases where the reaction temperature is higher than the reference, the resulting severity index is larger when compared to its real time equivalent. Conversely, a lower reaction temperature results in a relatively smaller severity. The relative magnitude at which the real time is altered when converted into severity index is highly dependent on the activation energy as shown in Equation 4.15.

The integrated batch design equation with first order kinetics can be combined with the concept of severity. This combination is achieved as follows:

$$ln\left(\frac{C}{C_0}\right) = k_1 t_1 = k_{ref} t_{ref} \ (Eq. 4.17)$$

$$n\left(\frac{C}{C_0}\right) = k_1 t_1 \left(\frac{k_{ref}}{k_{ref}}\right) \ (Eq. 4.18)$$

Substituting in the definition of severity index in Equation 4.14 into Equation 4.19:

$$ln\left(\frac{C}{C_0}\right) = k_{ref}\left(\frac{k_1 t_1}{k_{ref}}\right) = k_{ref} SI_{T_{ref}} \ (Eq. 4.19)$$

Equation 4.19 can be converted into one that employs the use of normalized MGV.

$$\ln(MGV_{Norm2}) = k_{ref} SI_{T_{ref}} (Eq. 4.20)$$

One consequence of using the severity index as proposed by Equation 4.20 is that experiments at different temperatures should all fall on the same line. The slope of this line is equivalent to the rate constant at the reference temperature. In addition, Equation 4.20 also suggests then that the resulting plots should not have a y-intercept.

Section 4.2.2 Determination of Activation Energy using Polarized Microscopy

Two methods of analysis are proposed to determine the cracking activation energy of several feeds. These methods used a modified form of Equation 4.20 where the definition of the severity index is substituted in.

$$\ln(MGV_{Norm2}) = k_{ref} SI_{T_{ref}} = k_{ref} \sum_{n=i}^{N} e^{\left[\left(\frac{-E_a}{R}\right)\left(\frac{1}{T_{ave(t)_i}} - \frac{1}{T_R}\right)\right]} \Delta t \ (Eq. 4.21)$$

It is clearly seen from Equation 4.21 that the activation energy is a key parameter when determining the severity index. The use of Equation 4.21 however, implies that there is no y-intercept. It is possible to modify the equation as follows:

$$\ln\left(\frac{MGV_{Norm2}}{\xi}\right) = k_{ref} \sum_{n=i}^{N} e^{\left[\left(\frac{-E_a}{R}\right)\left(\frac{1}{T_{ave(t)_i}} - \frac{1}{T_R}\right)\right]} \Delta t \ (Eq. \ 4.22)$$

$$\ln(MGV_{Norm2}) = k_{ref} \sum_{n=i}^{N} e^{\left[\left(\frac{-E_a}{R}\right)\left(\frac{1}{T_{ave(t)_i}} - \frac{1}{T_R}\right)\right]} \Delta t + \ln(\xi) \ (Eq. 4.23)$$

Where normalization error is accounted for by ξ and when factored out of the natural logarithm it allows for the MGV curves to be freely vertically translated on the plots. Both methods of analysis use Equation 4.23. The first method focuses on collapsing of normalized MGV data at several temperatures into a single linear plot at the reference temperature. The second method attempts to match slopes each individual data set of the normalized MGV while allowing the normalization factor to float. Details of each method are expanded upon in the sections below.

Section 4.2.2.1 Method 1: Collapsing the MVG Curve into One Line

Method one plots the natural logarithm of the normalized MGV against the calculated severity index. The resulting curves are linearly regressed into a single line by varying the activation energy in Equation 4.23 to minimize the value of the following objective function:

$$Objective\ Fucntion = \sum \text{abs}(MGV_{i,Predicted} - MGV_{i,Experimental}) \ \ (Eq. 4.24)$$

In essence, the use of severity factor with the appropriate activation energy will collapse of normalized MGV curves into a single curve at the reference temperature. Since lower temperatures react at a slower rate, the use of severities corrects the larger real time value into smaller value. Conversely, real times at higher temperatures are increased when converted into its equivalent severity. In this manner, an optimization was conducted using the Excel Solver tool to iterate until activation energy that minimized Equation 4.24 was determined. An activation energy that is too small results in low temperature severities that remain too large and severities at higher temperatures remain too small as shown in Figure 4.24.

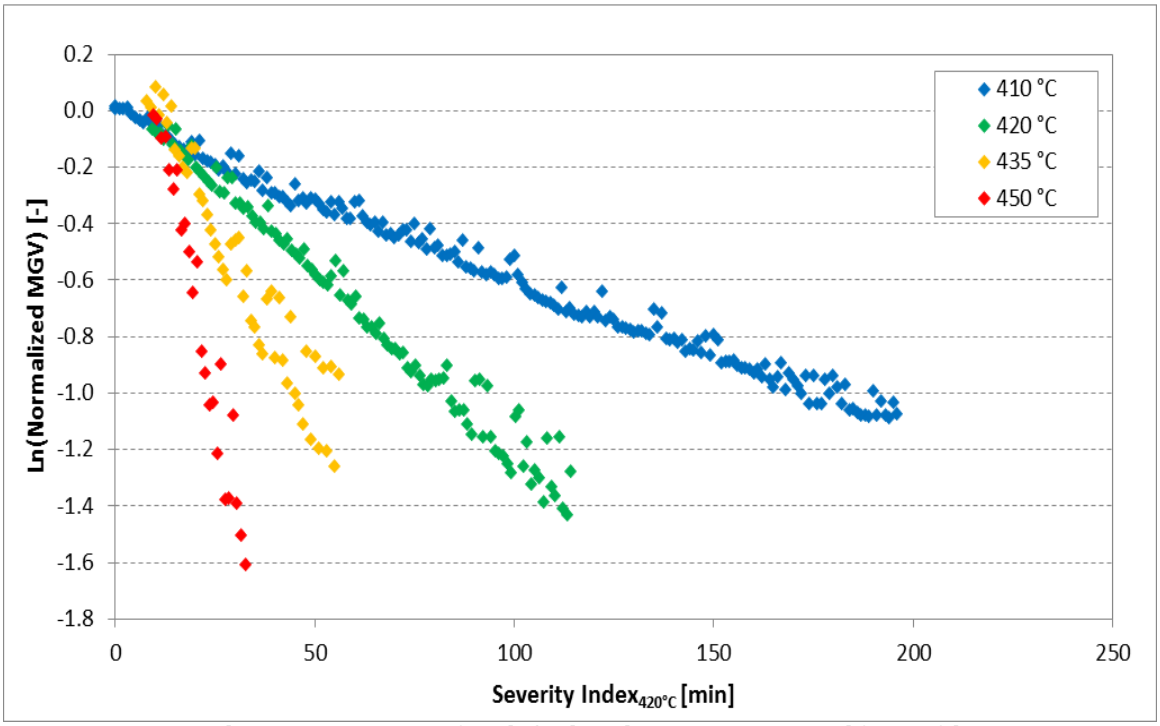

Figure 4.24: Using a low activation energy of 200 kJ/mol resulting in an unoptimized fitting of the MGV curves into a single curve into the reference temperature

Conversely, if the activation energy is too large, real times at lower temperatures and higher temperatures are shorten and extended too much respectively as illustrated in Figure 4.25. The optimal activation energy minimizes the objective function and results in the collapse the MGV curve into a single linear regressed line as depicted in Figure 4.26.

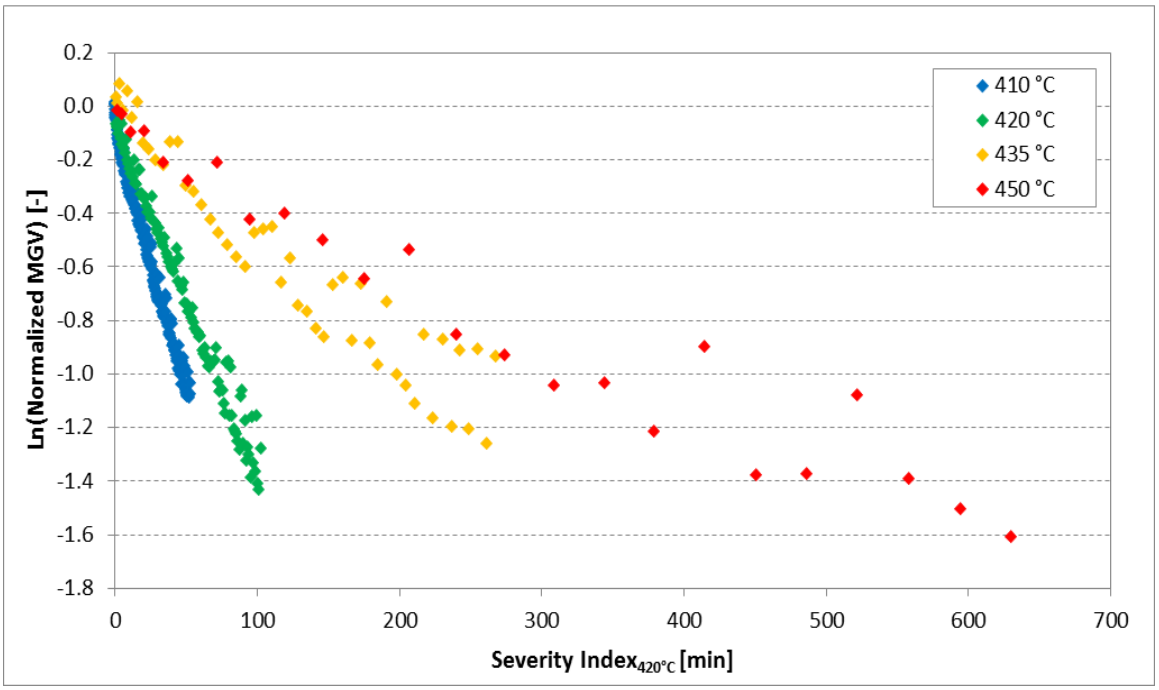

Figure 4.25: Using a large activation of 500 kJ/mol energy resulting in an unoptimized fitting of the MGV curves into a single curve into the reference temperature

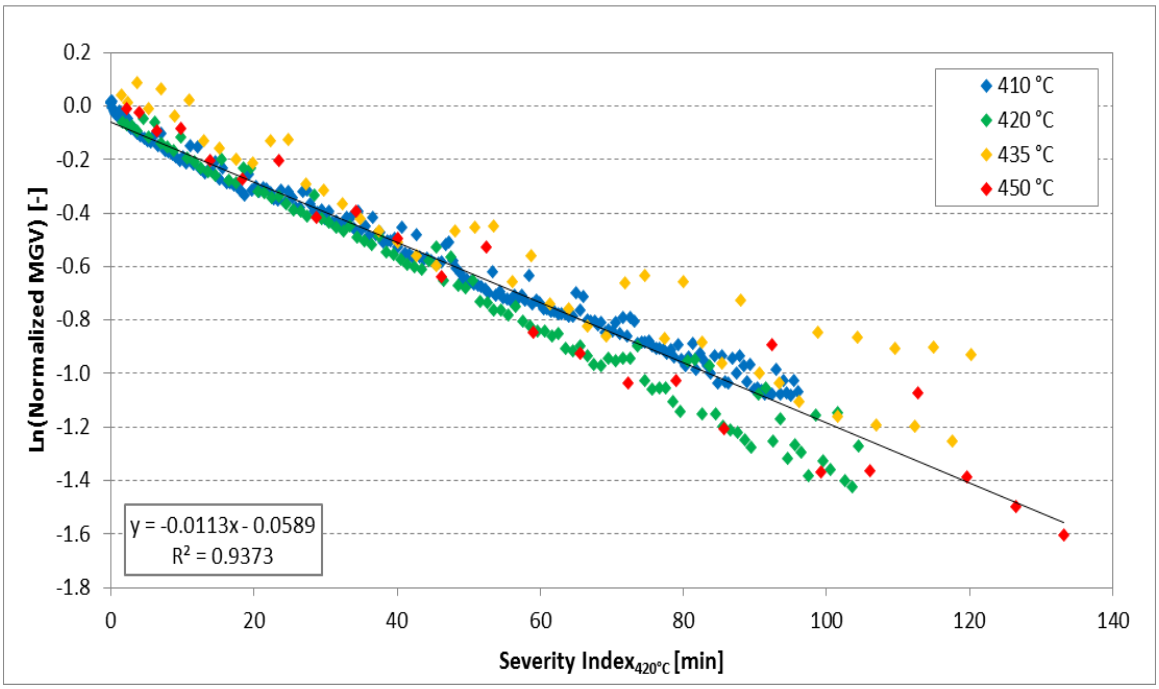

Figure 4.26: Optimized activation energy at 267.4 kJ/mol for Cold Lake bitumen MGV curves into a single curve into the reference temperature

It is possible to use Equation 4.21 rather than 4.23 for this analysis which forces the optimization to pass the regressed line through the origin as shown in Figure 4.27.

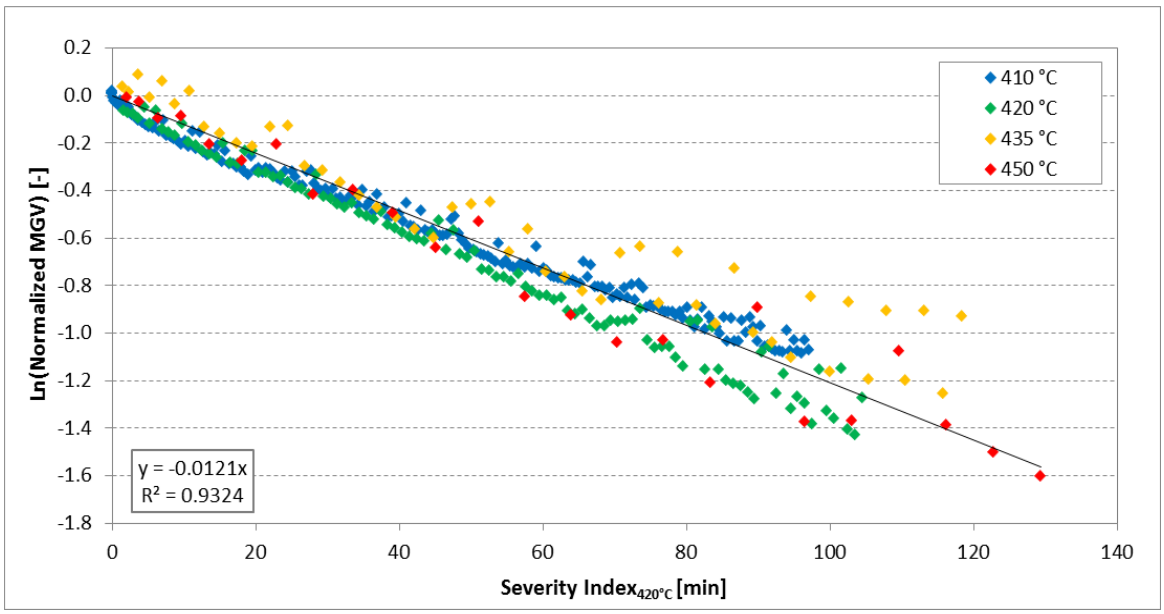

Figure 4.27: Optimized activation energy at 262.9 kJ/mol for Cold Lake bitumen MGV curves into a single curve into the reference temperature forcing the regressed line pass the origin

Results from Figures 4.26 and 4.27 show that for Cold Lake bitumen, not much difference is observed when forcing the y-intercept of the regression to zero. Similar slopes, r-squared values and activation energies indicate that there is not much error in the normalization. This is not the case for the Safaniya VR as shown in Figure 4.31 where the y-intercept is much larger. Normalization errors are expected as the temperature normalization was based off of data for Athabasca VR. To reduce this error, it is recommended that slow temperature ramps be completed for each individual feed. Thus, the use of Equation 4.23 was employed for method one.

Resulting plots of the normalized MGV against optimized severity times obtained from using method one are given below in Figures 4.28, 4.34, 4.41, 4.45, 4.51 and 4.55, these figures also contain the optimized regressed line obtained after all data was collapsed onto the reference temperature curve. The 95% confidence intervals are also reported in the y-intercept values in Tables 4.5 to 4.10. The confidence intervals are not shown on the plots as they were too small to observe when drawn to scale on the plots. Residual plots were also generated to show the spread of the data with respect to the regressed line, and are shown in Figures 4.31, 4.32, 4.39,

4.46, 4.48 and 4.54. Residual plots also show the standard deviation of the data as indicated by the dashed lines on these graphs.

It is important to note that the use of method one has a bias towards lower reaction temperatures, since lower temperatures take longer to conduct; they also contain more data points. Using the objective function in Equation 4.24 above gives equal weighting to each individual data point, and as such will skew results towards lower temperature trials. This is seen for the Safaniya, Columbian and Gudao VR in Figures 4.34, 4.41 and 4.51 respectively, where the higher temperature trials and particularly the 450 °C have the poorest fit. This can be remediated by modifying the objective function to:

$$Objective\ Func. = \sum_{i=1}^{n} \frac{\sum_{j=1}^{m} abs(MGV_{Predicted,j} - MGV_{Experimental,j})}{m_i} \quad (Eq. 4.25)$$

Where n is the number of experiments conducted, and m_i is the number of data points for a particular run. This objective function determines the average error of each trial and then gives equal weighting to each data set rather than each individual data point. The objective function in Equation 4.25 is used only for the Columbian, Safaniya and Gudao VR data as these results have poor fits for the higher temperature trials. Results using Equation 4.25 for optimization are given in Figures 4.33, 4.40 and 4.50 with residuals shown in Figures 4.35, 4.38 and 4.49.

Section 4.2.2.2 Method 2: Matching Slopes of Isothermal Data

Similar to the first method, method two also varies the activation energy to determine an ideal fit. Instead of solely varying the activation energy however, this method also allows the normalization factors of each data set to float. To take this into account Equation 4.21 is manipulated as follows:

$$\ln(MGV_{Norm2})_i = k_{ref,i} \sum_{n=i}^{N} e^{\left[\left(\frac{-E_a}{R}\right)\left(\frac{1}{T_{ave}(t)_i} - \frac{1}{T_R}\right)\right]} \Delta t + ln(\xi_i) \quad (Eq. 4.26)$$

Where the ξ_i and $k_{ref,i}$ refers to the individual normalization error and slope of each data set. Thus, the objective of method two is not to collapse all the MGV data into a

single line, rather it is to determine an activation energy where the slopes of all of the data sets are equivalent. The resulting objective function for this method is to minimize the variance between each of the slopes.

$$Obj.Func.M2 = \sigma_{slopes} \ (Eq. 4.27)$$

Where σ_{slopes} is the standard deviation of the slopes, the results of such an optimization process are plots that feature parallel MGV curves. Resulting plots after optimization are shown in Figures 4.29, 4.37, 4.43, 4.44, 4.53 and 4.57. Residual plots are also provided in Figures 4.30, 4.36, 4.42, 4.47, 4.25 and 4.56. Method two results in multiple regressed lines, the residuals are calculated with respect to each individual data set.

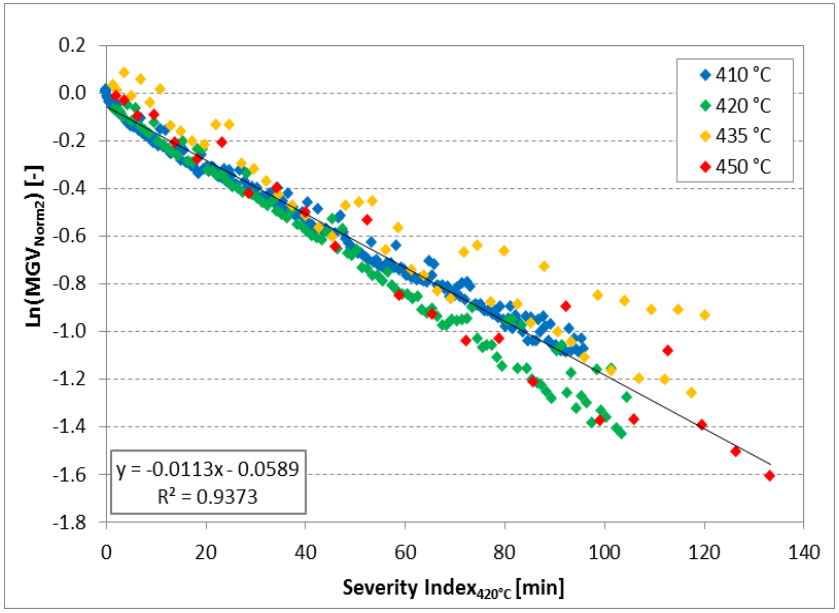

Figure 4.28: Method one optimization of Cold Lake bitumen

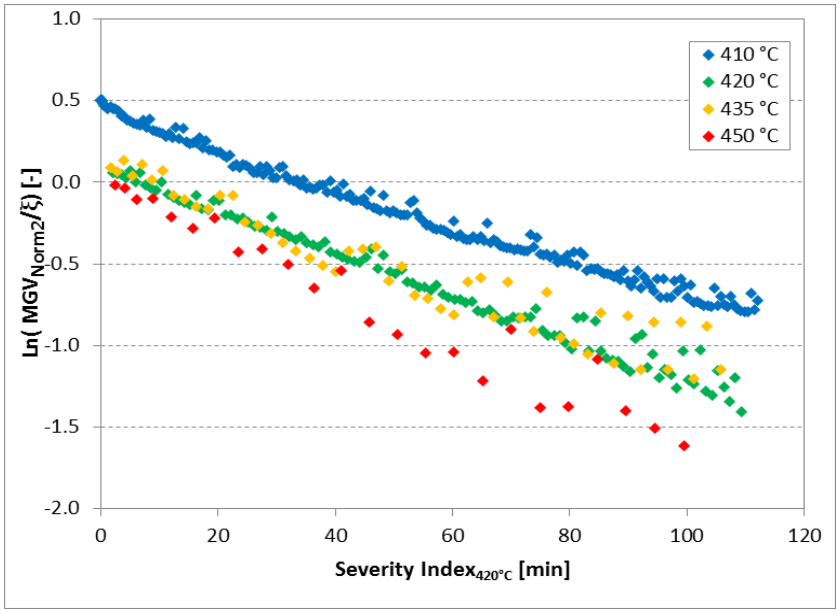

Figure 4.29: Method two optimization of Cold Lake bitumen

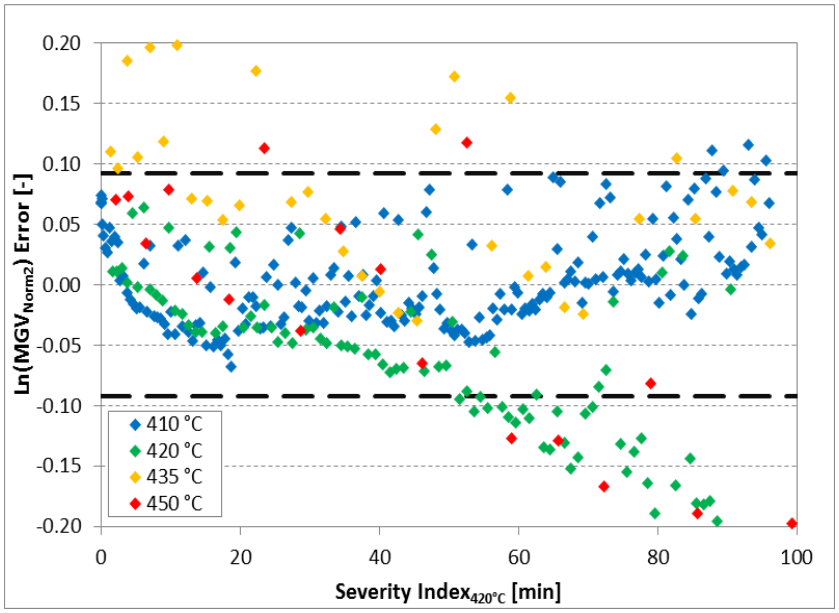

Figure 4.31: Resulting residuals from method one of analysis of Cold Lake bitumen

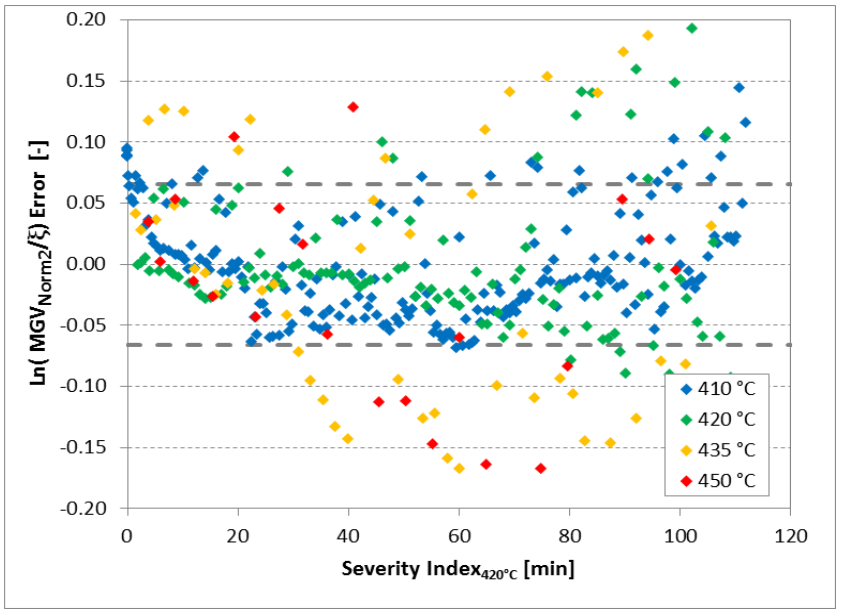

Figure 4.30: Resulting residuals from method two of analysis of Cold Lake bitumen

Table 4.5: Important parameters from analysis for Cold Lake bitumen

Parameter	Units	Method 1	Method 2
Activation Energy	[kcal/mol]	63.3	53.1
	[kJ/mol]	267.4	222.1
Slope	[-]	-1.12e-2	-1.35e-2
Y-Intercept	[-]	-5.09e-2 ±9.388e-3	Not Relevant
R^2 Value	[-]	0.94	Not Relevant
Standard Deviation of Slopes	[-]	Not Relevant	1.86e-3
Standard Deviation of Data	[-]	±9.22e-2	Not Relevant

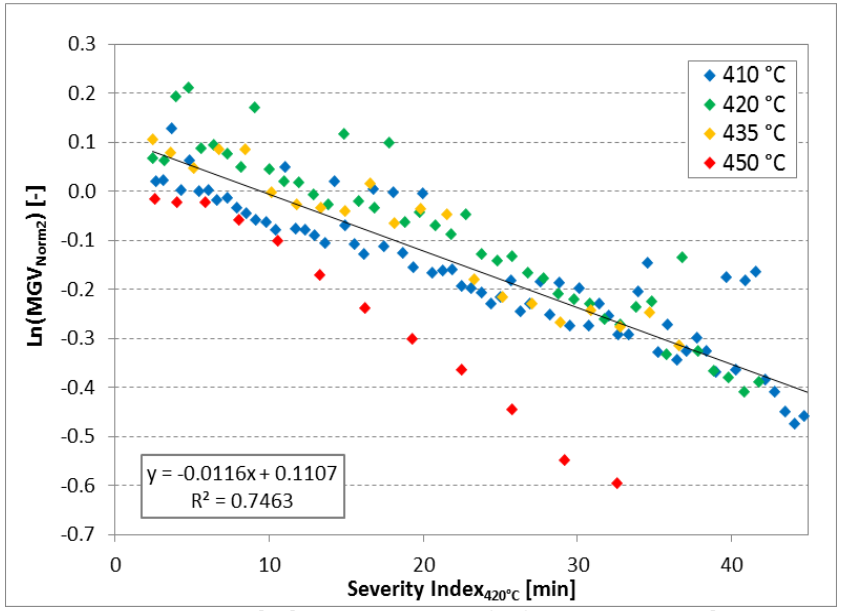

Figure 4.34: Method one optimization of Safaniya vacuum residue

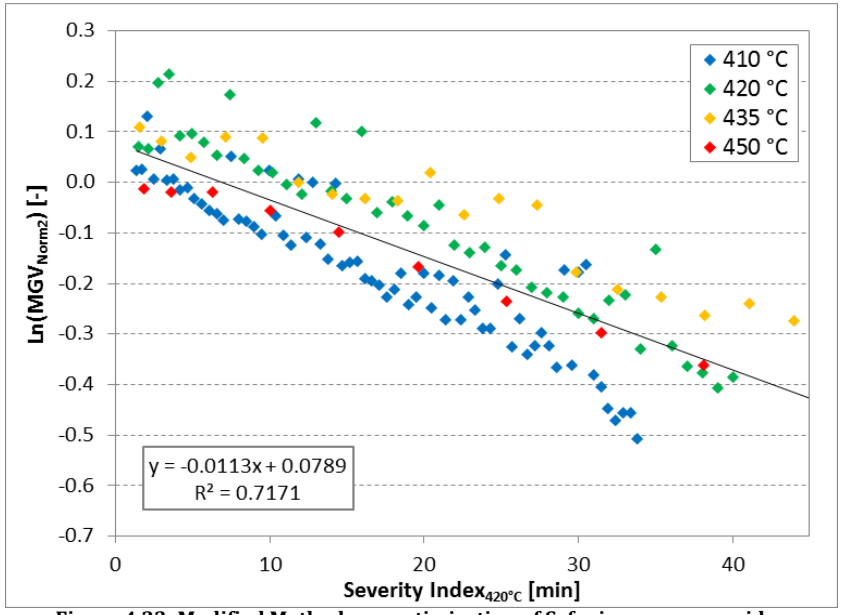

Figure 4.33: Modified Method one optimization of Safaniya vacuum residue

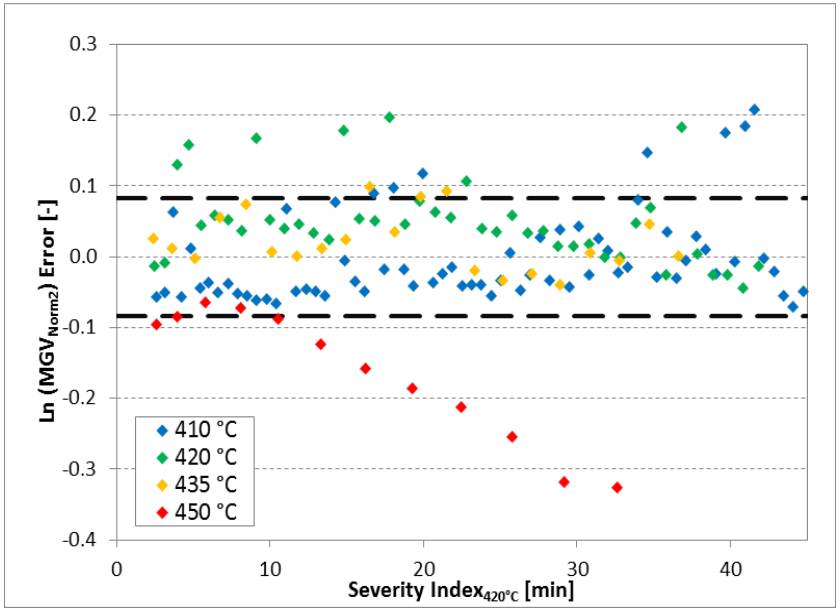

Figure 4.32: Resulting residuals from method one of analysis of Safaniya vacuum residue

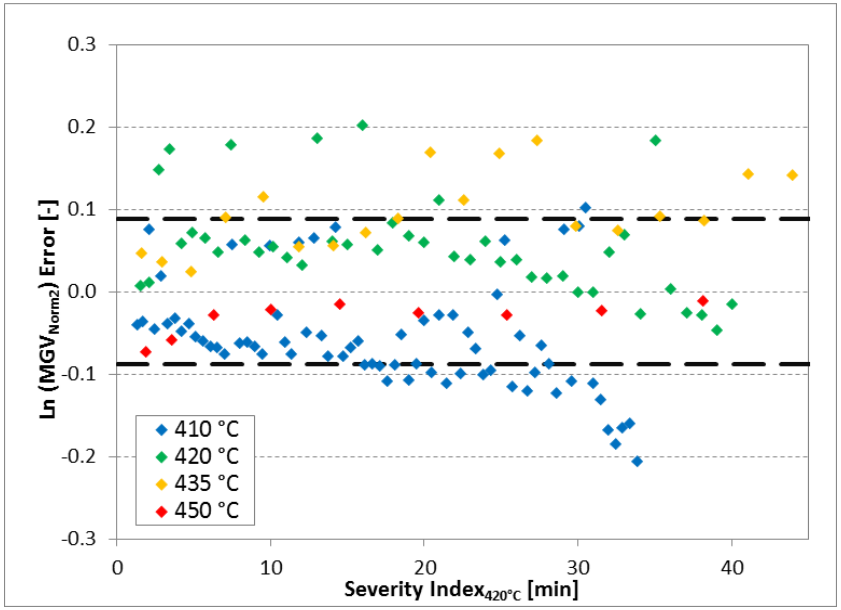

Figure 4.35: Resulting residuals from modified method one of analysis of Safaniya vacuum residue

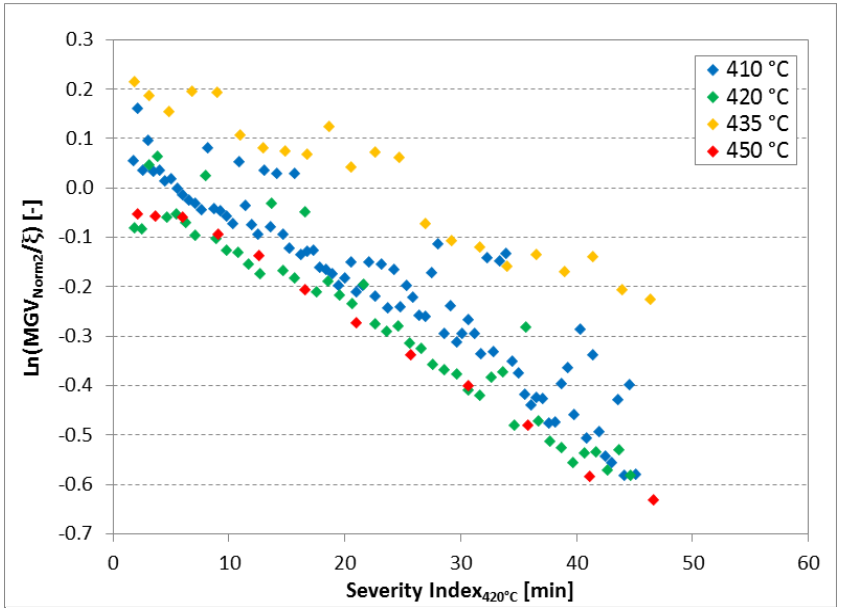

Figure 4.37: Method two optimization of Safaniya vacuum residue

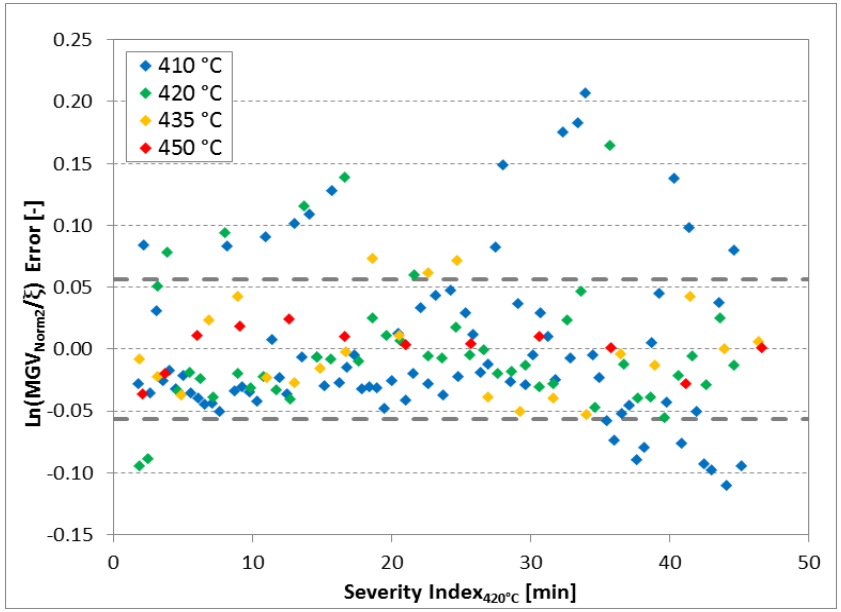

Figure 4.36: Resulting residuals from method two of analysis of Safaniya vacuum residue

Table 4.6: Important parameters from analysis for Safaniya vacuum residue

Parameter	Units	Method 1	Modified Method 1	Method 2
Activation Energy	[kcal/mol]	42.7	69.4	58.9
	[kJ/mol]	178.8	290.6	283.5
Slope	[-]	-1.16e-2	-1.13e-2	-1.28e-2
Y-Intercept	[-]	0.11 ±1.38e-2	0.08 ± 1.46e-2	Not Relevant
R^2 Value	[-]	0.75	0.71	Not Relevant
Standard Deviation of Slopes	[-]	Not Relevant	Not Relevant	1.69e-2
Standard Deviation of Data	[-]	±0.08	±0.09	Not Relevant

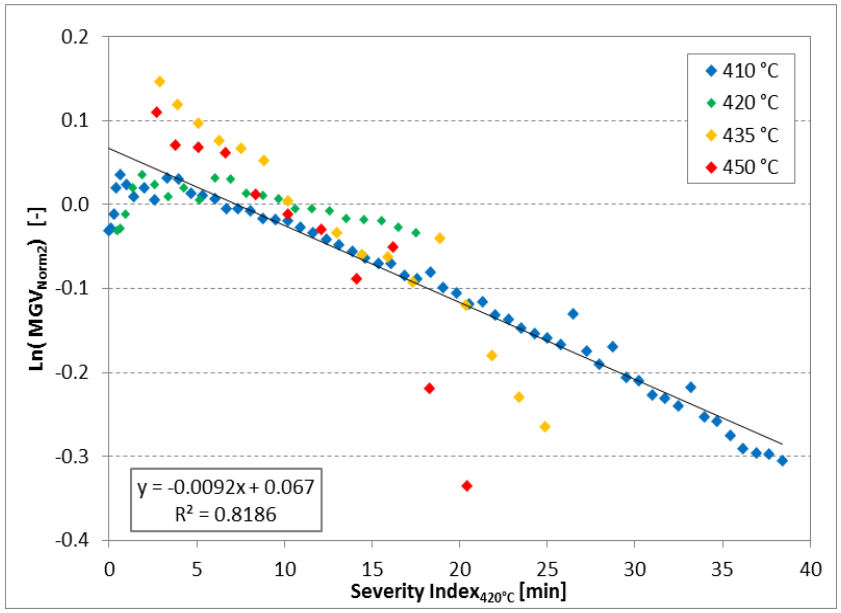

Figure 4.41: Method one optimization of Columbian vacuum residue

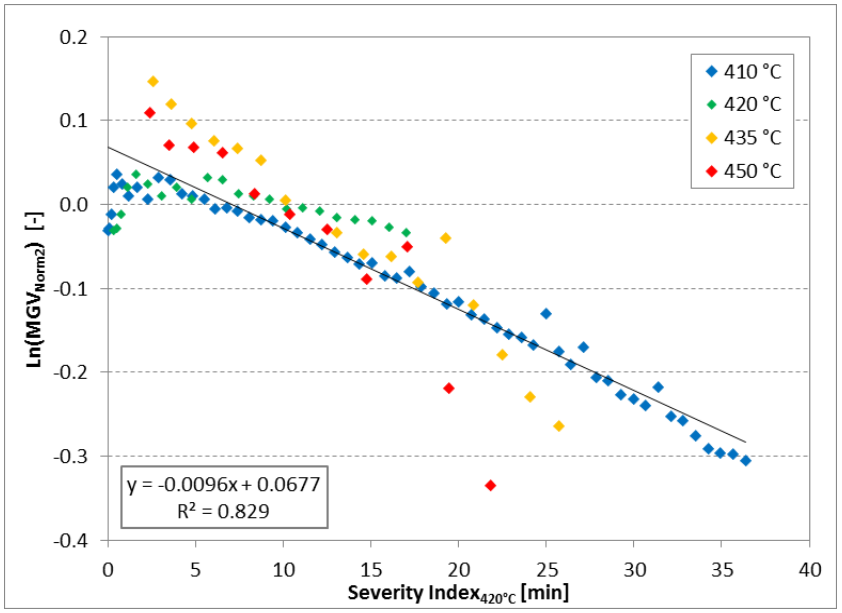

Figure 4.40: Modified method one optimization of Columbian vacuum residue

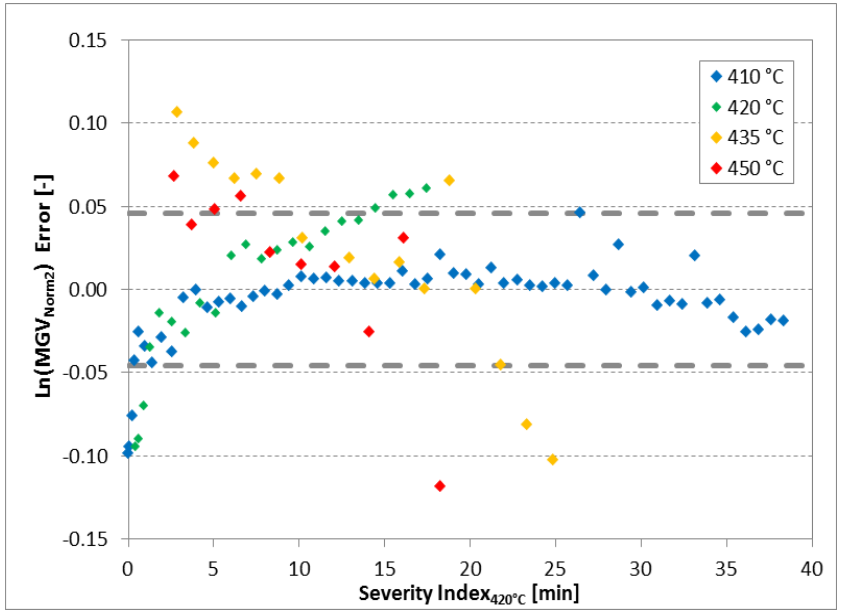

Figure 4.39: Resulting residuals from method one of analysis of Columbian vacuum residue

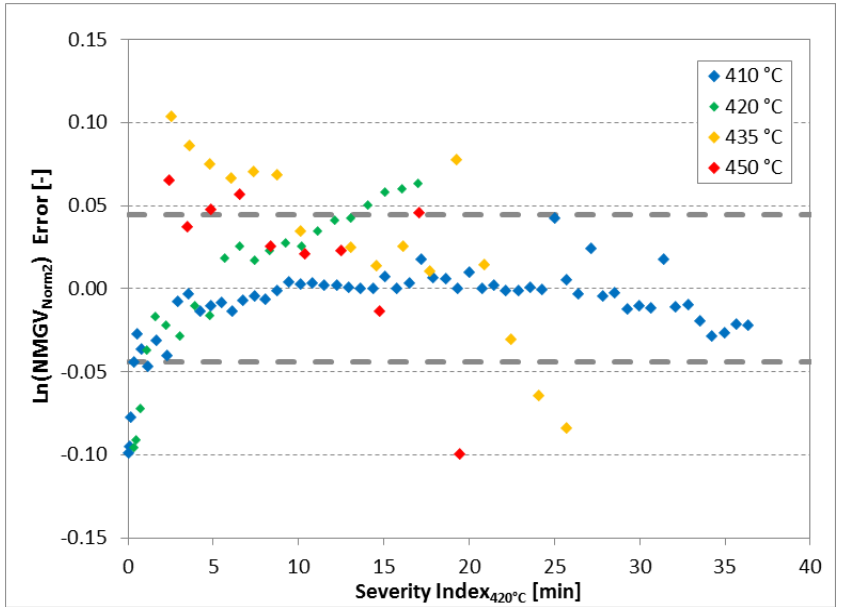

Figure 4.38: Resulting residuals from modified method one of analysis of Columbian vacuum residue

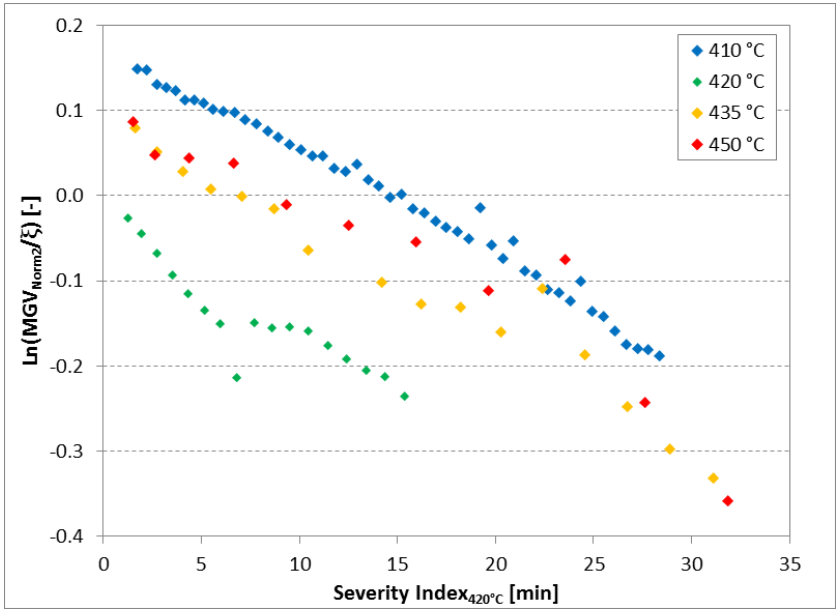

Figure 4.43: Method two optimization of Columbian vacuum residue

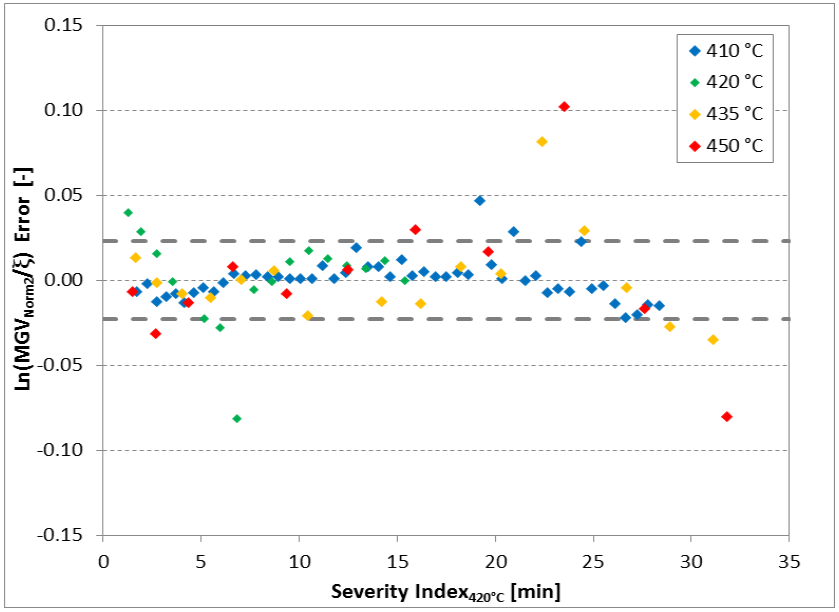

Figure 4.42: Resulting residuals from method two of analysis of Columbian vacuum residue

Table 4.7: Important parameters from analysis for Columbian vacuum residue

Parameter	Units	Method 1	Modified Method 1	Method 2
Activation Energy	[kcal/mol]	28.0	32.3	52.7
	[kJ/mol]	117.1	135.4	220.6
Slope	[-]	-9.19e-3	-9.64e-2	-1.22e-2
Y-Intercept	[-]	0.07 ±8.82e-2	.07±8.57e-2	Not Relevant
R^2 Value	[-]	0.82	0.83	Not Relevant
Standard Deviation of Slopes	[-]	Not Relevant	Not Relevant	1.07e-4
Standard Deviation of Data	[-]	±0.05	±0.04	Not Relevant

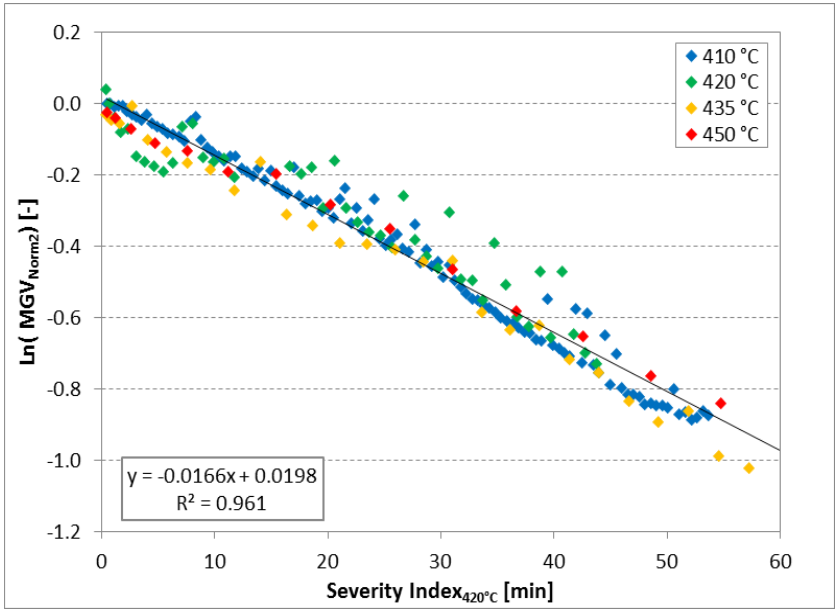

Figure 4.45: Method one optimization of Cerro Negro crude oil

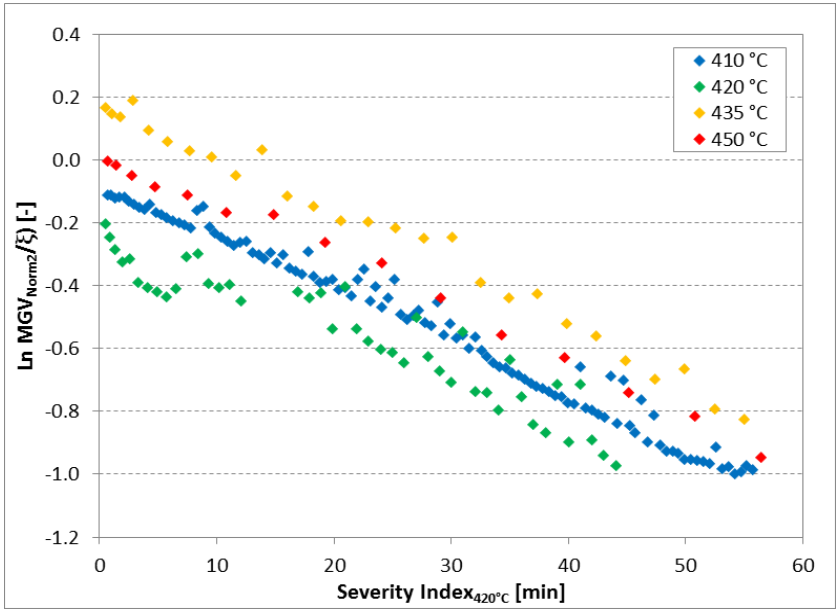

Figure 4.44: Method two optimization of Cerro Negro crude oil

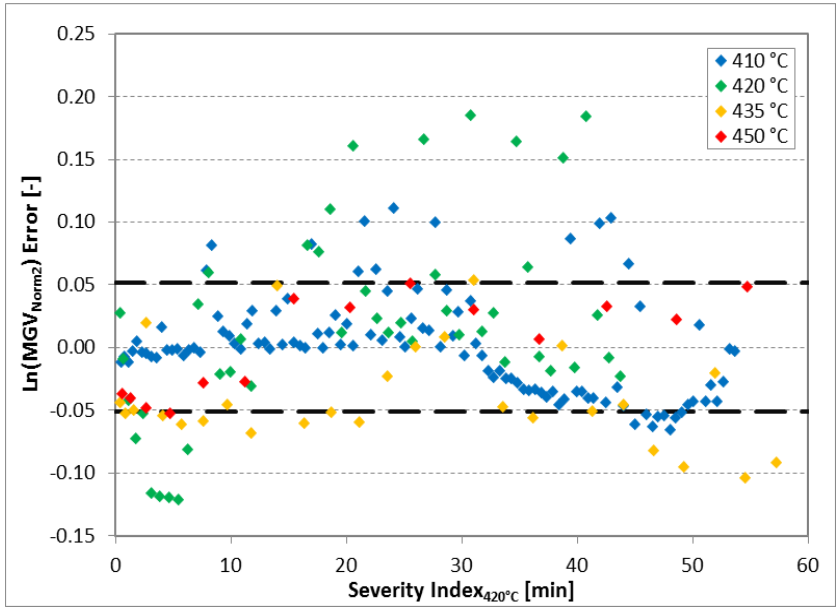

Figure 4.46: Resulting residuals from method one of analysis of Cerro Negro crude oil

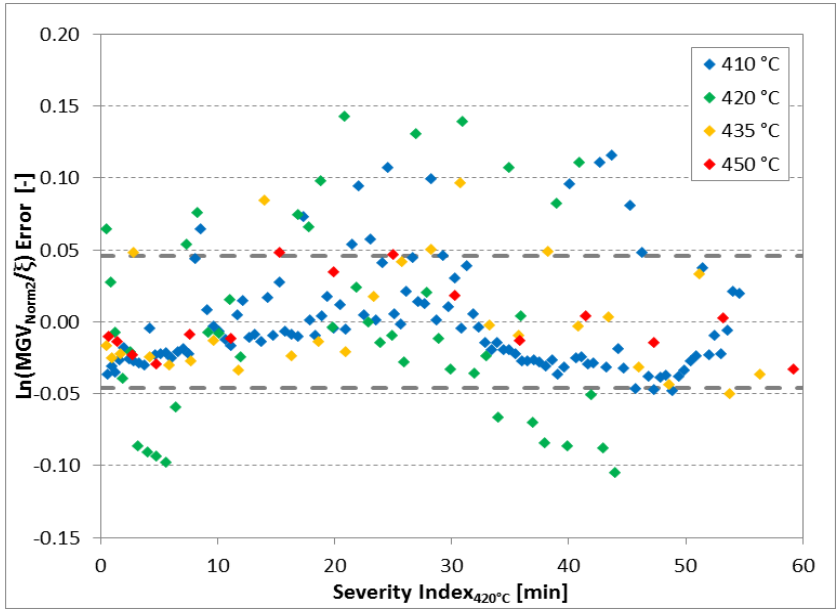

Figure 4.47: Resulting residuals from method two of analysis of Cerro Negro crude oil

Table 4.8: Important parameters from analysis for Cerro Negro crude oil

Parameter	Units	Method 1	Method 2
Activation Energy	[kcal/mol]	63.5	60.2
	[kJ/mol]	265.8	252.1
Slope	[-]	-1.66e-2	-1.71E-2
Y-Intercept	[-]	0.02 ±	Not Relevant
R^2 Value	[-]	0.96	Not Relevant
Standard Deviation of Slopes	[-]	Not Relevant	5.66E-4
Standard Deviation of Data	[-]	±0.05	Not Relevant

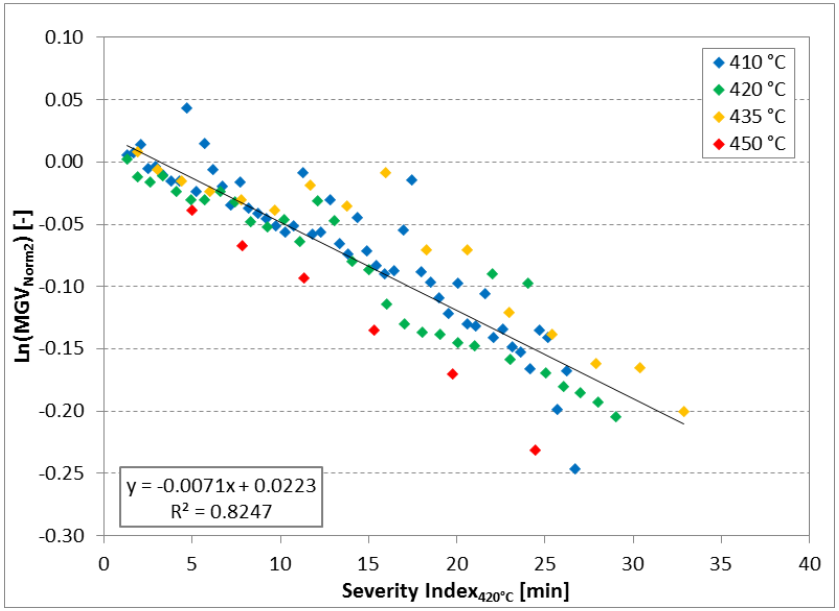

Figure 4.51: Method one optimization of Gudao vacuum residue

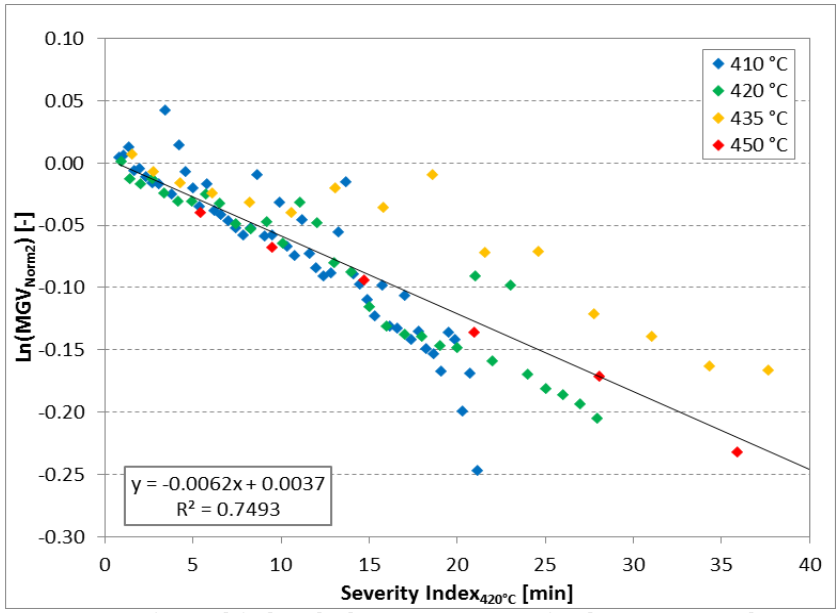

Figure 4.50: Modified method one optimization of Gudao vacuum residue

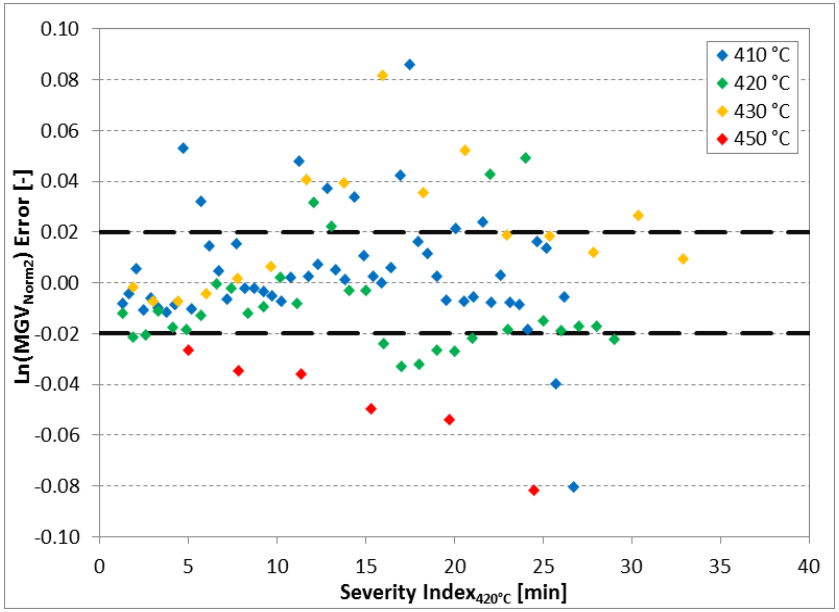

Figure 4.48: Resulting residuals from method one of analysis of Gudao vacuum residue

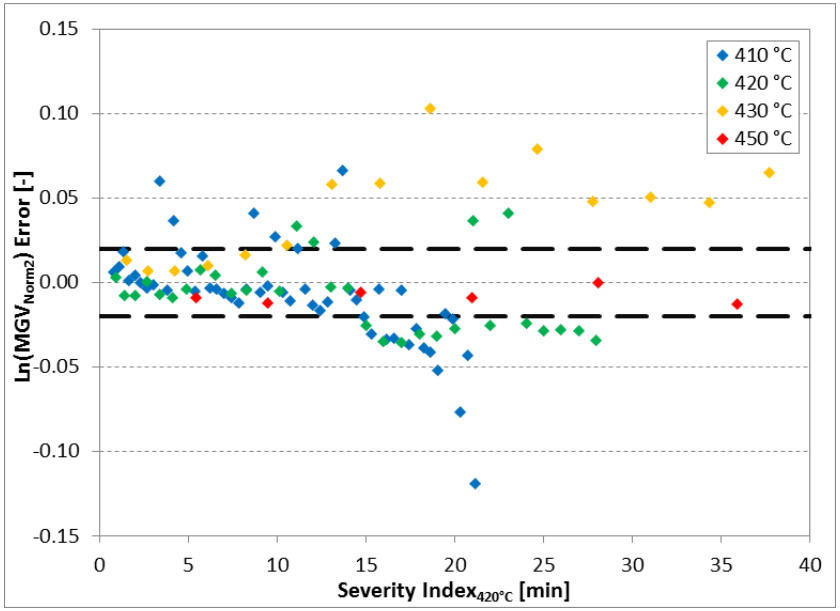

Figure 4.49: Resulting residuals from modified method one of analysis of Gudao vacuum residue

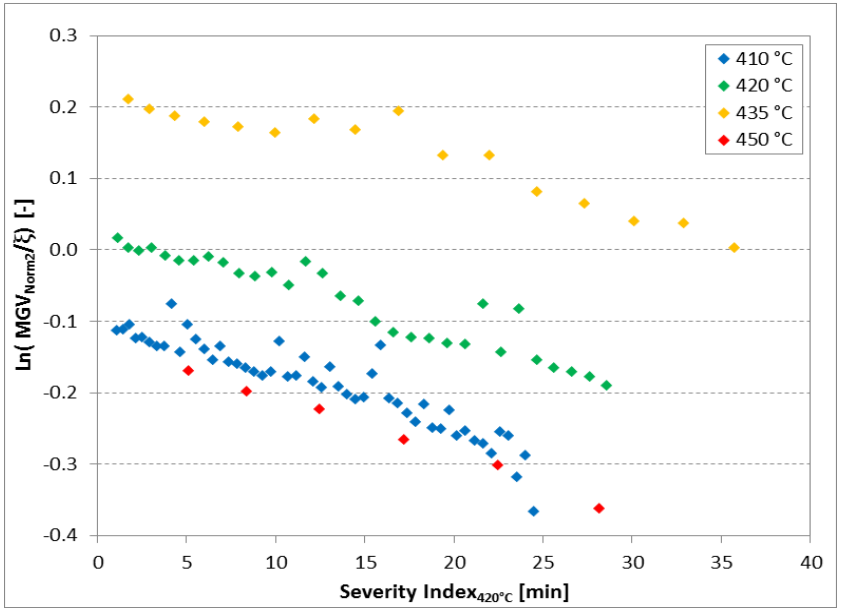

Figure 4.53: Method two optimization of Gudao vacuum residue

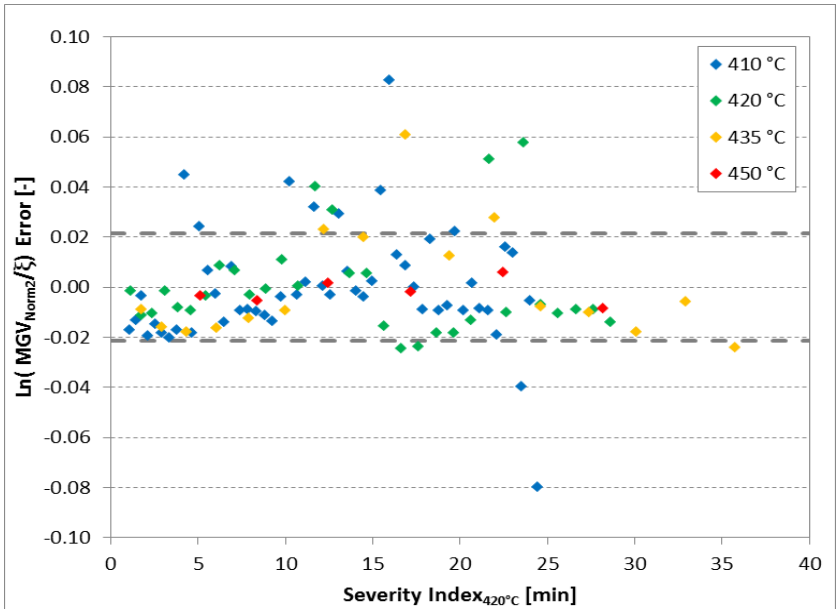

Figure 4.52: Resulting residuals from modified method two of analysis of Gudao vacuum residue

Table 4.9: Important parameters from analysis for Gudao vacuum residue

Parameter	Units	Method 1	Modified Method 1	Method 2
Activation Energy	[kcal/mol]	62.4	82.6	70.0
	[kJ/mol]	261.2	345.6	293.2
Slope	[-]	-7.07e-3 ± 5.23e-3	-6.23e-3 ±6.32e-3	-7.26e-3
Y-Intercept	[-]	0.02	0.02	Not Relevant
R^2 Value	[-]	0.82	0.00	Not Relevant
Standard Deviation of Slopes	[-]	Not Relevant	Not Relevant	1.18e-3
Standard Deviation of Data	[-]	±0.02	±0.02	Not Relevant

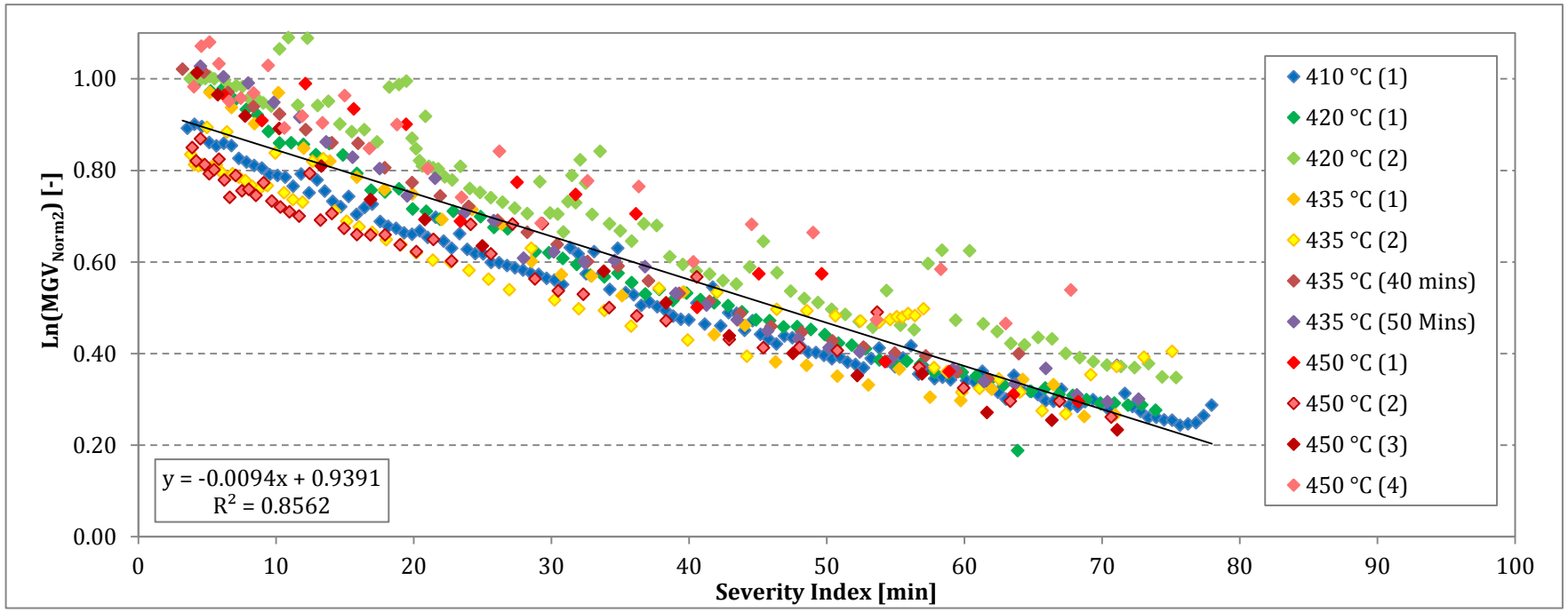

Figure 4.55: Method one optimization of Athabasca vacuum residue

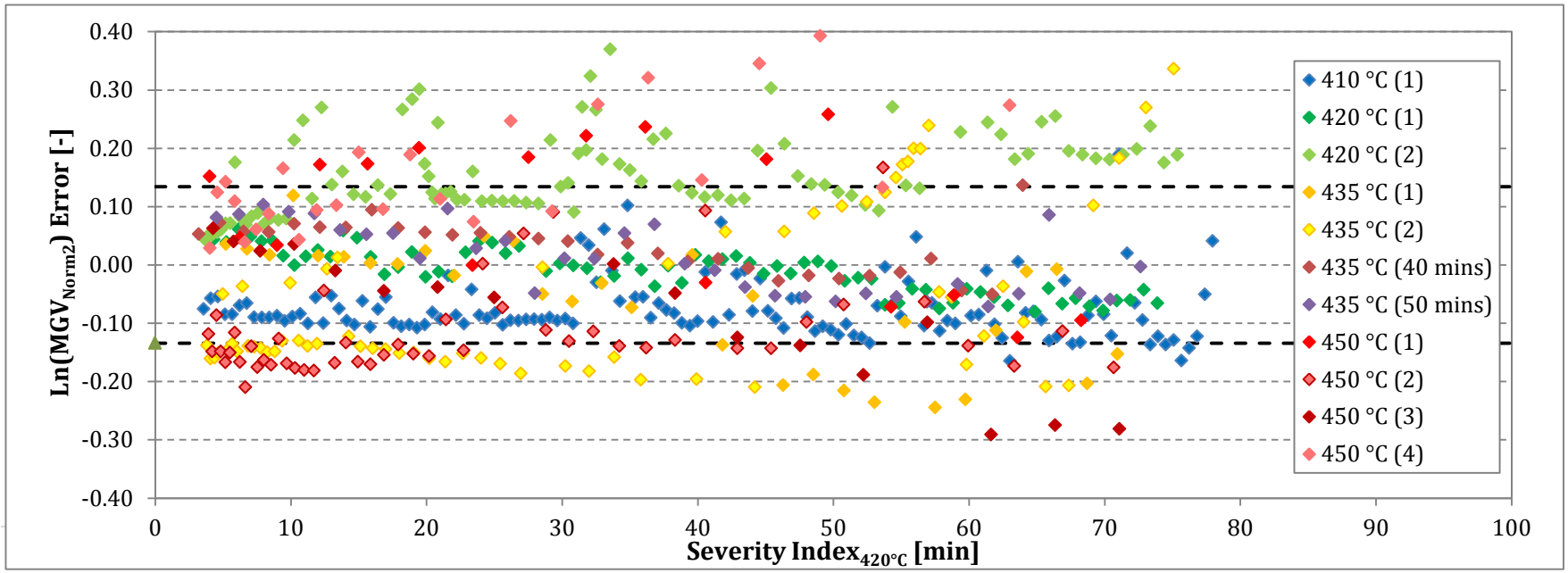

Figure 4.54: Resulting residuals from method one of analysis of Athabasca vacuum residue

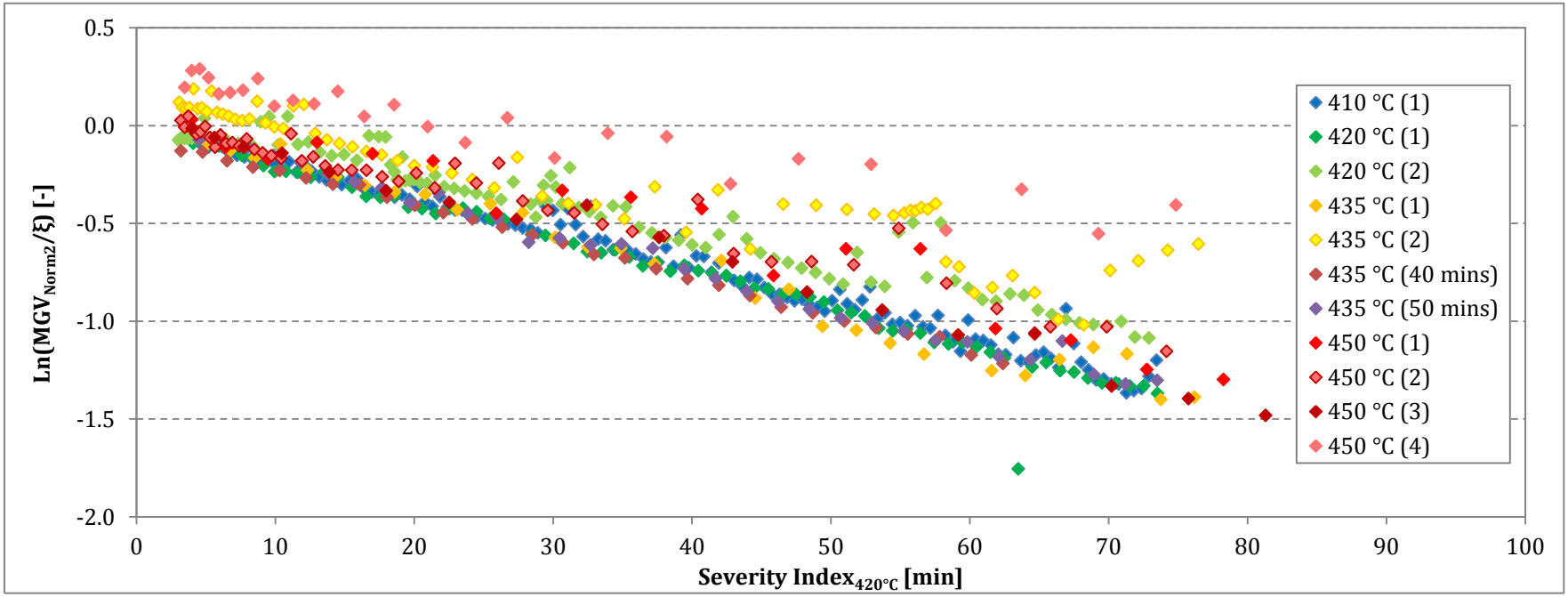

Figure 4.57: Method two optimization of Athabasca vacuum residue

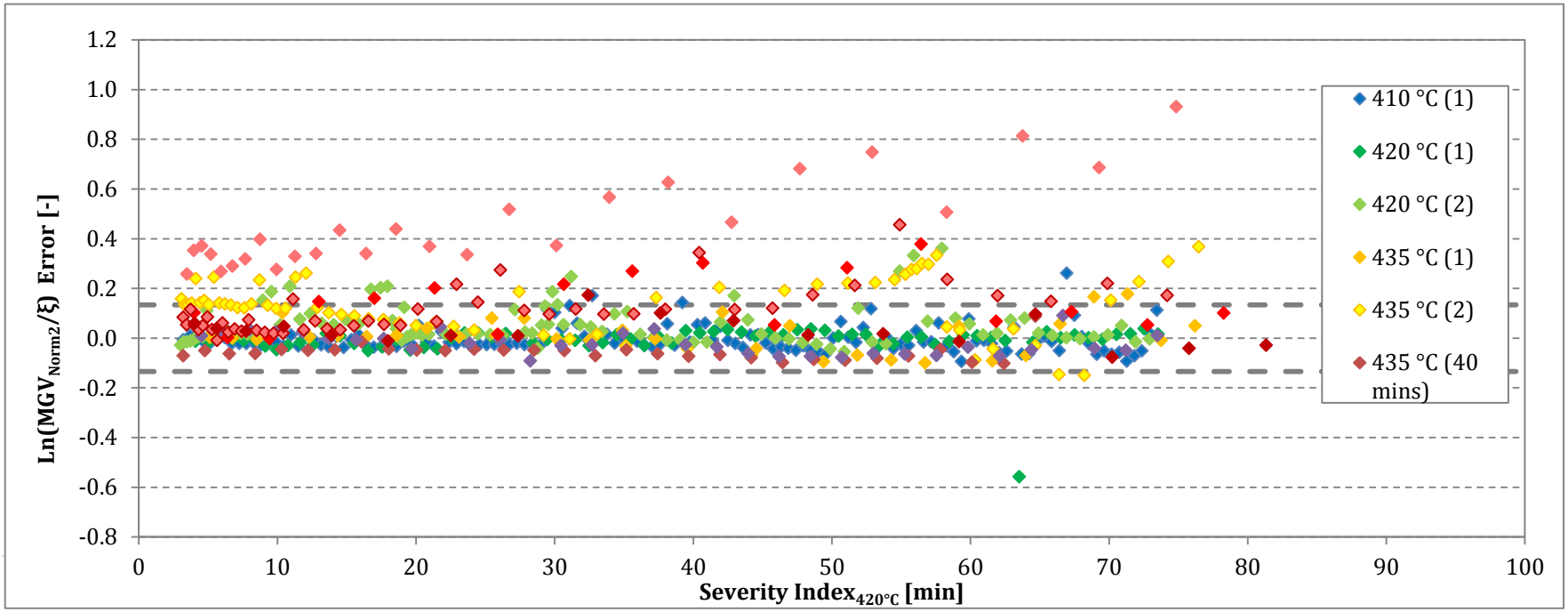

Figure 4.56: Resulting residuals from method one of analysis of Athabasca vacuum residue

Table 4.10: Important parameters from analysis for Athabasca vacuum residue

Parameter	Units	Method 1	Method 2
Activation Energy	[kcal/mol]	52.2	57.6
	[kJ/mol]	218.7	241.18
Slope	[-]	-1.68e-2	-1.64e-2
Y-Intercept	[-]	0.02 ± 0.01	Not Relevant
R^2 Value	[-]	0.88	Not Relevant
Standard Deviation of Slopes	[-]	Not Relevant	2.85e-3
Standard Deviation of Data	[-]	±0.13	Not Relevant

Section 4.2.2.3 Results of Activation Energy Analysis

A summary table of all six feeds after both methods of analysis were conducted is given below in Table 4.12.

Table 4.11: Optimized results for the determination of activation energy

Sample	Method 1 Collapsing Linear Regression					Method 2 Matching Slopes		
	Ea [kcal/mol]	Ea [kJ/mol]	R^2 Value	Slope	Y-Inter	Ea [kcal/mol]	Ea [kJ/mol]	Slope
Cold Lake Bitumen	63.3	267.4	0.94	-1.12e-2	-0.05	53.1	222.1	-1.35e-2
Safaniya VR	42.7	178.8	0.75	-1.16e-2	0.11	58.9	283.5	-1.28e-2
Columbian VR	28.0	117.1	0.82	-9.19e-3	0.07	54.7	228.8	-1.19e-2
Cerro Negro Crude	63.5	265.8	0.96	-1.66e-2	0.02	60.2	252.1	-1.71e-2
Gudao VR	62.4	261.2	0.83	-7.07e-3	0.02	70.0	293.2	-7.26e-3
Athabasca VR	52.2	218.7	0.88	-1.68e-2	0.02	57.6	241.2	-1.64e-2

The use of method one yielded several plots (Figures 4.28, 4.34, 4.41, 4.45, 4.51 and 4.55), that collapse several different temperature data sets into a single linearly regressed line, with R-squared values ranging from 0.75 to 0.96. The R-squared value alone, however, is not enough to determine if the regressed fit is reasonable. Consequently, residual plots were also used to determine the effectiveness of the two methods.

The regression of Cold Lake bitumen data yielded a R-squared value of 0.94, a result that is relatively higher than other R-squared values determined for the other feeds.

Upon inspection of the residual plot Figure 4.31, it can clearly be seen that the error is not random in the case of the 410 °C data. At lower severity there is a tendency for the regression to under predict MGV, while at later times the regression over-predicts the MGV. This bias is indicative of a poor fit even if the R-squared value is relatively high. There is a possibility that temperature effects are still prevalent at lower times as the system has not quite reached the desired reaction temperature. Consequently, the increasing temperature of the reacting medium prevents an establishment of a constant reaction rate. Poor fits at higher severities is likely to be a result of deviations away from a first order regime as previously mentioned and reported in literature. Similar behavior was also observed in the Cerro Negro data and may suggest that cracking behavior may not be accurately captured exactly by first order kinetics. To obtain a better fit, it was recommended that initial portion of the data be truncated later or the later portion of the data is removed as data approaches higher severities.

Further examination of residual plots from method one show a poor model fit to the higher temperature data. Lower temperature experiments are longer in duration and therefore have more data points and the opposite occurs for high temperature experiments that have relatively fewer data point. This mismatch in number of data points leads to a bias towards the lower temperature data sets when using the optimization strategy employed in method one. For this reason, modified method one was conducted to remediate this problem. Results show improved fits for higher temperatures data sets in Figures 4.33, 4.40 and 4.50. The improved fit for higher temperatures comes at a cost of a slightly poorer fit for the lower temperature data.

The use of the second method introduced a separate error factor that accounts for a variety of uncontrolled variables in the experimental apparatus. Results from this method are in agreement with the first method within 15% for the Cerro Negro, Gudao and Athabasca VR. In particular both the Safaniya and Columbian feed had large differences in calculated activation energy. This is likely due to the mismatch in data point bias and normalization error, as the difference reported activation energy is diminished when method two was compared to the modified method one.

In order to evaluate if the use of scattering is the appropriate for the study of cracking kinetics a literature review was conducted. Unfortunately at this time, no other studies outside of this laboratory group were found to use scattering phenomenon to study cracking kinetics. Similar MGV curve trends have been reported by Huang and Otten [78], however, their cracking kinetics study used fluorescence spectroscopy. Fluorescence was found to increase while the oil was heated, but eventually a second stage that followed showed a drop in fluorescence intensity once compounds begin to decompose. Bombardelli *et al*. [79], also found similar trends for the electrical resistivity of oil during cracking reactions. Furthermore, they reported that the change is electrical resistively decreased quicker at higher reaction temperature, a result which is consistent with findings presented in this thesis. Although using different physical phenomena, both studies demonstrate that as the physicochemical properties of an oil mixture changes as it reacts. These studies use these physical phenomena to track the chemical reaction instead of directly measuring concentrations which is traditionally used in kinetic studies. Since this thesis uses backscattering phenomenon to track cracking reactions, readers are cautioned that MGV and DPR are not equivalent to concentration. However, based on the aforementioned studies a conclusion is drawn that the use of to study low conversion cracking kinetics is valid. Calculated activation energies of 117.1-293.2 kJ/mol found in this thesis falls within reported literature values of 99.1-329.7 kJ/mol. More specifically, extensive modeling work by Zarand [80] reports an activation energy range for 217.5-226.6kJ/mol for Athabasca VR. The activation energy of 218.7 kJ/mol calculated by method one in this thesis is within Zarand's reported range.

It should be noted that MGV has its limitations in this study. Since the MGV is the average of the RGB values, it reflects the average brightness. The MGV condenses all the possible information of the micrographs into a single value. It does not reveal any information about the number of mesophase domains or their size distributions. Furthermore, it does not explicitly show when the appearance of mesophase

domains or patchy dark films occur. Thus the primitive approach is not likely able to fully capture the complex behavior of cracking.

Section 4.2.3 Monitoring Reaction Dynamics Using Laser Light Backscattering

Similar cracking experiments were completed on the laser backscattering setup using Athabasca vacuum residue at 420, 435 and 450 °C. The laser experimental setup monitors the reaction by measuring the backscattering of linearly polarized green light at 532 nm. The backscattered light is passed through a probe that partitions the light into its parallel and perpendicular components. The parallel and perpendicular intensities are similar to the MGV of micrographs that use the bright field and polarized settings respectively. One advantage of using the laser backscattering setup is that both intensities are reported simultaneously. An example of the backscattered intensities of the parallel and perpendicular components is shown in Figure 4.58.

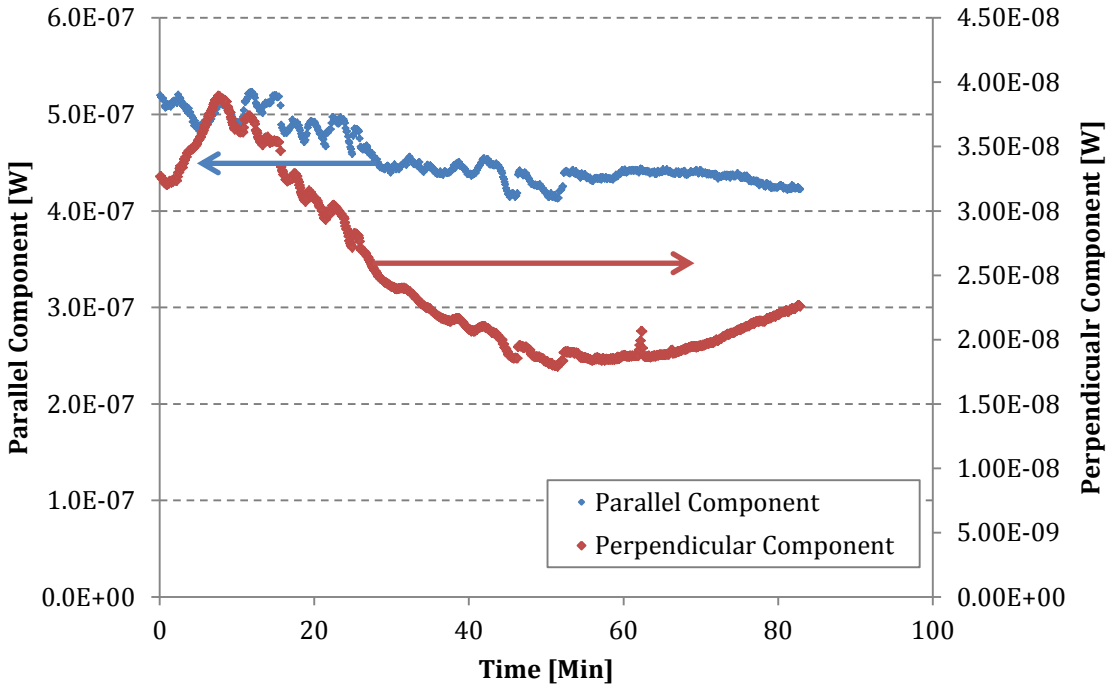

Figure 4.58: Parallel and perpendicular intensities of Athabasca VR reacting at 435 °C

Previous work on the microscope [37] has shown that the intensity of the perpendicular component is closely related to the scattering properties of the reacting medium while the parallel component remains relatively constant. This

phenomenon is also observed in Figure 4.58. Unfortunately, backscattered intensities in Figure 4.58 exhibit a fair amount of relatively small fluctuations that are attributed to a slightly unstable power source that affects the intensity of the incident light source. The depolarization ratio (DPR) is used to factor out these fluctuations. The DPR is defined as the quotient of the intensity of the perpendicular and parallel component. The corresponding DPR of the parallel and perpendicular intensities presented in Figure 4.58 yields a much smoother curve as show depicted in Figure 4.59.

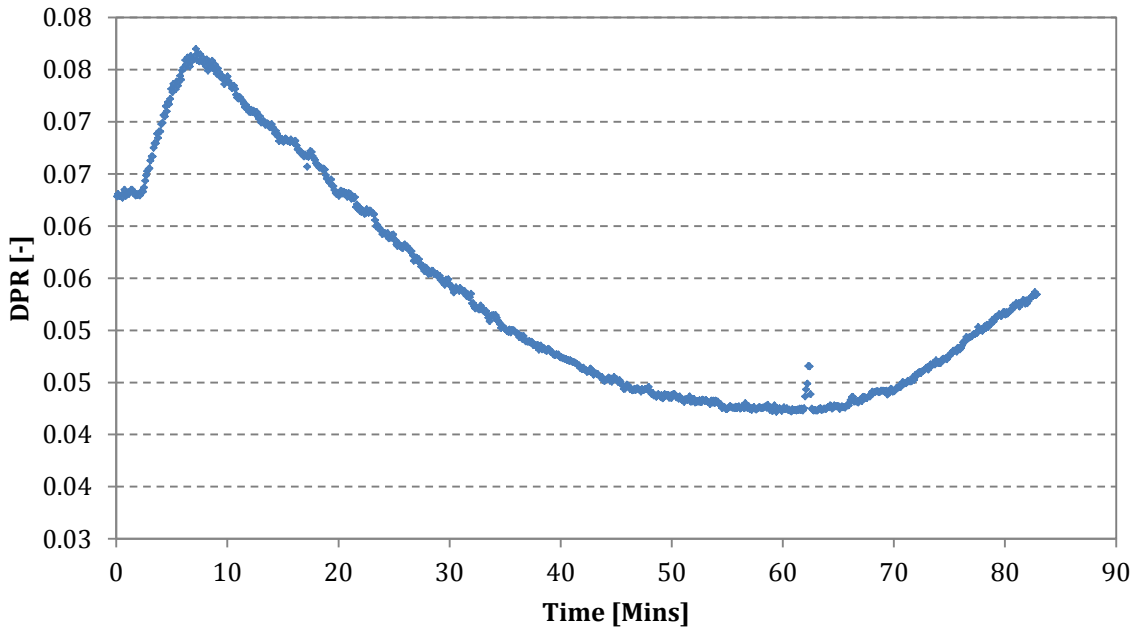

Figure 4.59: The depolarization ratio of Athabasca VR at 435°C

Although the perpendicular intensity is analogous to the MGV data, obtained from image analysis, and can be used directly for analysis, an added level of difficulty is encountered when analyzing data that is plagued with fluctuations. Consequently, the DPR is used instead for all subsequent analysis. DPR trends at various temperatures are given in Figure 4.60.

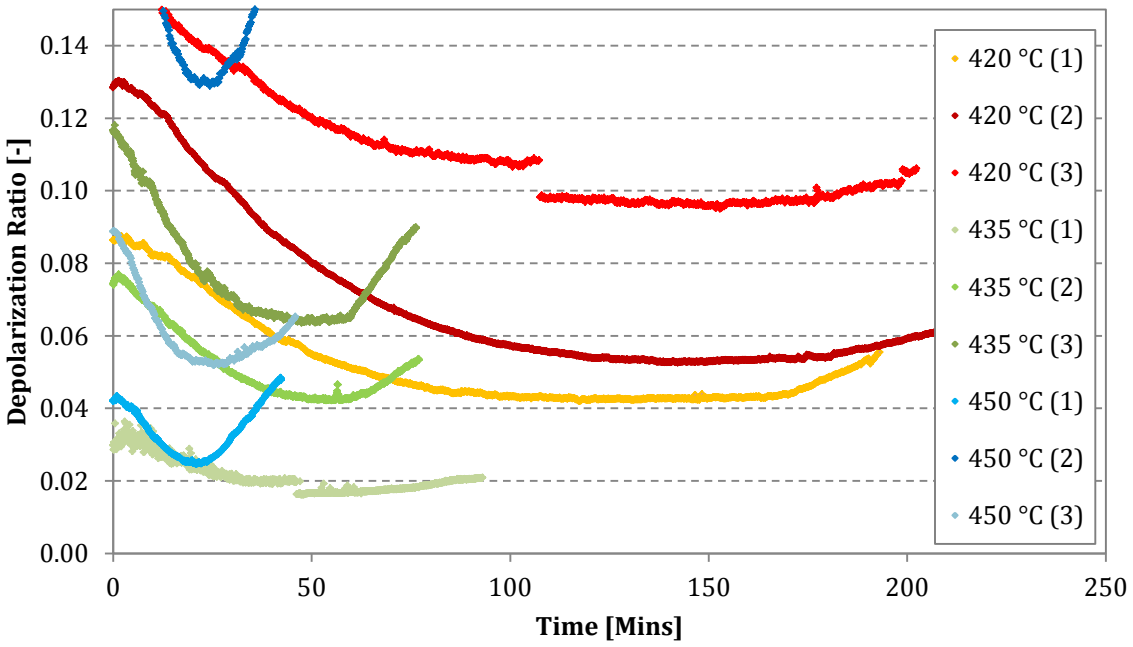

Figure 4.60: Evolution of depolarization ratio of Athabasca VR at various temperatures

In the most general of terms, the DPR curves have similar shapes when compared to MGV curves. One is cautioned against direct comparison of MGV with DPR data as the underlying phenomena that define the parameters are quite different. A compilation of the raw DPR data in Figure 4.60 also illustrates that the DPR decreases and eventually reach a minimum. Figure 4.60 also shows that experiments conducted at lower temperatures require a longer period before the curve begins to level out. This is a result of slower reactions rates at lower temperatures, which was also observed in the MGV data. It should also be noted that there is a discontinuity for the 420 °C (3) and the 435 °C (1) trials in Figure 4.60. Both of these experiments dealt with a disruption which caused a slight shift in the probe mid experiment. The resulting discontinuity is due to the sensitivity of the optic equipment. The discontinuity will not affect subsequent analysis as only the low severity sections of the curves are used. The same MGV normalization procedure in Section 4.2.1.2 was repeated for DPR resulting in Figure 4.61.

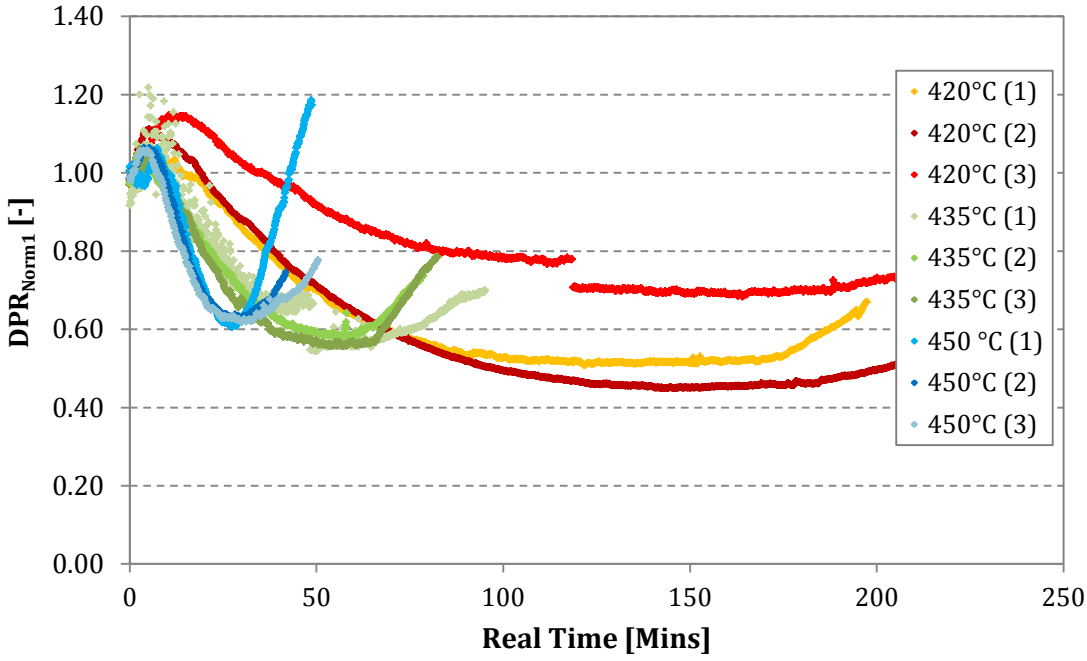

Figure 4.61: Normalized depolarization ratios of Athabasca VR at various temperatures

Section 4.2.3.1 Depolarization Ratio Order Determination

The determination of reaction order for the normalized DPR data follows the same methodology as outlined in Section 4.2.1.3 for the MGV data, with results given in Figures 4.62, 4.63, 4.64 and 4.65, and Table 4.12. Similarly to the MGV data, the heating portion (stage one) and the heterogeneous reaction regime (stage three) were truncated from the analysis. Based on a combination of R-squared values and inspection of residuals, it was concluded that the DPR kinetics were best described second order kinetics.

Table 4.12: Results from DPR fitting to various orders

Order	Slope	R^2	Error
Zero Order	-1.63e-3	0.94	0.64
0.5 Order	-5.30e-3	0.96	0.56
First Order	-1.73e-2	0.98	0.48
1.5 Order	-5.71e-2	0.99	0.42
Second Order	-1.89e-1	0.99	0.38
Third Order	-2.10e0	0.98	0.35

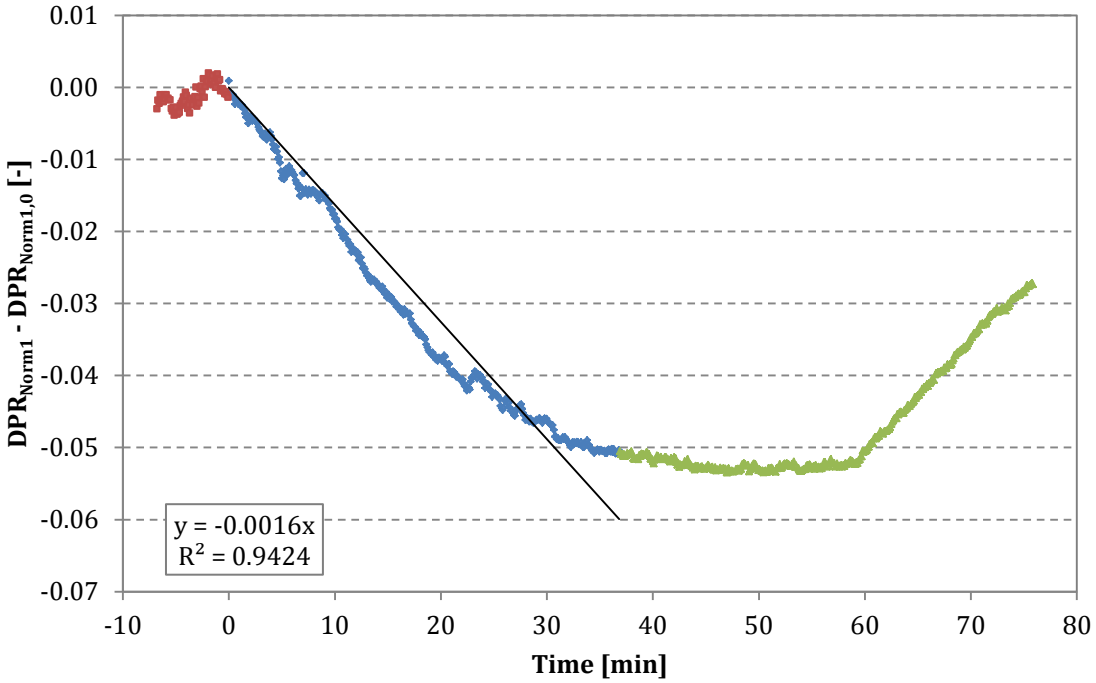

Figure 4.62: DPR data of Athabasca VR at 435 °C fitted to the zeroth order

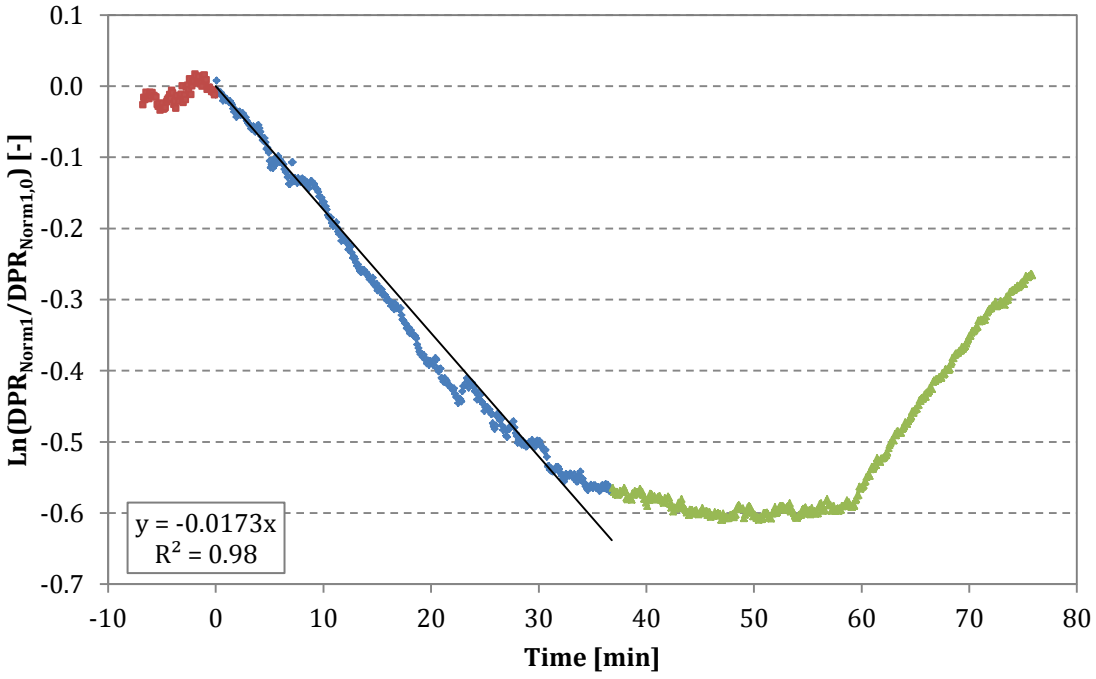

Figure 4.63: DPR data of Athabasca VR at 435 °C fitted to the first order

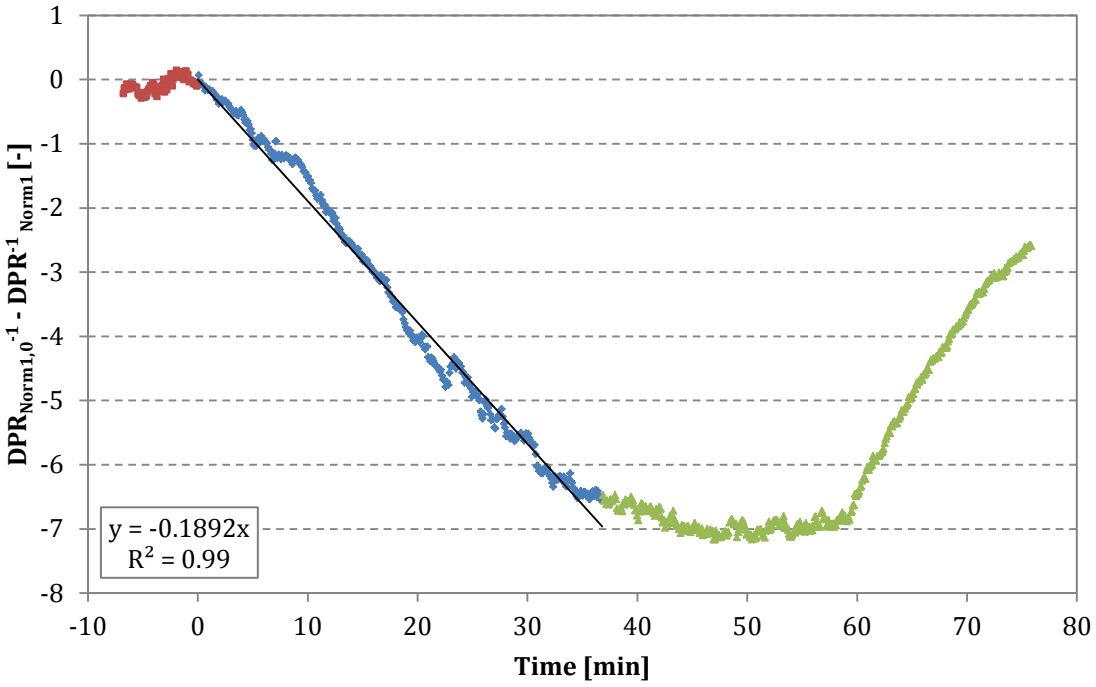

Figure 4.64: DPR data of Athabasca VR at 435 °C fitted to the second order

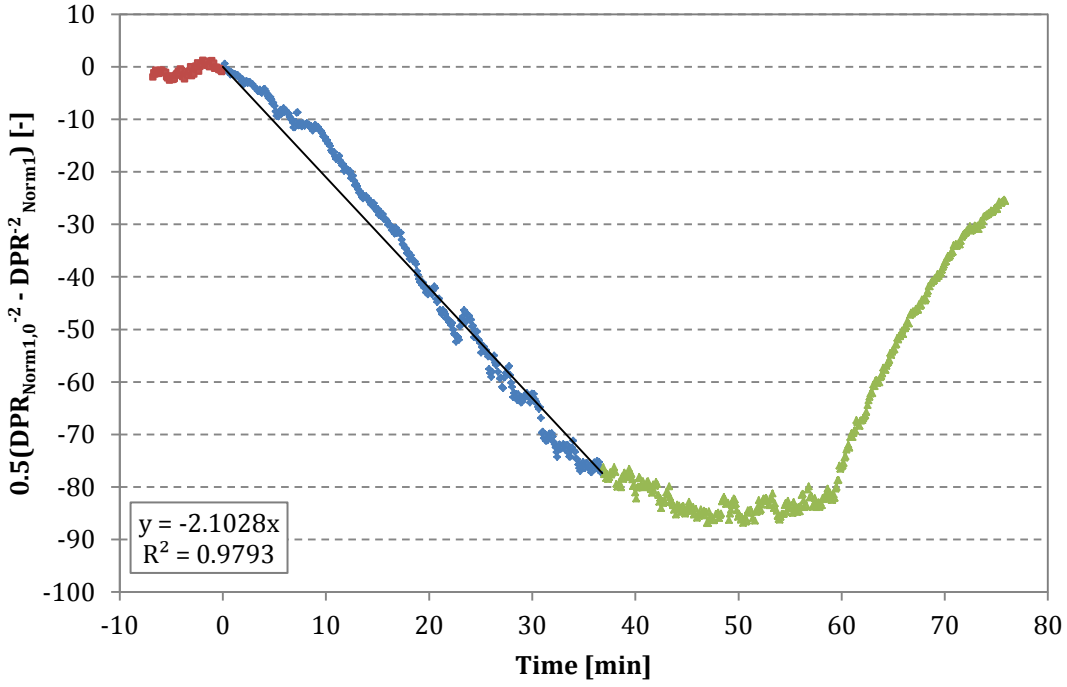

Figure 4.65: DPR data of Athabasca VR at 435 °C fitted to the third order

SECTION 4.2.3.2 DETERMINATION OF ACTIVATION ENERGY USING DEPOLARIZATION RATIO

The analysis of the depolarization ratio once again employs the use of the severity index using 420°C as the reference temperature. The heating portion and heterogeneous reaction stages were removed prior to analysis. Since isothermal data was used, the normalization applied in this section did not account for temperature effects. Similar to method one used in the MGV data analysis, regression of multiple temperature DPR data sets employed the following equation:

$$1 - \frac{1}{DPR_{Norm1}} = k_{ref} \sum_{n=i}^{N} e^{\left[\left(\frac{-E_a}{R}\right)\left(\frac{1}{T_{ave(t)_i}} - \frac{1}{T_R}\right)\right]} \Delta t + \xi \; (Eq. 4.28)$$

The activation energy in Equation 4.28 was varied until the following equation was minimized:

$$objective\ function = abs\left(\frac{1}{DPR_{i,predicted}} - \frac{1}{DPR_{i,experimental}}\right) (Eq. 4.29)$$

The optimal activation energy to fit the second order DPR kinetic model was 218.9 kJ/mol. The optimization yielded a slope of -1.02e-2 with an y-intercept of 0.0835 and a R-squared value of 0.77. Plots of the regression and the residuals are provided in Figures 4.66 and 4.67.

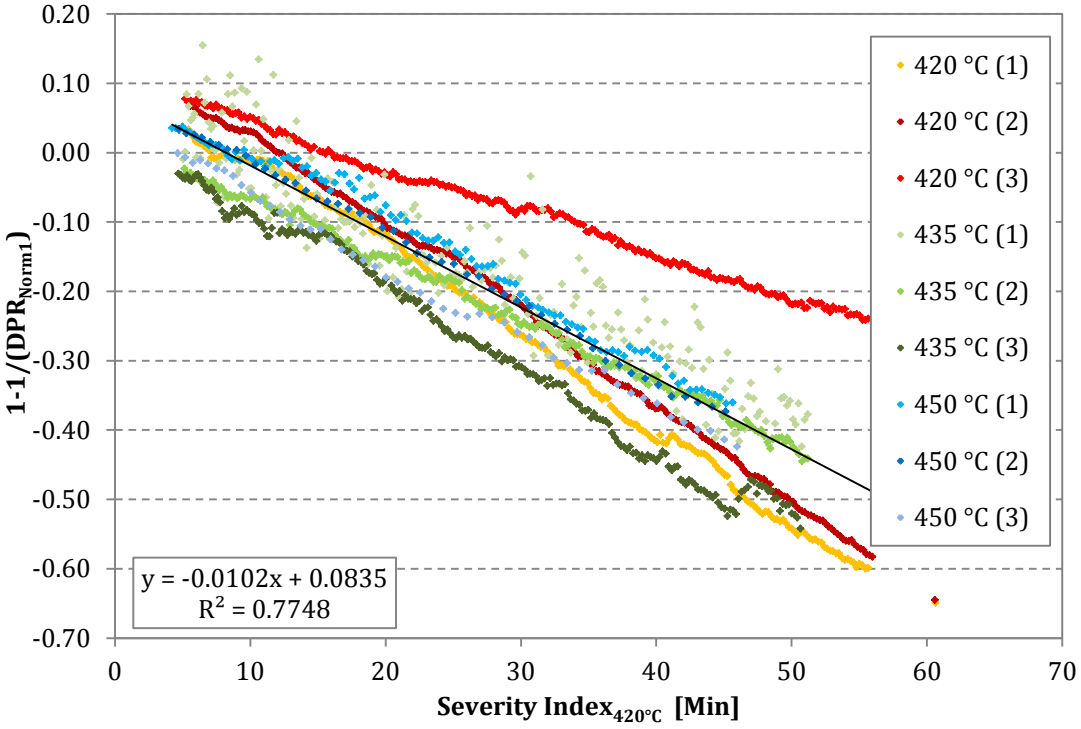

Figure 4.66: Determination of activation energy of Athabasca VR using method one on DPR

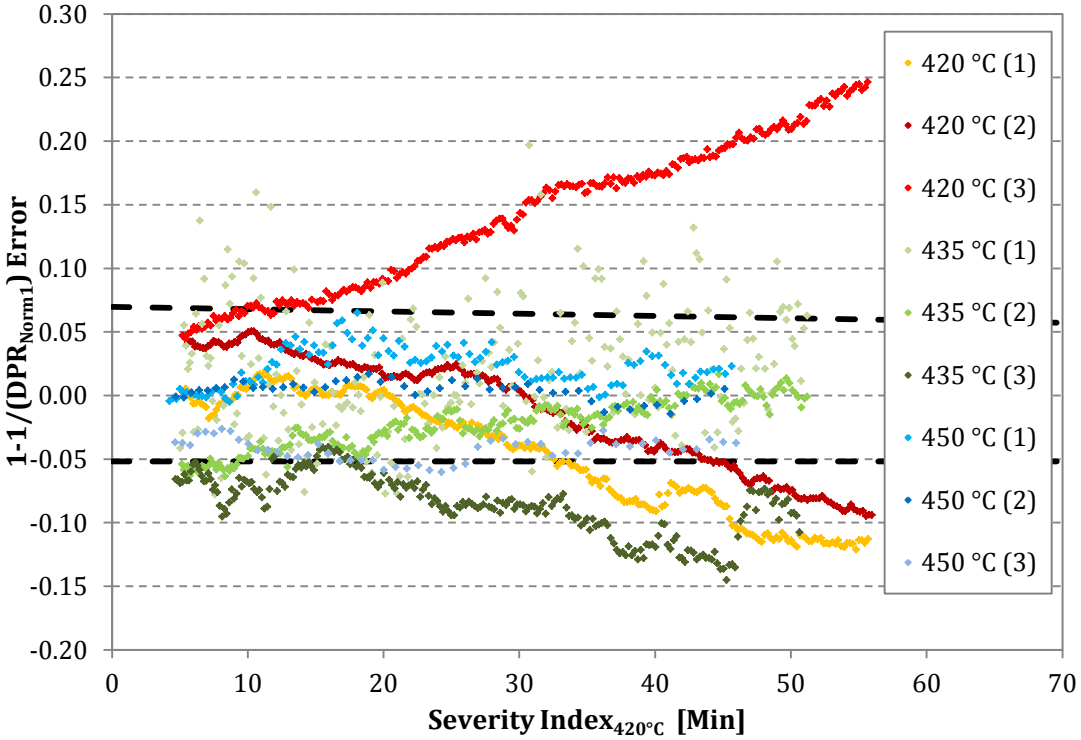

Figure 4.67: Residual plot from using method one on the DPR of Athabasca VR

Examination of Figure 4.67 shows that most data is fitted reasonably well, with the exception of the third triplicate of the trial conducted at 420°C. The slope matching method was also utilized by applying Equation 4.30 to the DPR data and then optimized by minimizing the variance of the slopes of each individual data set as shown by Equation 4.31.

$$1 - \frac{1}{(DPR)_i} = k_{ref,i} \sum_{n=i}^{N} e^{\left[\left(\frac{-E_a}{R}\right)\left(\frac{1}{T_{ave(t)_i}} - \frac{1}{T_R}\right)\right]} \Delta t + \xi_i \; (Eq. 4.30)$$

$$Objective\ Func.\ M2 = \sigma_{k_{ref,i}} \; (Eq. 4.31)$$

Again, Equation 4.30 was modified for the DPR as it was established that DPR power law kinetics is second order. Results from the application of method two are given in Figure 4.68 with residuals in Figure 4.69. An activation energy of 271.6 kJ/mol or 64.9 kcal/mol was calculated.

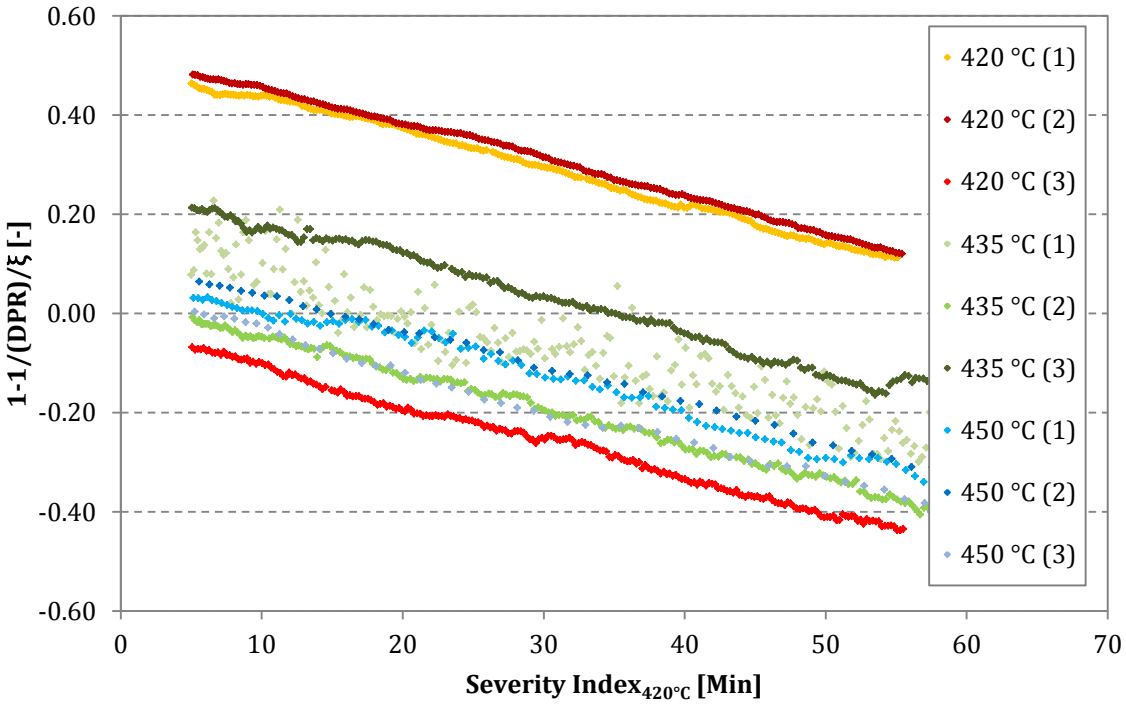

Figure 4.68: Determination of activation energy of Athabasca VR using method two on DPR

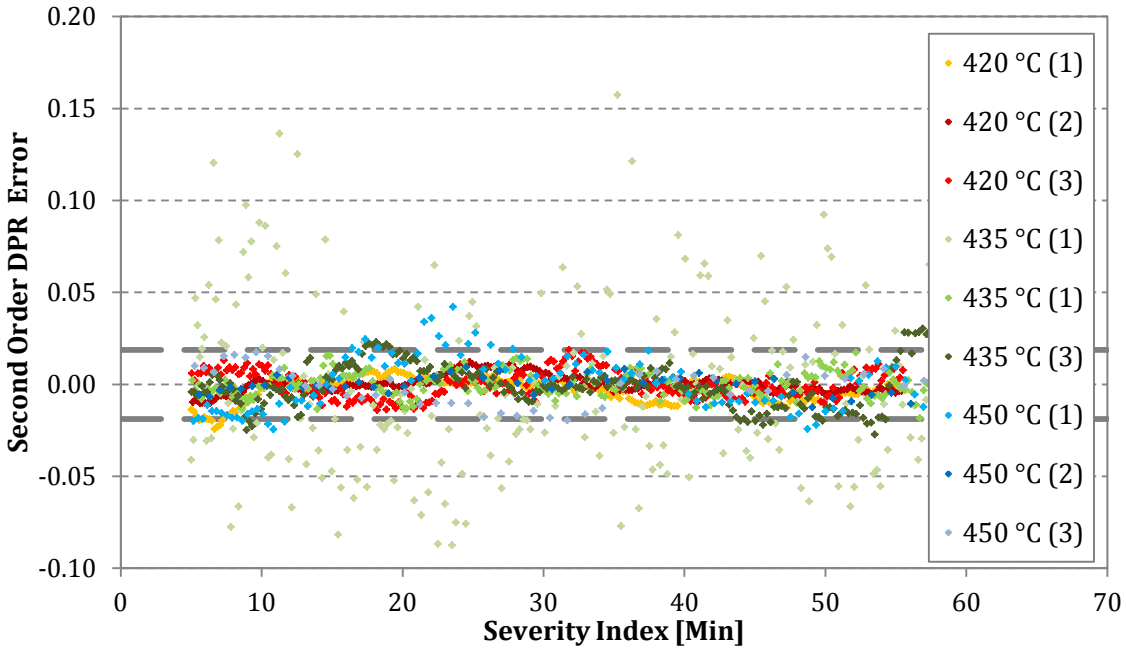

Figure 4.69: Residual plot from using method two on the DPR of Athabasca VR

Comparison of the residual plots shows that method two provides a more robust methodology of analysis. Currently there is no explanation as to why DPR kinetics falls under second order kinetics while MGV kinetics is better captured by first order. Thus, the activation energies determined from the polarized microscopy data and the laser backscattering data are not comparable.

Use of depolarization ratio to study kinetics has been reported by Pujala and Bohidar [81]. This particular study investigated the kinetics during a heterogeneous reaction however, and reported that the kinetics of laponite dispersions at water-air interfaces follows power law kinetics with a wide range of orders from 0.1 to 4. Although the DPR is commonly used to study kinetics of systems that feature anisotropic material, it seems that this work is the first to use this technique to study kinetics of systems before the onset of anisotropic material.

One concern that should be mentioned is the possibility of fluorescence interfering with the intensity of the back scattering when using the green laser with vacuum residues. It is known that this phenomenon is enhanced when shorter wavelengths in the blue to UV region are used. This system uses green light in hopes of reducing

this complication. An additional concern is the truncation of the data. In the previous sections, MGV data that operated in the heterogeneous fouling reaction stage was removed prior to analysis. The onset time for the laser backscattering system, is ambiguous as this experimental system does not provide micrographs for optical detection.

Section 4.3 Onset Times

Onset times have been determined from microscopy experiments through direct examination of the micrographs. As mentioned in Section 4.2.1, two different types of fouling behaviors were observed. Onset times for both mesophase and dark films were determined for the Gudao and Columbian feeds where dark film fouling was observed. Pictures were inspected and the time at which the appearance was seen was recorded. Times presented below include the heating portion of the experiments, but were all corrected by one to three minutes as to remove the initial portion of the heating ramp that exhibited a temperature lag when the setpoint was initially changed to reaction temperature. Results presented include a 95% confidence interval only if more than one trial was conducted for that particular set of experimental conditions and are given in Figure 4.70 to 4.72.

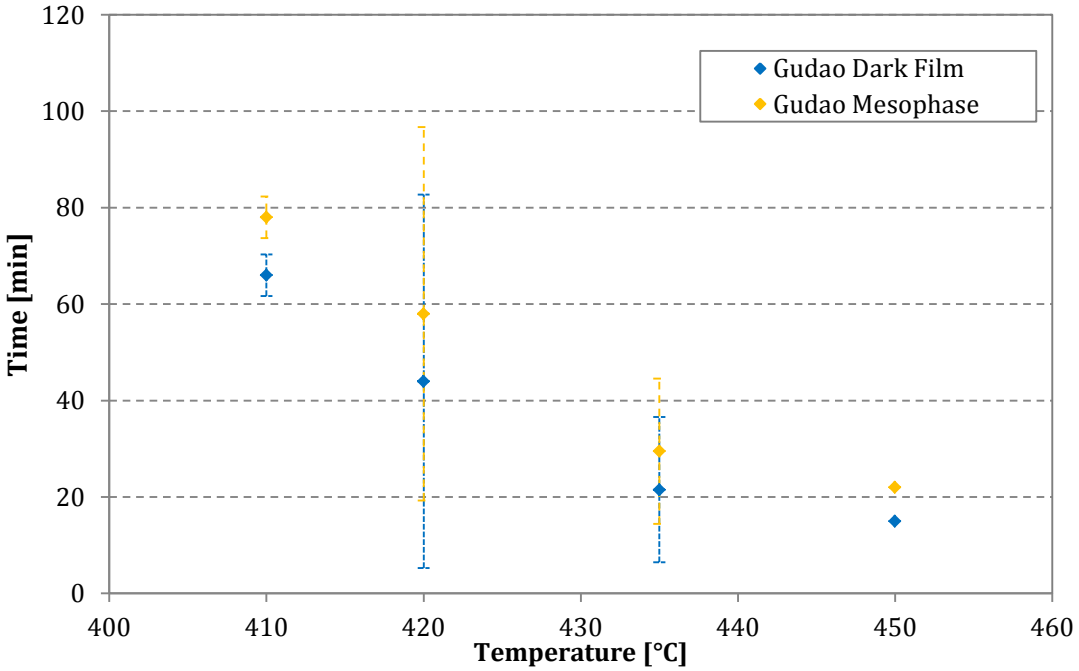

Figure 4.70: Heterogeneous onset times for Gudao as a function of temperature

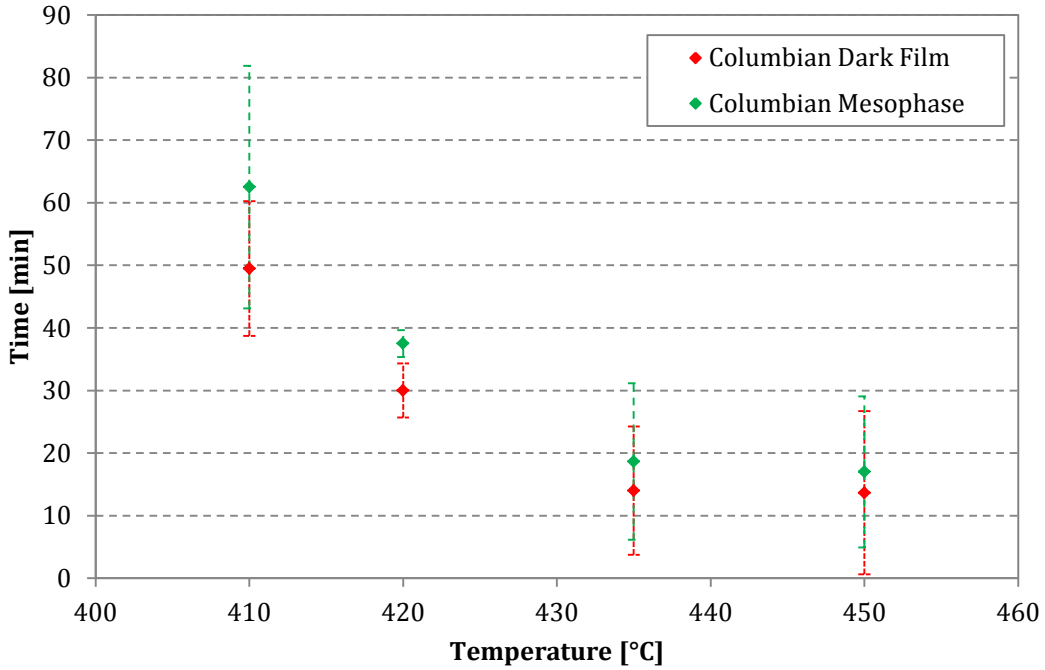

Figure 4.71: Heterogeneous onset times for Columbian as a Function of temperature

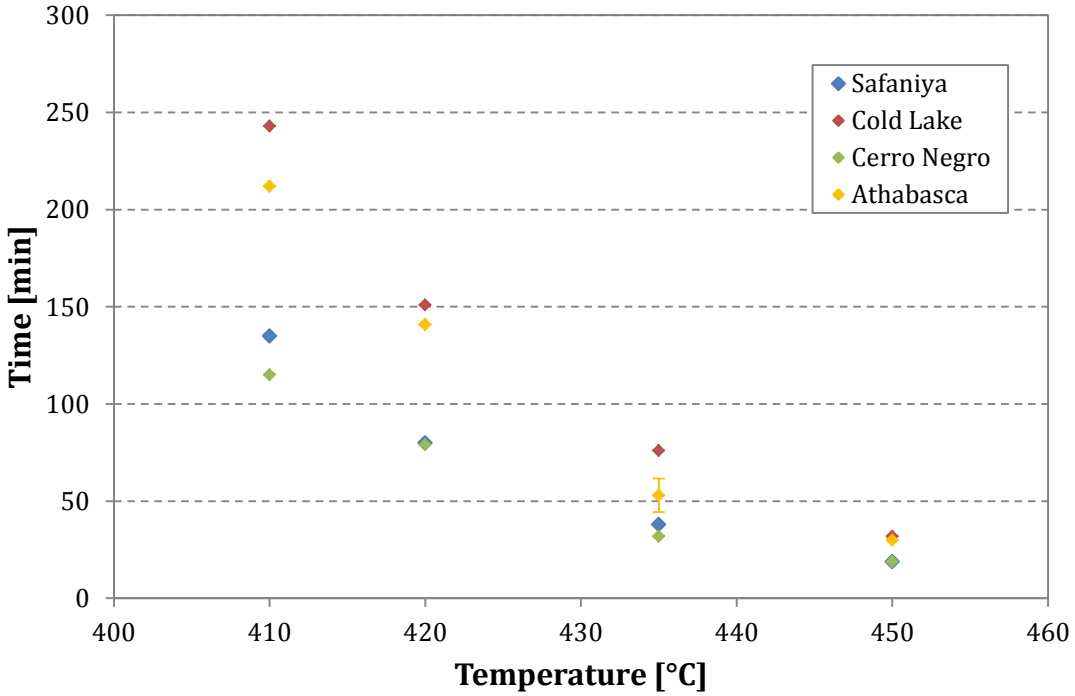

Figure 4.72: Mesophase onset times for feeds that do not exhibit dark film fouling

As expected, results from all experiments indicate that onset times drop with increasing temperature. From Figure 4.72 it can be seen that the drop in onset times is not significant between 435 and 450°C. A possible explanation for this observation is that experiments at 450°C spend a significant portion of time on the heating ramp.

Guado and Columbian results in Figures 4.70 and 4.71 both have large confidence intervals. Since data reported in Figures 4.70 and 4.71 mostly represent duplicates, the large intervals are likely to be a result of running statistics on data sets with minimal replicates. Variability in these duplicates and triplicates may also indicate that onset periods for dark film fouling feeds are susceptible to experimental factors such as reactor hydrodynamics and or nucleation sites. As stated in Chapter 3, stirring is accomplished using a magnetic stirrer that rotates based on an external magnet operating at 120 rpm. The current stirring mechanism provides only minimal agitation. Accordingly, the mixing is also not in the turbulent regime resulting in the possibility of inconsistent mixing. Nucleation sites can also be produced from wall effects in or from cross contamination due to improper cleaning even with current stringent cleaning procedures. It is recommended that additional replicates be completed after these factors are improved.

SECTION 4.4 THEORETICAL VALIDATION OF EXPERIMENTAL SETUP FOR SUBCRITICAL AQUATHEMRAL STUDY

For the purposes of this study, subcritical aquathermal conditions are defined as elevated temperature and pressure in a system that contains water, but is not so high that it becomes a supercritical fluid. Although the term hydrothermal has been used before to describe systems with water, this study chooses to use aqua to avoid confusion as hydro is commonly referred to in refining as the use of hydrogen. The creation of an experimental setup that is able to operate at these conditions has proven to be challenging for a number of reasons. The issues primarily stemmed from the severe operating conditions. One factor is that the materials of construction needed to be configured properly. While the Swagelok parts are designed to withstand the experimental temperatures and pressures, special care was necessary for the design of the sapphire window. As sapphire is the most brittle component it is most likely to fail in the event of an over pressurization. A rupture assembly was also installed for extra precaution. Other problems were also encountered and will be explored further in the following sections.

SECTION 4.4.1 TEMPERATURE VALIDATION

Since water has tendency to condense, extra care must be given to uniform temperature of the reactor surfaces. It is determined that all surfaces should be above 370 °C to prevent condensation and simulations were completed to explore this issue.

The temperatures of the reactor system and all the Swagelok parts were modeled using COMSOL, finite element software. The reactor was modeled using the conjugate heat transfer package in the software which was built specifically for convective heat transfer. COMSOL is able to calculate the temperature profile of the reactor once the user has specified the dimensions, the material makeup and the boundary conditions. Reactor dimensions were captured through the use of several ANSI Steel tubes with varying diameters and wall thicknesses. The entire system was pressurized with nitrogen. Three types of boundary conditions were applied, the first shown in Figure 4.73A are the surfaces defined by the convective heat

losses. The second boundary condition applied was a constant temperature condition. This case was applied across two different areas as shown in Figure 4.73B-C. The surface area in Figure 4.73B is where the first band heater heats the main body of the reactor where the sample is set. The other area illustrated in Figure 4.73C is the arm where a second heater operates to keep the rupture disk assembly heated. The final boundary condition is dedicated to the solid-fluid boundary inside the tubes and is depicted in Figure 4.73D.

The base simulation case was designed to maintain the heated surfaces in Figure 4.74 B and C at 435 °C while applying a convective heat transfer coefficient of 10 W/(m^{2}K) for non-heated Figure 4.74 A surfaces. It is assumed that room temperature was at 20 °C and the inside the reactor was filled with nitrogen at atmospheric pressure. This resulting profile is given in Figure 4.74 A. Typical heat transfer coefficients between gas-steel-gas range from 5 to 10 W/(m^{2}K). Sensitivity analyses were conducted to examine both the effect of convection coefficient and effect of wall temperature on the temperature profile of the reactor. First the convective coefficient was changed to 5 and 20 W/(m^{2}K) while the temperature constant heated surfaces were kept at 435 °C. As expected, the higher convective coefficient resulted in greater heat losses as shown in Figure 4.74 C and the opposite was shown for the smaller coefficient as illustrated in Figure 4.74 B. Additionally, profiles were also determined for constant temperature surfaces were kept at 420, 435 and 450 °C and are shown in Figures 4.74 D, A and E respectively. Simulation results indicate that in all cases, all of the wall temperature are maintained above 370 °C and condensation of water should be avoided.

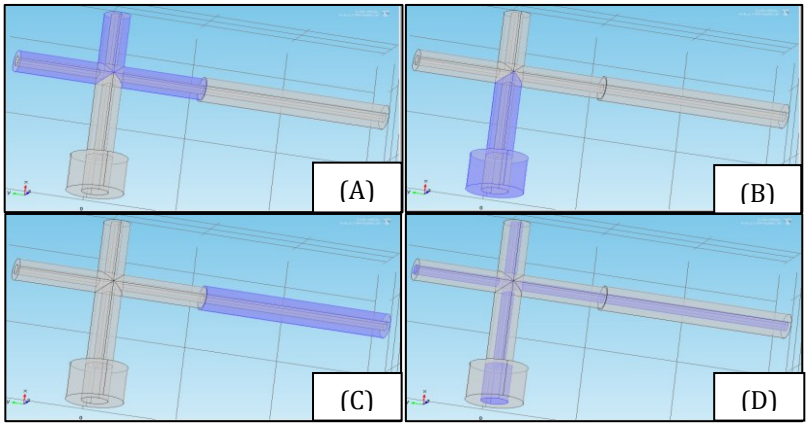

Figure 4.73: Various boundary conditions used in COMSOL simulations

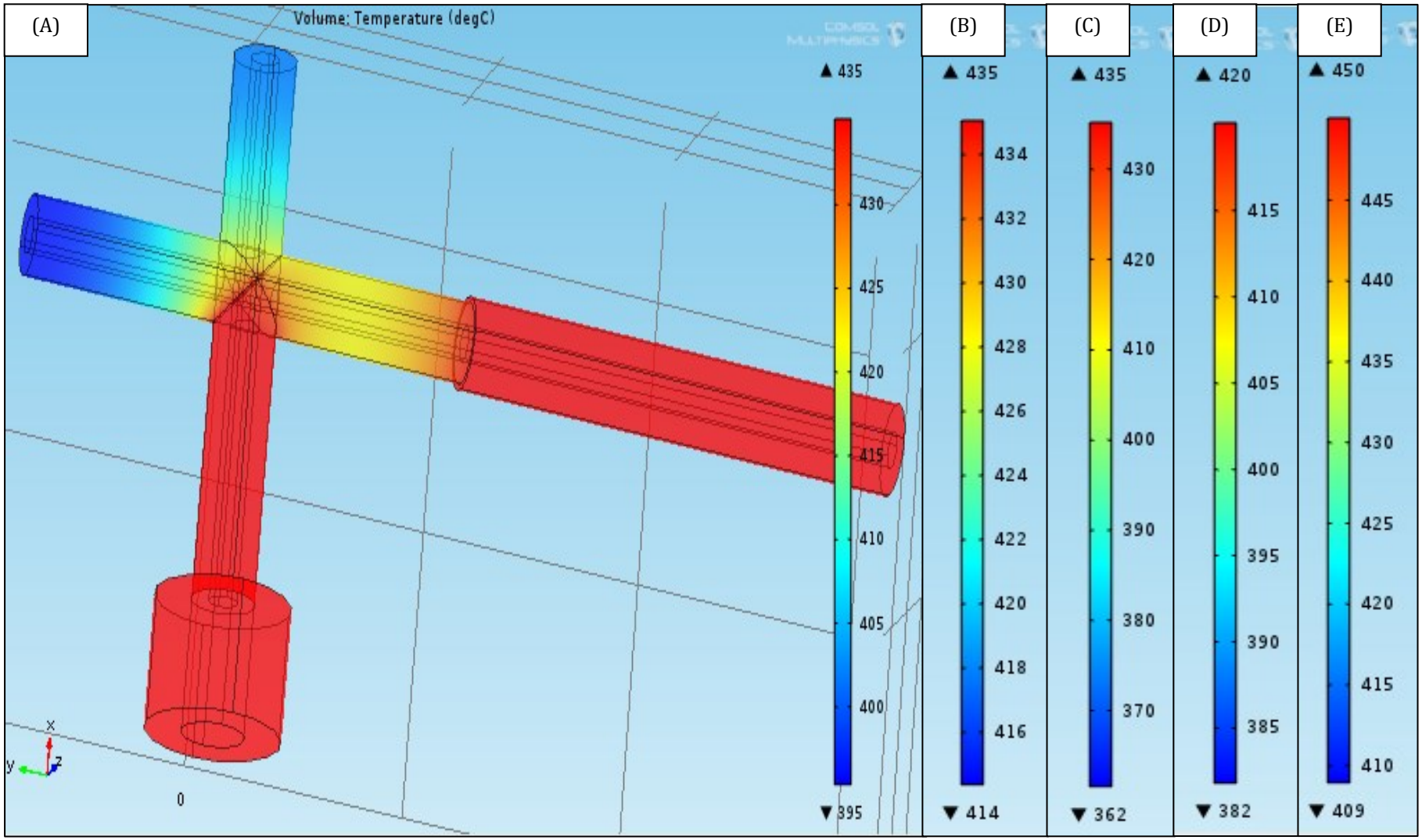

Figure 4.74: COMSOL temperature profiles with heated surface temperatures and convective coefficients of: (A) T = 435 °C & H= 10 W/(m²K) (B) T = 435 °C & H= 5 W/(m²K) (C) T = 435 °C & H = 20 W/(m²K) (D) T = 420 °C & H = 10 W/(m²K) (E) T = 450 °C & H= 10 W/(m²K)

SECTION 4.4.2 PRESSURE VALIDATION

While the aquathermal conditions used in this study are selected so that the water is at subcritical conditions, the system is still at relatively high temperature and pressure. In order to measure the reactor pressure, both the use of pressure transducers and Bourdon pressure gauges were explored. It was found, however, that they are not suitable for this application. Most pressure transducers required too large of a headspace for the experimental and many were also unable to handle elevated temperatures. The usual approach for extending the usable temperature range for a transducer is the insertion of a segment of pipe in between the transducer and the hot medium, thus acting as a cooler. Unfortunately this approach cannot be used for this setup as the cooling pipe would act as a surface for water condensation and add headspace. Since the amount of water used in the experiments is in the order of 0.1 g for the microreactors, even the smallest amount of condensation, result in large pressure losses. Bourdon pressure gauges also are prone to condensation problems.

Rather than direct pressure measurement, the pressures for the microreactor experiments are estimated computationally through the use of thermodynamic simulation. Values from simulation are experimentally validated using the Parr reactor which has a much larger volume of 500mL and measures pressure using a Bordon pressure gauge attached to the top of the reaction vessel. For a more detailed description of the Parr reactor please refer to Section 3.2. Experimental pressures obtained are expected to be lower than simulated pressures as the Bordon gauge provides a cold sink for condensation, lowering the amount of water in the vapour phase. When compared to the micro reactors however, it is expected Parr reactor pressure is not as severely affected by condensation because a

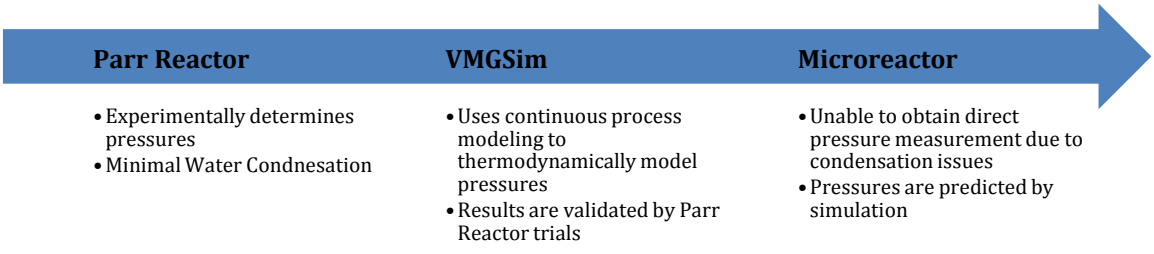

Figure 4.75: Summary of pressure modeling

significantly larger amount of water was used. A summary of pressure validation is given in Figure 4.75.

The process simulation software used was VMGSim. While the current apparatus is a batch process, VMGSim works best when modeling continuous processes. For the purposes of the modeling, the reactor was simulated as a steady-state continuous process to estimate the maximum pressure that could be generated inside the reactor during the operation. The process flow diagram used for the continuous simulation is given in Figure 4.76. The process functions by mixing the desired ratio of water and heavy oil and pumping the mixed stream to achieve desired initial pressure inside the reaction vessel. This pressure is the initial pressure in the reactor before any heating. The controller "CN2" varies the amount of nitrogen that is compressed to ensure that the total volume of the total feed stream "TF" consisting of the oil, water and nitrogen amounts to reactor volume. In the case of the Parr reactor experiments the volume and initial pressure was set to 500mL and 1.5MPa. The reaction pressure was calculated through the use of controller "CN1", which performed an iterative calculation by adjusting the pressure of the heated stream "HF" to ensure that the heating process is isochoric. The use of simulation is not without its limitations, for example, the property package used to conduct thermodynamic calculations was the Advance Peng-Robinson equation of state. Although the Peng-Robinson is able to characterize oils, the addition of water introduces significant error. As such, experiments were conducted in the Parr reactor to verify the results that were simulated. This error did not pose a significant problem with safe reactor operation, however, because the actual pressures were always lower than the simulated pressure. Additionally, since the objective of pressure determination was to ensure operation remained subcritical and within safe operating limits, the error was deemed acceptable.

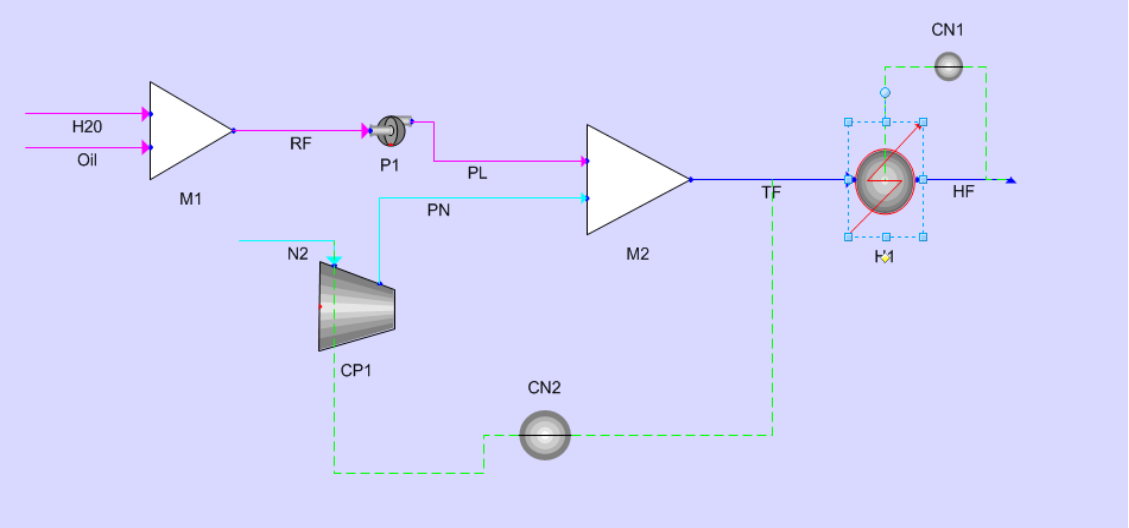

Figure 4.76: Process diagram for pressure calculation using VMGSim

Reactions conducted in the Parr reactor are initially pressurized at 1.5 MPa of nitrogen. Several different experiments were completed, with one trial testing only 40 mL of water with nitrogen. Results of the water and nitrogen experiment are given in Figure 4.61 and show the increase in pressure as the water and nitrogen are heated. Both the wall and center temperature of the reactor were reported. This is done to examine if there were large temperature gradient across the reactor. The largest gradients in the Figure 4.77 and 4.79 are experienced during the initial heating ramp. The reason for this observation is due to the lack of stirring as the impellers are not activated until the reactor has reached at least 150 °C. Temperature differentials of up to 20 °C were observed. Once mixing has been turned on and the reactor has been heated past 350 °C the average differential was determined to be in the order of 5 °C.

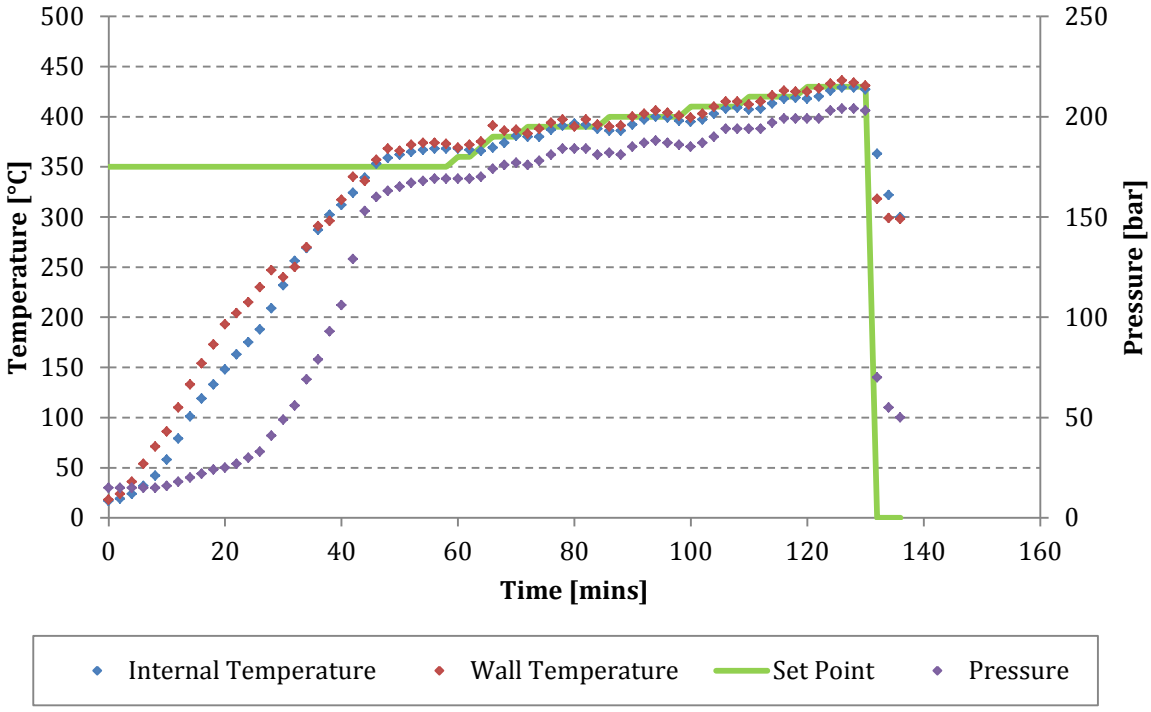

Figure 4.77: Parr reactor run with water + nitrogen (1.5 MPa initially) system

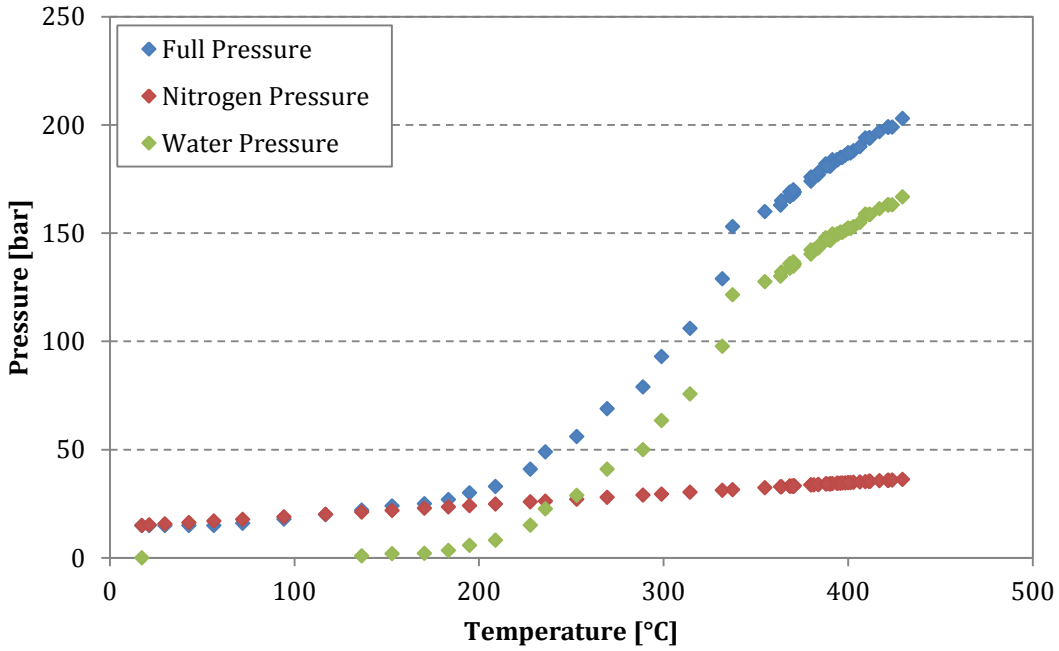

Figure 4.78: Partial pressure as a function of temperature for water + nitrogen system

The blue diamonds in Figure 4.78 show the average temperature and its corresponding pressures from the experiment in Figure 4.77. This total pressure can be crudely fractioned into its partial pressure by using the ideal gas law to determine the nitrogen pressure alone. The partial pressure provided by the nitrogen was subtracted from the full pressure to determine a rough estimate of the water partial pressure. This calculation was completed assuming there were no intermolecular interactions between the water vapor and nitrogen and limited nitrogen solubility in the liquid water phase. A comparison of water partial pressure calculated against saturated steam table values indicate that the experimental values are lower than expected. This might be attributed to the fact that there was some water condensation, as well as the possibility that there were some intramolecular interactions within the water.

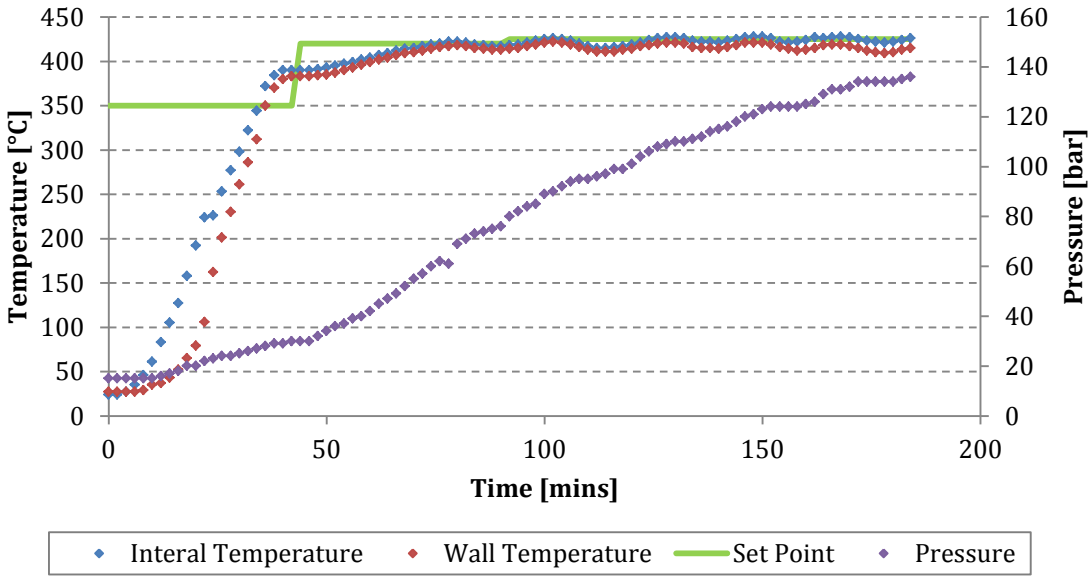

Figure 4.79: Parr reactor run with Athabasca VR + nitrogen (1.5 MPa initially) system

A similar test was conducted in the Parr reactor for a dry system with Athabasca VR shown in Figure 4.79. The vapour pressure of the heavy oil is significantly less than water. This is expected as vacuum residue is composed of heavy components with high boiling points. Upon reaching the final set point of 425 °C, results of the Athabasca VR plus nitrogen experiment show that the pressures continue to increase even after the final temperature setpoint. This is a result of cracking

reactions that occur when temperatures exceed 370 °C producing lighter products, some of which then contributes to the overall pressure. It becomes apparent then that experimental and simulated results should only be compared at pre-cracking temperatures, since the simulation only calculates the thermodynamic equilibrium and does not take into account any reactions.

Several trials were also conducted for a water, oil and nitrogen systems. All tests were initially pressurized with 1.5 MPa of nitrogen and loaded with approximately 170 g of oil. Water concentrations of 4.6, 7.6, 9.1 wt% were tested with results are given in Figure 4.80. Duplicates at each water concentration were tested. Simulation curves predict that the pressure increases in an exponential fashion until a break point after which the pressure increases in linear manner. Although the shape of the experimental curves seems to agree with the simulation results, the point at which the experimental points begin to behave linearly is delayed relative to the simulated curve. In addition, the simulation consistently overpredicts the pressure. As aforementioned, the lower experimental pressure is likely to be the result of some water condensation, as well as interactions between the various chemical species. Additionally, VMG Simulation with the Peng-Robinson property package under predicts the water and nitrogen solubility in the oil phase. Furthermore, the experimental system was not in equilibrium. Results shown are taken during the heating ramp with the presence of a thermal gradient within the reactor. Finally, results show that once temperatures pass 370 °C, the pressures increase more rapidly than the linear trend predicted by VMGSim. This is attributed to cracking reactions that produce vapour products that contribute to an increase in pressure.

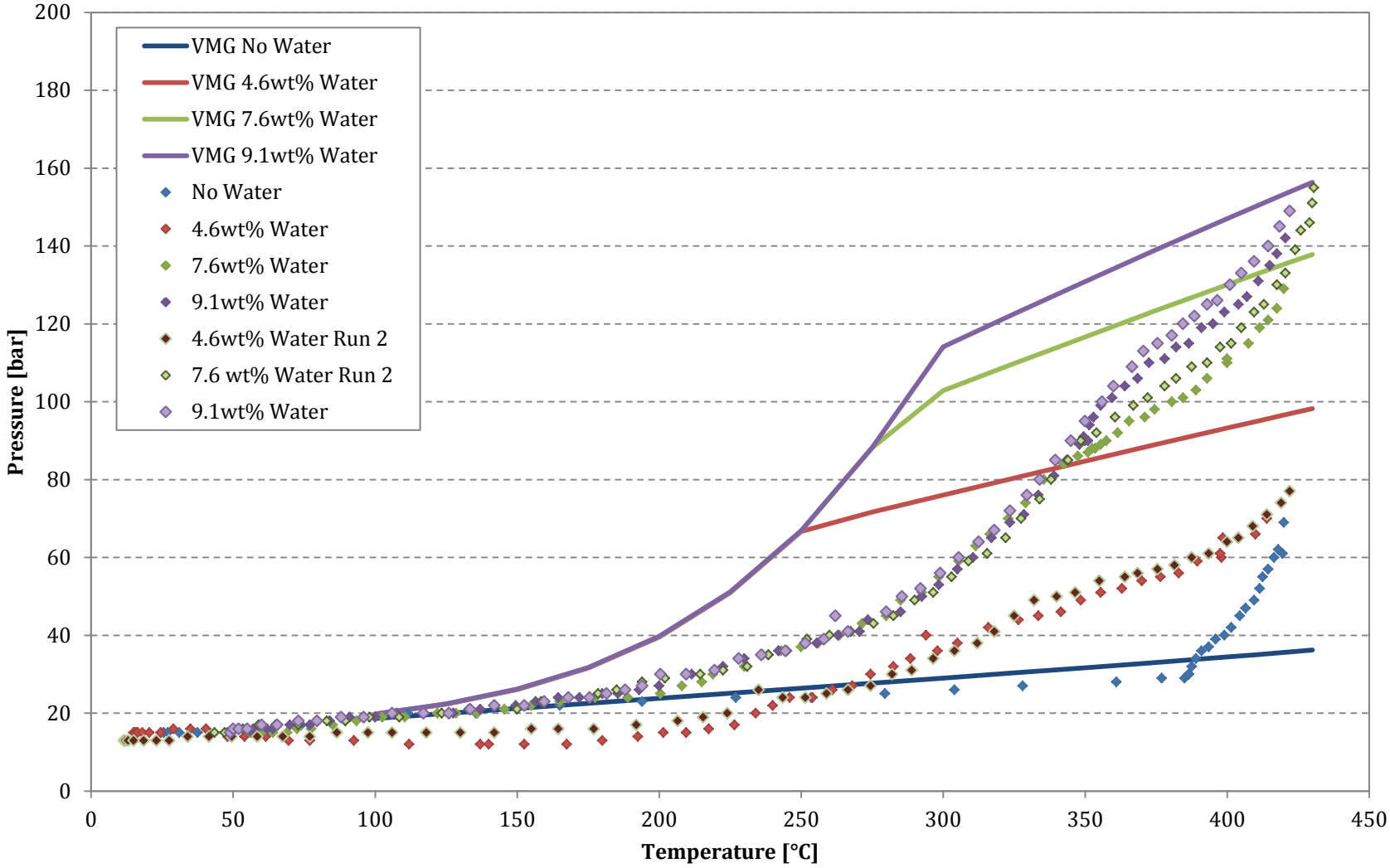

Figure 4.80: Comparison of experimental and simulated pressure profiles for oil + water + nitrogen systems. Simulated results are shown in lines and experimental results are given by points

Section 4.5 Aquathermal Experiments

Section 4.5.1 Aquathermal Experiments with Polarized Microscopy

With the validation of the experimental setup complete, aquathermal runs were conducted with Athabasca VR at 435 °C with 12.5 wt% and 23.9 wt% water on the polarized microscopy setup. The base case contained 12 wt% water and was initially pressurized with 2 MPa of nitrogen and is expected to reach 8.7 MPa at 435 °C before significant reactions. Micrographs from these experiments are shown in Figure 4.81 at five minutes stages. Inspection of micrographs shows that the addition of water introduces the formation of a dark film before the onset of mesophase. This phenomenon was not observed in the experiments without added water. In the case of the results in Figure 4.81, the dark film appearance can be clearly seen at 30 minutes. Replicates of these runs confirm that the addition of water results in phase instability and causes Athabasca VR to exhibit dark film fouling when reacted with water.

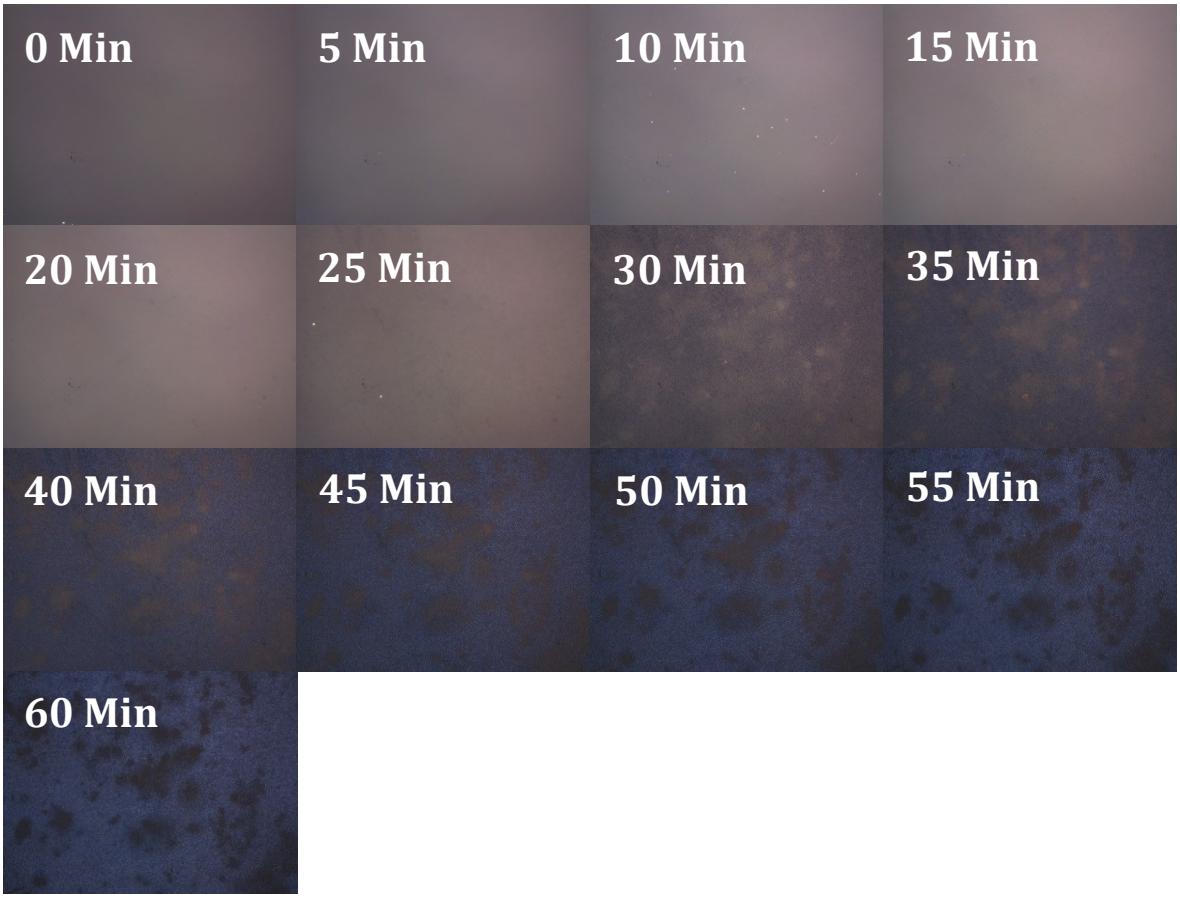

Figure 4.81: Dark film fouling behavior of Athabasca VR at 435 °C and 12.5 wt% water

The phase destabilization as shown in Figure 4.81 is likely to be a result of a physical phenomenon. The dark film that is shown to occur when water is added to Athabasca VR is likely to be the result of fine solids deposition are were previously discuss in Section 4.1 during feed characterization.

The corresponding Normalized MGV plot of the micrographs in Figure 4.81 is given in Figure 4.82.

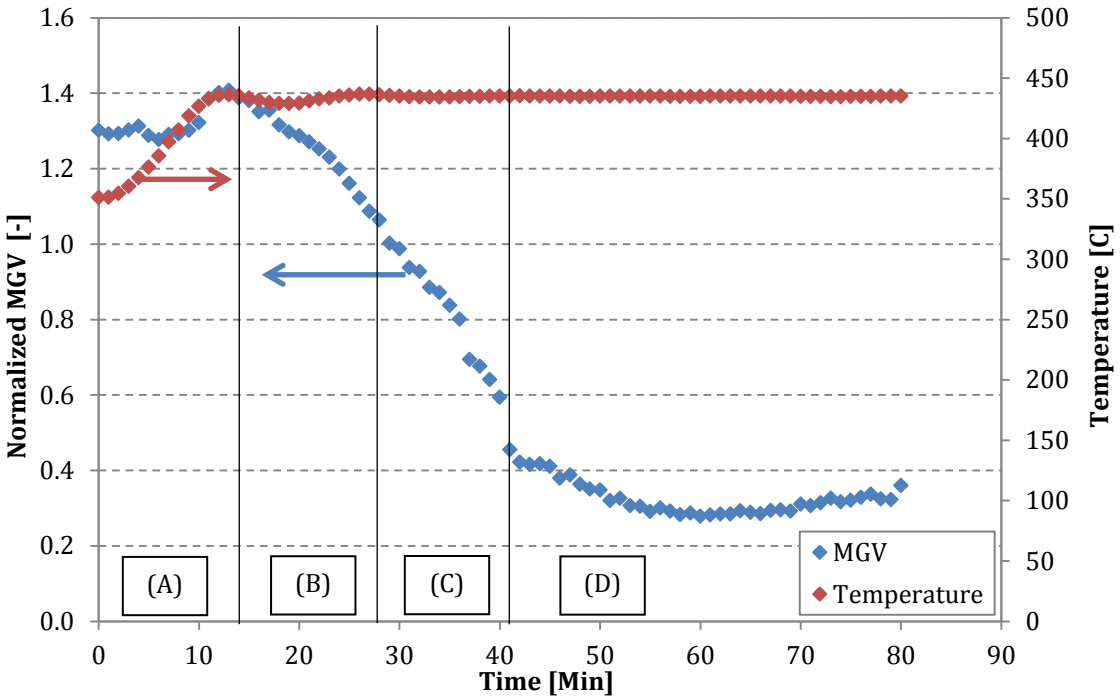

Figure 4.82: Normalized MGV evolution behavior of Athabasca VR at 435 °C and 12.5 wt% water subdivided into (A) Heating Ramp (B) Homogenous Reaction Stage (C) Dark film fouling stage (D) Mesophase fouling stage

Vertical lines are given in Figure 4.82 the various reaction stages are based on optical detection. Figures 4.83 and 4.84 compare experiments in the homogeneous reaction stage for experiments with and without added water.

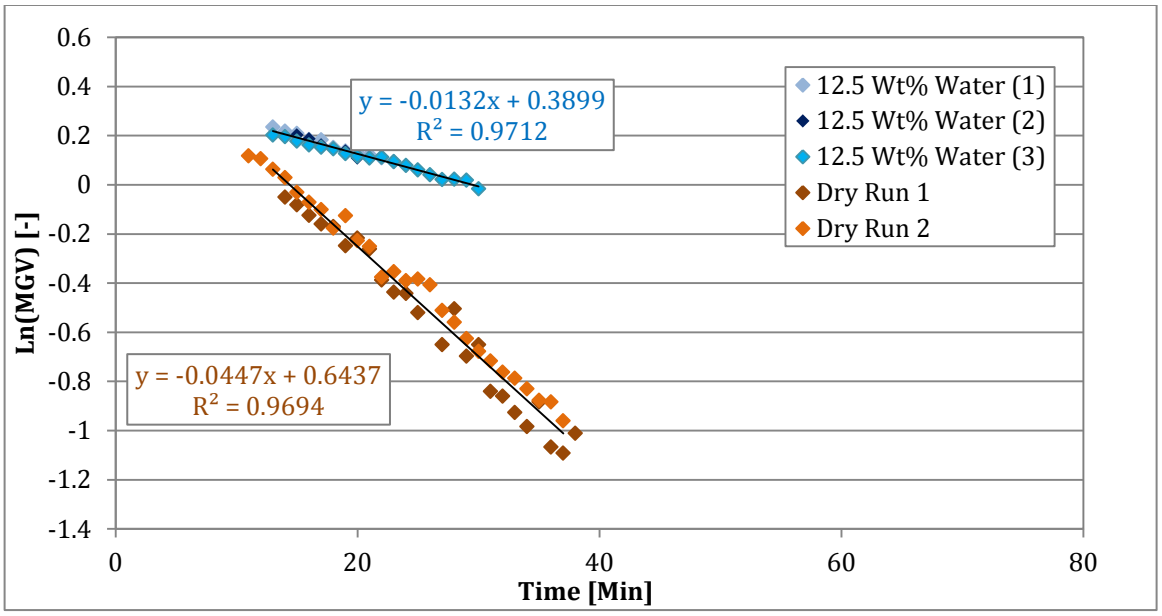

Figure 4.83: MGV comparison of Athabasca VR at 435°C with aquathermal conditions of 12.5 wt% water initially pressurized with 2 MPa nitrogen and estimated 8.7 MPa at 435 °C

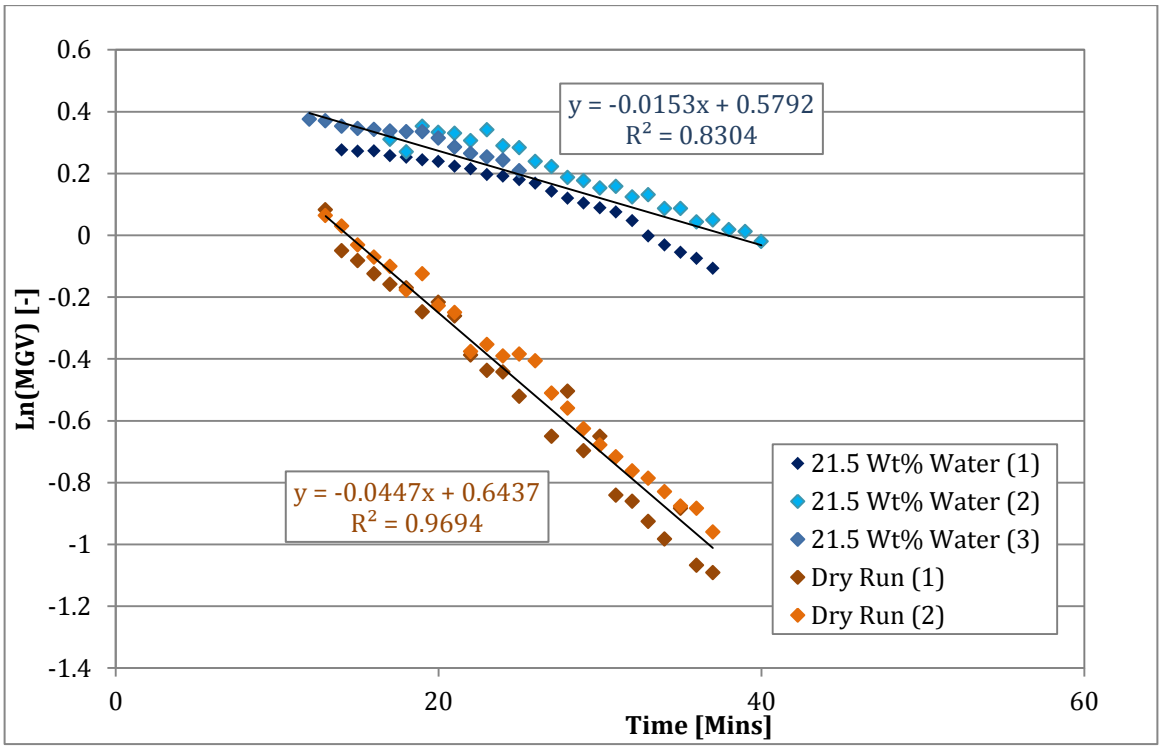

Figure 4.84: MGV comparison of Athabasca VR at 435°C with aquathermal conditions of 21.5 wt% water initially pressurized with 2 MPa nitrogen and estimated 12.3 MPa at 435 °C

Based on Figures 4.83 and 4.84 it is seen that the slope of the aquathermal experiments are reduced. This observation suggests that before the onset of any fouling behavior, the cracking kinetics of the cases with water appear to be hindered relative to dry experiments. One possible explanation for this observation is mentioned by Kruse and Dingus [59] who proposed that dissolved water in the liquid phase can reduce concentration of reactants, thus hindering reaction rates. No further analysis was conducted to determine kinetics parameters as the analysis described earlier in this chapter requires data at several temperatures for analysis.

Section 4.5.2 Aquathermal Experiments with Laser Backscattering

Aquathermal experiments similar to those presented in Section 4.5.1 were carried out using the laser backscattering setup. The depolarization ratio was normalized using the same procedure previously described in Section 4.2.1.2. Graphs of the results are given in Figure 4.85 and Figure 4.86 for lower and higher water loadings respectively. The green lines in both figures represent experiments with no added water.

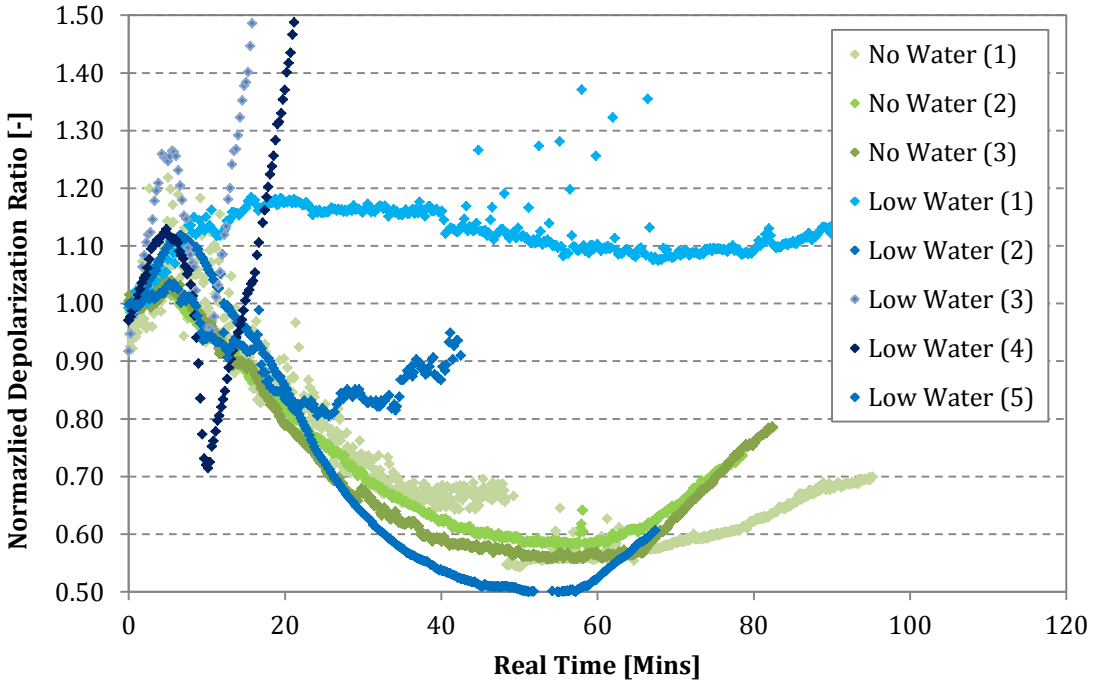

Figure 4.85: Aquathermal depolarization results of Athabasca VR at 435 °C at a water loading of 12.5 wt% with estimated pressure of 8.7 MPa

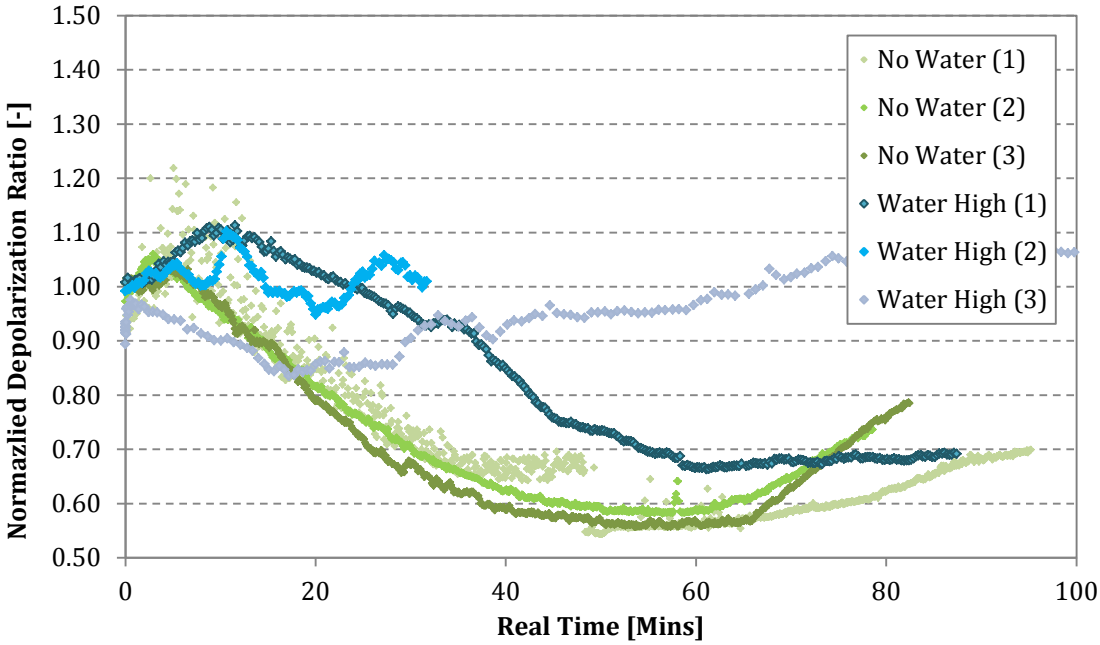

Figure 4.86: Aquathermal depolarization results of Athabasca VR at 435 °C at a water loading of 23.9 wt% with estimated pressure of 12.4MPa

As explained previously, the depolarization ratio is an indication of the amount of backscattering detected. Typically, the depolarization ratio curve increases during heating as the thermal energy increases the amount of scattering. Once cracking temperatures have been reached, the DPR will reach a maximum before starting to decrease. The decrease in DPR occurs during asphaltenes oligermization into larger domains. The decrease in DPR continues to occur until sufficient time has elapsed to allow for the polymerized materials to reorganize itself into an anisotropic structure. Mesophase structures are associated with strong scattering properties and slow the depolarization ratio dropping rate upon their appearance.

Results in Figure 4.85 compare experiments with no added water against experiments containing 12.5 wt% water, at 2 MPa of nitrogen initially. Using VMGSim it was determined the system reaches 8.7 MPa at reaction temperature. Although both dry and wet of tests follow the depolarization curve shape description above, the time it takes for the mesophase onset appears to be sporadic for water experiments. Triplicates of trials with no added water all reach a minimum depolarization ratio at approximately 54 minutes. In contrast, the

aquathermal tests have depolarization minimums that appear over a wide range of times varying from 9 to 66 minutes. Several experiments with higher water loadings were also tested with results illustrated in Figure 4.86. Again DPR curves show that DPR minimums were reached over a large time span. Thus, it was concluded that the use of laser-based DPR monitoring of heavy oil cracking in aquathermal conditions was ineffective since it resulted in sporadic mesophase onset behavior.

The seemingly stochastic mesophase onset behavior can be explained through examination of the area coverage by the laser focal point. The laser has a relatively small focal point area of approximate 0.07 mm^2, when compared to the cross-polarized microscope that has a much larger coverage of 5 mm^2. The substantially smaller coverage by the laser can result in the reporting of skewed data in the event any fouling on the window. In the event where the focal point of the laser is directed at a point where a dark patches materializes, the DPR will report an earlier onset. Thus, the results reported by the laser setup are position dependent. This explanation accounts for seemingly random behavior that is observed by the laser setup.

Section 4.5.3 Aquathermal Onset Times

One objective of conducting aquathermal experiments was to investigate the effect of water on mesophase onset times. This was completed by the direct examination of the micrographs. Since aquathermal experiments result in dark film fouling, both onset times of the dark films and mesophase are reported. Summarized in the Table 4.14 are the experimental conditions tested with their corresponding VMG estimated pressure. As a reminder, the estimated pressure only accounts for the thermodynamic equilibrium and not for any gaseous products that are the result of any reactions.

Table 4.13 Aquathermal experimental conditions

Water Loading	Initial Nitrogen Pressure	Estimated Pressure at 430°C	Number of Replicates
[wt%]	[MPa]	[MPa]	[-]
0	0.1	0.1	3
12.5	2	8.7	4
12.5	4	12.2	4
21.4	2	12.3	3

Upon inspection of the micrographs, the onset times were determined and compared against tests with no added water. Mesophase and dark film onsets times are given with a 95% confidence intervals are shown in Figure 4.87. The added water reduces the mesophase onset period compared with the case with no added water. In order to examine if the mesophase onset times were significantly less than the dry experiments, one-tailed t-tests were conducted on results with results shown in Table 4.15. Using an $\alpha = 0.05$, the null hypnosis can be rejected showing that water does indeed significantly reduce the mesophase onset period. It is also interesting to note regardless of experimental conditions the mesophase onset appears approximately ten minutes after the appearance of the dark film.

Table 4.14: P-values of dry vs. aquathermal runs

Water Loading	Initial Nitrogen Pressure	Average Mesophase Onset Time	P-Value
[wt%]	[MPa]	[min]	[-]
0	0.1	56.6	n/a
12.5	2	31.0	7.2e-3
12.5	4	36.3	4.8e-3
21.4	2	40.3	4.3e-3

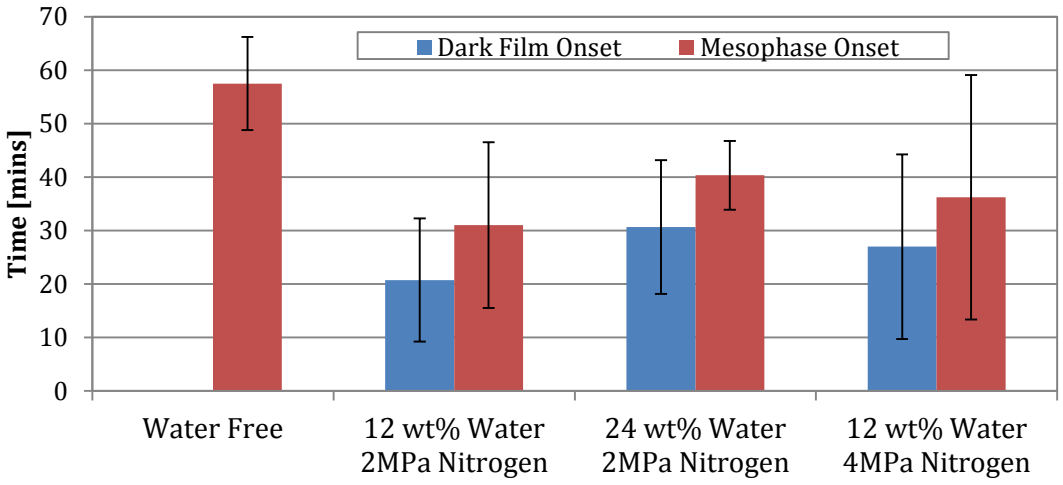

Figure 4.87: Dark film and mesophase onset of Athabasca VR at 435 °C

Results presented above seem inconsistent with most literature findings. As reported in by many authors, the addition of water can result in a solvent or dispersion effect. Both of which are beneficial to the cracking as it results in lower viscosity products as well as the delay in coke onset. One possible explanation between this study and the reports in the literature by other research groups is that those studies examined water concentrations that often exceed 50 wt%. Differences in water concentration, however, is not likely to be the only explanation as even at much lower concentrations Nhieu reported that water had no significant effect on coke onset [68]. The key difference is that Nhieu's work is centered around coke while this work is focused on mesophase. Although mesophase is a precursor to coke and there are similarities between the two, the behaviors of the substances are expected not to be identical.

Regardless, there is still large variability seen in the results as reflected in the confidence intervals. A possible explanation for this is the poor stirring apparatus used for this investigation leading to inconsistent reactor hydrodynamics. These inconsistences may play a large role especially when dealing with systems with dark film deposits. Additionally, even with stringent cleaning procedures there is always a possibility for cross contamination providing nucleation sites for mesophase formation. Furthermore the sapphire window damage from prolonged usage, or

coke build up that cannot be removed may also result in nucleation sites. As such it is recommended that more experiments be carried out.

In summary, thermal cracking of Athabasca vacuum residue was conducted with water at subcritical conditions. Before experiments were conducted, simulation work in COMSOL was completed to ensure cold sinks in the system would not result in significant water condensation. VMG Simulation was used to predict reacting pressures, it should be noted that pressures predicted are higher than experimental pressure obtained for trials on the Parr reactor. In addition to condensing surfaces in the Parr reactor, the property package in the simulation may not adequately capture intermolecular forces while also under-predicting water and nitrogen solubility in the liquid phase.

Added water to Athabasca VR results in the introduction of dark film fouling. Results also indicate that reaction kinetics in the homogeneous reaction stage is hindered relative to tests where no water was added. The dark film fouling also renders the laser backscattering setup unhelpful as the laser focal point on this experimental apparatus is too small. Finally, the addition of water also was seen to reduce mesophase onset periods.

Chapter 5 : Conclusions and Recommendations

Section 5.1 Conclusions

This study setted out to study heavy oil cracking by applying backscattering techniques. A combination of polarized hot stage microscopy and laser backscattering has allowed for the investigation of low conversion cracking kinetics of several different heavy oil feeds with the following results:

- As heavy oil is upgraded its chemical composition changes which causes changes in scattering properties. The parameters that are used to monitor the amount of scattering for the microscopy and laser setups are the MGV and DPR respectively.
- Three stages were identified for MGV and DPR curves:
    - Heating stage where both the MGV and DPR are observed to increase with increasing temperature
    - Homogenous reaction stage where the MGV and DPR are seen to decrease
    - Heterogeneous reaction stage when the onset of fouling behavior has been observed
- The fouling behavior of oils is dependent on feed composition. Two types of fouling behavior were distinguished:
    - Mesophase fouling where appearance of bight mesophase domains is observed optically. Mesophase fouling is observed with all feeds studied given sufficient time for reaction.
    - Dark film fouling where the bulk oil phase formed patchy deposits before the formation of mesophase as exhibited by the Gudao and Columbian oils.
- Severity factor which is a parameter that reports the time-temperature history of a reaction can be used to elute the activation energy. Activation energy was determined by converting real time of a reaction at a given

temperature into an equivalent severity index at a reference temperature. Two optimization methods were proposed to determine the activation energy.

  - By collapsing the MGV or depolarization curves into a single regressed line and varying the activation energy until the best fit is obtained.
  - Alternatively, varying both the activation energy and normalization factors to minimize standard deviation of the slopes of the MGV or depolarization curves.

- It was determined that during the homogeneous reaction stage the MGV falls under a first order kinetic regime and the DPR is best modeled by a second order kinetic model.
- The activation energy determined by both methods of analysis generated results that are within reasonable values reported in the literature.
- Mesophase onset times decrease with increasing temperatures.

Both experimental apparatuses which were also used to study the effect of water on Athabasca VR determined that:

- The addition of water to Athabasca VR results in phase instability that changes its fouling behavior by the introduction of film fouling.
- Laser backscattering should not be used for systems that exhibit film fouling as the focal coverage of the laser is too small that causes the results to become position dependent.
- Mesophase onset times are reduced when compared to experiments with no added water.
- The difference in dark film and mesophase onset times appear to be consistent regardless of the reaction condition tested.

SECTION 5.2 RECOMMENDATIONS AND FUTURE WORK

The current work is not without its limitations, several improvements are recommended for future work:

- Improvement of the stirring mechanism to reach turbulent conditions that will allow for better mixing and subsequently more consistent reactor hydrodynamics.
- More stringent procedures and studies should be implored to gain a deeper understanding of light artifacts of the microscope and backscattering intensity for the laser and the microscope. The intention of this recommendation is for attaining stable results that do not need to be normalized to account for run-to-run variability.
- An investigation into temperature effects on scattering at temperatures above cracking temperatures is suggested for better temperature normalization.
- A limited amount of data is available for onset times due to time constrains resulted in poor statistical analysis. It is highly recommended that additional replicates be completed for both aquathermal conditions as well as the kinetics works.
- It is recommended that other image analysis methods be developed. One example is to use the RGB values separately rather than average them into the MGV. It is also possible to use other color models such as hue-saturation-lightness (HSL) or hue-saturation-value (HSV) rather than RGB values. These models may reveal other artifacts in the data relative to MGV. For even more advance image processing, the use of color histograms maybe applied. RGB values are considered to be the average of theses histograms; as such the use of such information may be useful when examining particle distributions.
- Additional testing is recommended to examine the role of florescence and its significance during the laser backscattering experiments

BIBLIOGRAPHY

[1] U. E. I. Administration, "International Energy Outlook 2013," U.S. Department of Energy, Washington D.C., 2013.

[2] Canada's Oil and Natrual Gas Producers, "Crude Oil Forcast, Market & Transportation," Canadian Association of Petroleum Produces, Calgary, 2014.

[3] M. R. Gray, Upgrading Oilsands Bitumen and Heavy Oil, Edmonton: Univerity of Alberta Press, 2014.

[4] A. de Klerk and E. Furimsky, Catalysis in the Refininf of Fischer-Tropsch Syncrude, Royal Society of Chemistry, 2010.

[5] D. K. Yang and S. T. Wu, Fundamental of Liquid Crystal Devices, West Sussex: John Wiley & Sons, Limited, 2006.

[6] S. R. Bagheri, "Mesophase Formation in Heavy Oil," Department of Chemical and Materials Engineering , Edmonton , 2012.

[7] Z.-M. Cheng, Y. Ding, L.-Q. Zhao, P.-Q. Yuan and W.-K. Yuan, "Effects of Supercritical Water in Vacuum Residue Upgrading," *Energy & Fuels,* vol. 23, pp. 3178-3183, 2009.

[8] J. G. Speight, "Chapter 2: Chemical and Physical Studies of Petroleum Asphaltenes," *Developments in Petroleum Science,* vol. 40 , no. Part A, pp. 7-65, 1994.

[9] V. Calemma, P. Iwanski, M. Nali, R. Scotti and L. Montanari, "Structural Characterization of Asphaltenes of Diffrent Origins," *Energy 5 Guels ,* vol. 9, pp. 225-230, 1995.

[10] Z. Liao, J. Zhao, P. Creux and C. P. Yang, "Discussion on the Structural Features of Asphaltene Molecules," *Energy Fuels,* vol. 23, no. 12, pp. 6272-6274, 2009.

[11] A. Karimi, K. Qian, W. N. Olmstead, H. Freund, C. Yung and M. R. Gray, "Quantitative Evidence of Bridged Structures in Asphaltenes by Thin Film Pyrolysis," *Energy & Fuels,* vol. 25, no. 8, pp. 3581-3589, 2011.

[12] H. Groenzin and O. C. Mullins, "Molecular Size and Structure of Asphaltenes from Various Sources," *Energy and Fuels,* vol. 14, no. 3, pp. 677-684, 2000.

[13] J. M. Sheremata, M. R. Gray, H. D. Dettman and W. C. McCaffrey, "Quantitative Molecule Representation and Sequential Optimization of Athabasca Asphaltenes," *Energy & Fuels ,* vol. 18, no. 5, pp. 1377-1384, 2004.

[14] M. R. Gray and W. C. McCaffrey, "Role of Chain Reactions and Olefin Formation in Cracking, Hydroconversion, and Coking of Petroleum and Bitumen Fractions," *Energy & Fuels,* vol. 16, no. 3, pp. 756-766, 2002.

[15] P. D. Clark and M. J. Kirk, "Studies on the Upgrading of Bituminous Oils with Water and Transition Metal Catalysts," *Energy and Fuels,* vol. 8, pp. 380-387, 1994.

[16] H. P. Bolch, Compressors and Modern Process Applications, John Wiley & Sons, 2006.

[17] J. J. Colyar, E. Peer, S. Kressmann and F. More, "H-Oil Process Based Heavy Crudes Refining Schemes".

[18] C. L. Thomas, "Chapter 24: Petroeum Coke and Coking," in *Progress in Petroleum Technology*, American Chemical Society: Division of Petroleum Chemistry , 1951, pp. 278-286.

[19] S. J. Abedi, S. Seyfaie and J. M. Shaw, "Unusual Retrograde Condensation and Apshaltene Precipitation in A Model Heavy Oil System," *Petoroleum Science and Technology,* vol. 16, no. 3&4, pp. 209-226, 1998.

[20] I. A. Wiehe, "A Phase-Separation Kinetic Model for Coke Formation," *Industiral & Engineering Chemistry Research,* vol. 32, no. 11, pp. 2447-2454, 1993.

[21] J. D. Brooks and G. H. Taylor, "The Formation of Graphtizing Carbon from the Liquid Phase," *Carbon,* vol. 3, pp. 185-193, 1965.

[22] K. W. Hutchenson, J. R. Roebers, G. Z. Liu, J. C. Mullins and M. C. Thies, "Chpater 28: Production of Mesophase Pitch by Supercritial Fluid Extraction," in *Supercritical Fluid Engineering Science*, American Chemical Society, 1992, pp. 347-362.

[23] F. Reinitzer, "Beiträge zur Kenntnis des Cholesterins," *Monatshefte für Chemie ,* vol. 9, p. 421, 1888.

[24] P. J. Collings, Liquid Crystals: Nature's Delicate Phase of Matter, Princeton: Princeton University Press, 2002.

[25] T. Schneider, K. Artyushkova, J. E. Fulghum, L. Broadwater, A. Smith and O. D. Lavrentovich, "Oriented Monolayers Prepared from Lyotropic Chromonic Lyotropic Chromonic," *Langmuir,* vol. 21, no. 6, pp. 2300-2307, 2005.

[26] J. Corcoran, S. Fuller, A. Rahman, N. Shinde , G. J. T. Tiddy and G. S. Attard, "Amphitropic liquid crystals. Part 1.—Effect of a thermotropic mesogen on lyotropic mesomorphism, and of a surfactant on thermotropic mesomorphism. The C16EO8–5-CB–water system," *Journal of Materials Chemistry,* vol. 2, pp. 695-702, 1992.

[27] I. Dierking, "Chapter 5. The Nematic and Cholesteric Phases," in *Textures of Liquid Crystals*, Manchester , Wiley-VCH, 2004, pp. 51-74.

[28] M. Born and E. Wolf, Principleso of Optics: Electromagnetic Theory of Propagation, Interference and Diffractino of Light Fourth Ed., Oxford: Pergamon Press, 1970.

[29] R. Dabrowski, P. Kula and J. Herman, "High Birefringence Liquid Crystals," *Crystal ,* vol. 3, no. 3, pp. 443-482, 2013.

[30] C. Ai and J. C. Wyant, "Testing Stress Birefringence of an Optical Window," in *Proc. SPIE Vol. 1531 Advance Optical Manufacturing and Testing II*, 1991.

[31] S. R. M. Robertson, "Measuring Birefringence Properties using a Wave Plate and an Analyzer," *Applied Optics,* vol. 22, no. 14, pp. 2213-2216, 1983.

[32] K.-C. Lim and J. T. Ho, "Apparatus for High-Resolution Birefringence Measurement in Liquid Crystals," *Molecular Crystal and Liquid Crystals,* vol. 58, no. 3-4, pp. 173-177, 1978.

[33] H. C. van de Hulst, Light Scattering by Small Particles, New York: Dover Publications, Inc., 1957.

[34] M. I. Mishchenko and J. W. Hovenier, "Deploarization of Light Backscattered by Randomly Oriented Nonsphrical Particles," *Optics Letters,* vol. 20, no. 12, pp. 1356-1358, 1995.

[35] L. M. Cameron, "The Depolarization of Light Scattered from Liquid Crystals," *Molecular Crystals,* vol. 7, no. 1, pp. 235-252, 1969.

[36] R. S. Bagheri, M. R. Gray, J. M. Shaw and W. C. McCaffrey, "In Situ Observation of Mesophase Formation and Coalescence in Catalytic Hydroconversion of Vacuum Residue Using a Stirred Hot- Stage Reactor," *Energy and Fuels,* vol. 26, pp. 3167-3178, 2012.

[37] R. S. Bagheri, M. R. Gray and W. C. McCaffrey, "Depolarized Light Scattering for Study of Heavy Oil and Mesophase Gormation Mechanisms," *Energy and Fuels,* vol. 26, pp. 5408-5420, 2012.

[38] H. Marsh, "Carbonization and Liquid-Crystal (Mesophase) Development: Part1. The Significance of the Mesopahse during Carbonization of Coking Coals," *Fuel,* vol. 52, pp. 205-212, 1973.

[39] R. H. Hurt and Y. Hu, "Thermodynamics of Carbonaceous Mesophase," *Carbon,* vol. 37, pp. 281-292, 1999.

[40] M. Shishido, S. Yamada, K. Arai and S. Saito, "Application of liquid crystal theory to the estimation of mesophase pitch phase-transition behavior," *Carbon,* vol. 35, no. 6, pp. 797-799, 1997.

[41] Y. Hu and R. H. Hurt, "Thernodynamics of Carbonaceous Mesophase II. General throy for Nonideal Solutions," *Carbon 39,* vol. 39, pp. 887-896, 2001.

[42] T. Gentzis, P. Rahimi, R. Malhotra and A. S. Hirschon, "The Effect of Carbon Additives on the Mesophase Inudction Period of Athabasca Bitumen," *Fuel Processing Technology,* vol. 69, pp. 191-203, 2001.

[43] J. Chang, L. Fan and K. Fujimoto, "Enhancement Effect of Free Radical Initiator on Hydro-Thermal Cracking of Heavy Oil and Model Compound," *Energy & Fuels,* vol. 13, pp. 1107-1108, 1999.

[44] H. H. Al-Soufi, Z. F. Savaya, H. K. Mohammed and I. A. Al-Azawi, "Thermal Conversion (Visbreaking) of Heavy Iraqi Residue," *Fuel,* vol. 67, pp. 1714-1715, 1988.

[45] S. D. Carlo and D. Janis, "Composition and Visbreakaility of Petroleum Residues," *Chemical Engineering Science,* vol. 47, no. No.9-11, pp. 2695-2700, 1992.

[46] R. Krishna, Y. K. Kuchhal, G. S. Sarna and I. D. Singh, "Visbreaking studies on Aghajari Long Residue," *Fuel,* vol. Vol. 67, pp. 379-383, 1988.

[47] J. Xiao, L. Wang and Q. Chen, "Modeling for Product Distribution in Thermal Conversion of Heavy Oil," *Petroleum Science and Technology,* vol. 20, no. 5, pp. 605-612, 2002.

[48] D. M. Trauth, M. Yasar, M. Neurock, A. Nigam and M. T. Klein, "Asphaltene and Resid Pyrolsis: Effect of Reactio Environment," *Fuel Science and Technology International,* vol. 10, no. 7, pp. 1161-1179, 1992.

[49] M. Yasar, D. M. Trauth and M. T. Klein, "Asphaltene and Resid Pyrolysis 2: The Effect of Reactino Environment on Pathwats and Selectivities," *Energy Fuels,* vol. 15, no. 3, pp. 504-509, 2001.

[50] K. L. Kataria, R. P. Kulkarni, A. B. Pandir, J. B. Joshi and M. Kumar, "Kinetic Studies of Low Severity Visbreaking," *Industiral Enginnering Chemistry Res.,* pp. 1373-1387, 2004.

[51] J. Singh, M. M. Kumar, A. K. Saxena and S. Kumar, "Reaction Pathways and Product Yeilds in Mild Thermal Cracking of Vacuum Residues: A Multi-Lump Kinetic Model," *Chemical Engineering Journal ,* vol. 108, pp. 239-248, 2005.

[52] T. Takatsuka, R. Kajiyama, H. Hasimoto, I. Matsuo and S. Miwa, "A practical Model of Thermal Cracking of Residual Oil," *Journal of Chemical Engineering of Japan,* vol. 22, pp. 304-310, 1989.

[53] Z. L. Zhou, S. Z. Chen and C. L. Li, "A Predictive Kinetic Model for Delayed Coking," *Petroleum Science and Technology,* vol. 25, no. 12, pp. 1539-1548, 2007.

[54] J. Shardbahr, L. Khosravani and F. Khorasheh, "Developement of a continuous kinetic model for visbreaking reactions," *Scientia Iranica,* vol. 18, no. 3, pp. 465-469, 2011.

[55] D. Montane, R. P. Overend and E. Chornet, "Kinetic Models for Non-Homogeneous Complex Systems with a Time-Dependent Rate Constant," *The Canadian Journal of Chemical Engineering ,* vol. 76, pp. 58-68, 1998.

[56] K. Heger , Uematsu and E. U. Franck, "The Static Dielectric Constant of Water at High Pressures and Temperatures to 500 MPa and 550°C," *Berichte der Bunsengesellschaft für physikalische Chemie,* vol. 84, no. 8, pp. 785-762, 1980.

[57] J. Griswold and J. E. Kasch, "Hydrocarbon-Water Solubilities at Elevated Temperatures and Pressures," *Industiral and Engineering Chemistry,* vol. 34, no. 7, pp. 804-806, 1942.

[58] M. J. Amani, M. R. Gray and J. M. Shaw, "Volume of mixing and solubility of water in Athabasca bitumen at high temperature and pressure," *Fluid Phase Equilibria,* vol. 358, no. 25, pp. 203-211, 2013.

[59] A. Kruse and E. Dinjus, "Hot Compressed Water as Reaction Medium and Reactant Properties and Synthesis Reactions," *Supercritical Fluids ,* vol. 39, pp. 362-380, 2007.

[60] L.-N. Han, R. Zhang and J.-C. Bi , "Upgrading of coal-tar pitch in supercritical wate," *Journal of Fuel Chemiistry and Technology,* vol. 36, no. 1, pp. 1-5, 2008.

[61] L.-Q. Zhao , Z.-M. Cheng, Y. Ding, P.-Q. Yuan, S.-X. Lu and W.-K. Yuan, "Experimental Study on Vacuum Residuum Upgrading through Pyrolysis in Supercritical Water," *Energy & Fuels,* vol. 20, pp. 2067-2071, 2006.

[62] L. Schleep, M. Elie, P. Landais and M. A. Romero, "Pyrolysis of Asphalt in the Presence and Absence of Water," *Fuel Processing Technology,* vol. 74, p. 2001, 107-123.

[63] M. Morimoto, Y. Sugimoto, Y. Saotome, S. Sato and T. Takanohashi, "Effect of Supercritical Water on Upgrading Reaction of Oil Sand Bitumen," *Supercritical Fluids,* vol. 55, pp. 223-231, 2010.

[64] M. Morimoto, Y. Sugimoto, S. Sato and T. Takanohashi, "Bitumen Cracking in Supercritical Water Upflow," *Energy & Fuels,* vol. 28, no. 2, pp. 858-861, 2013.

[65] T. Sato, T. Adschiri, K. Arai, G. L. Rempel and F. T. T. Ng, "Upgrading of asphalt with and without partial oxidation in supercritical water," *Fuel ,* vol. 82, pp. 1232-1239, 2003.

[66] T. Sato, T. Tomita, P. H. Trung, N. Itoh, S. Sato and T. Takanohashi, "Upgrading of Bitumen in the Presence of Hydrogen and Carbon Dioxide in Supercritical Water," *Fuel,* vol. 27, pp. 646-653, 2013.

[67] A. A. Gregoli, U. M. Oko and L. Frederic , "Process for Converting Heavy Crudes, Tars, and Bitumens to Lighter Products in the Presence of Brine at Supercritial Conditions". United Sates of America Patent 4,818,370, 4 April 1989.

[68] P. Nhieu, "Role of Water and Fine Solids in Onset of Coke Formation During Bitumen Cracking," Department of Chemical and Materials Engineering, Edmonton, 2014.

[69] J. B. Wachtman and L. H. Maxwell, "Strength of syntheic single crystal sapphire and ruby as a function of temperature and oientation," National Bureay of Standards , Washington D.C., 1959.

[70] A. Bazyleva, M. Becerra, D. Stratiychuk-Dear and J. M. Shaw, "Phase behavior of Safaniya vacuum residue," *Fluid Phase Equilibria ,* vol. 380, no. 25, pp. 28-38, 2014.

[71] Z.-X. Wang, A.-J. Guo and G.-H. Que, "Coke Formation and Characterizatio During Thermal Treatment and Hydrocracking of Liaohe Vacuum Residuum," *American Chemical Society, Divsion*

of Petroleum Chemistry , vol. 43, no. 3, pp. 530-533, 1998.

[72] A. Bazyleva, M. Fulem, M. Becerra, B. Zhao and J. M. Shaw, "Pase Behaviour of Athabasca Bitumen," *Chemicnal & Eningeering Data,* vol. 56, no. 7, pp. 3242-3253, 2001.

[73] S. Peramanu, B. B. Pruden and P. Rahimi, "Molecular Weight and Specfific Gravity Distributinos for Athabasca and Cold Lake Bitumens and Their Saturates, Aromatics, Resin and Asphaltene Fraction," *Industrial & Engineering Chemistry,* vol. 36, no. 8, pp. 3121-3130, 1999.

[74] S. Acevedo and P. Rodriguez, "An electron microscopy study of crude oils and maltenes," *Energy & Fuels,* vol. 18, no. 6, pp. 1757-176, 2004.

[75] A. M. Benito, M. T. Martinez, I. Fernandez and J. L. Miranda, "Visbreaking of an asphaltenic coal residue," *Fuel ,* vol. Vol. 74, no. 6, pp. 922-927, 1995.

[76] J. G. Speight and B. Ozum, Petroleum Refining Processes, New York: CRC Press, 2001.

[77] J. C. Geniesse and R. Reuter, "Effect of Time and Temperature on the Cracking of Oils," *Industrial and Engineering Chemistry ,* vol. 22, no. 12, pp. 1274-1279, 1930.

[78] W.-L. Huang and G. A. Otten, "Cracking kinetics of crude oil and alkanes determined by diamond anvil cell-fluorescence spectroscopy pyrolysis: technique development and preliminary results," *Journal of Organic Geochemistry,* vol. 32, pp. 817-830, 2001.

[79] C. Bombardelli, L. M. Assis and H. J. Kalinowski, "Tracking aromaticity changes in heavy hydrocarbon processing by monitoring changes in electical resistivity," *Fuel ,* vol. 89, pp. 3730-3732, 2010.

[80] S. M. Ghafelebashi Zarand, "Distributed Acitivation Energies Modeling of Athabasca Vacuum Residue Pyrolysis," University of Alberta, Edmonton, 2014.

[81] R. K. Pujala and H. B. Bohidar, "Kinetics of anisotropic ordering in Laponite dispersions induced by a water-air interface," *Physical Review E,* vol. 88, no. 5, 2013.

[82] M. T. Martinez, A. M. Benito and M. A. Callejas, "Thermal Cracking of Coal Residues: Kinetics of Asphaltene Decomposition," *Fuel,* vol. 75, no. 9, pp. 871-877, 1997.

[83] P. Thiyanarajan , J. E. Hunt, R. E. Winans, K. B. Anderson and J. T. Miller, "Temperature-Dependent Structural Change of Asphaltene in 1-Methylnapthalene," *Energy Fuels,* vol. 9, no. 5, 2003.

APPENDIX A: EXPERIMENTAL SET-UP VALIDATION

The quality of results obtained by the set-up is dependent not only the quality of the equipment but the knowledge of its limitations and shortcomings. Only then can modifications be carried out to ensure the application of such a set-up will result in high confidence results. This appendix is aimed at examining several components of the dynamic light backscattering set-up in order gain better insight on the current equipment and to verify that the equipment is able to produce reliable results.

Laser Probe Tip Positioning

The distance at which the laser should be placed before the sapphire window (d_1 in the Figure A.1) was determined using Snell's Law. The penetration depth of the laser into the pitch is shown as d_3 in Figure A.1, this distance must be smaller than depth of the pitch itself which is defined as t_p.

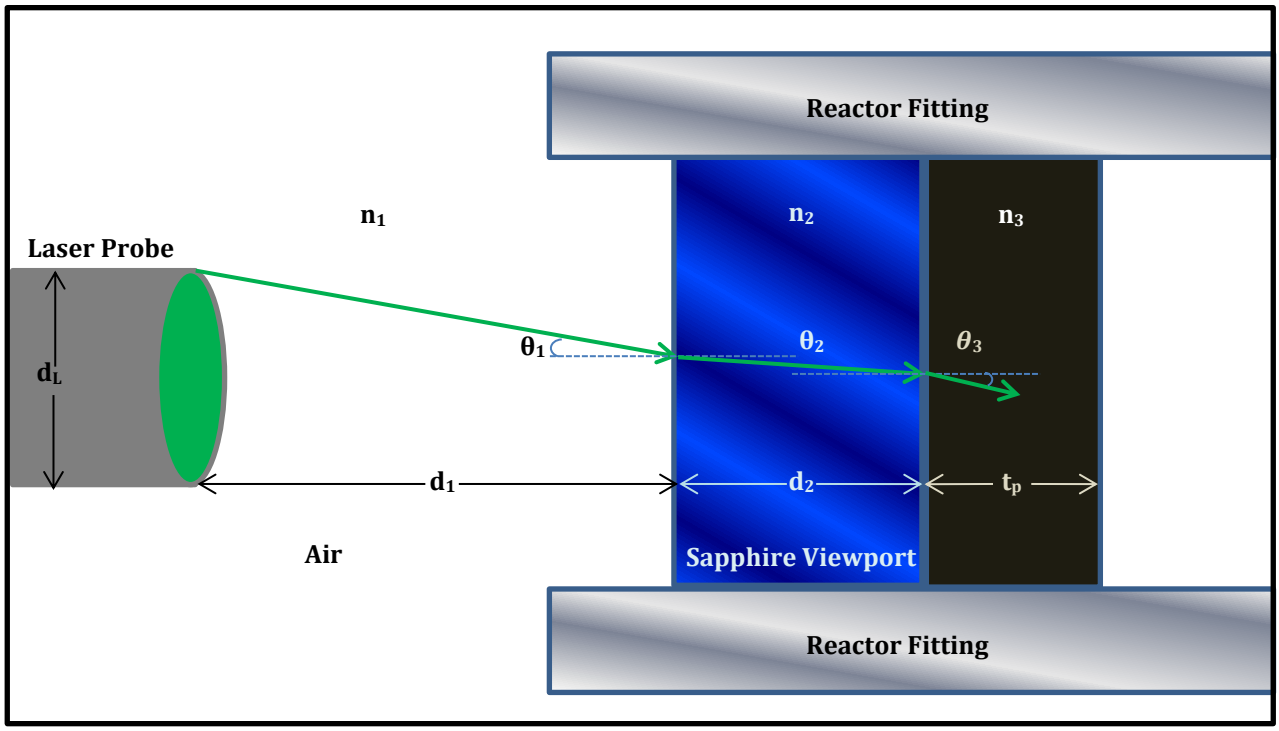

Figure A.8: Laser beam path as it passes thru the sapphire window

Although the pitch is opaque, the light is able to penetrate at shorter lengths. As such when loading the reactor the depth of the pitch must exceed this length at a minimum. However, for simplicity it will be assumed that the laser is focused immediately between the interface of the sapphire and pitch. The sapphire window thickness is also known. Depending on the window used the thickness can be 3, 4 or 5 mm.

The manufacturers specify that diameter of the probe tip (d_L) is 1.5 cm, and that the majority of the light paths converge in a spot that is 0.3mm in diameter (d_f) which is 20 mm away from the tip. Using these values the first angle of incidence (θ_1) was determined as follows:

$$tan\theta_1 = \frac{.5(d_L - d_f)}{f} = \frac{.5(15mm - 0.3mm)}{20mm} = \frac{7.35}{20} = .3675$$

$$\theta_1 = 20.17°$$

The initial angle of incidence determined by the above equation is valid as long as the probe is placed within its focal distance of 20 mm. It can also be seen that regardless of the mediums that the light travels through, the beam must move $y_{total} = 7.35$ mm vertically to converge, which is shown in Figure A.2. With θ_1 calculated it is then possible to determine the angle of the refracted ray in the sapphire window using Snell's Law. The refractive indexes for air and sapphire respectively are 1.0 and 1.77. Using these values:

$$\frac{sin\theta_1}{sin\theta_2} = \frac{n_2}{n_1} = \frac{\sin(20.17°)}{sin\,\theta_2} = \frac{1.77}{1.0}$$

$$\theta_2 = 11.23°$$

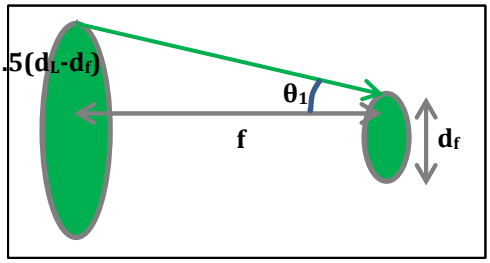

Figure A.9: Laser probe focal point

Knowing that the thickness of the window is 4 mm, the vertical distance which the light traverses while in the sapphire was determined as:

$y_2 = d_2 tan\theta_2 = 4\,mm(\tan 11.23°) = 0.79mm$

As explained the beam must vertically travel in the air:

$y_1 = y_{total} - y_2 = 7.35mm - .79mm = 6.55mm$

$$d_1 = \frac{y_1}{tan\theta_1} = \frac{6.55mm}{.3675} = 17.83mm$$

Where d_1 is the distance the probe tip should be place from the air-sapphire boundary. Of course, the thickness of the sapphire window will vary depending on applications. The following table repeats the above calculations for a range of window thicknesses where all values are reported in mm.

Table A.3: Recommended probtip distance for various window thinknesses

Window Tickness $d_2\ [mm]$	*Vertical Window Distance* $y_2\ [mm]$	*Vertical Air Distance* $y_1\ [mm]$	*Probe Tip Distance* $d_1\ [mm]$
3	0.60	6.75	18.38
4	0.79	6.56	17.84
5	0.99	6.36	17.30
6	1.19	6.16	16.76
7	1.39	5.96	16.22
8	1.59	5.76	15.68

It is also possible repeat the above calculation while assuming that the beams converge into a single point of negligible diameter. If that is the case the parameters change as follows:

$y_{total} = 7.5mm\ ;\ \theta_1 = 20.56°\ ;\ \theta_2 = 11.44°$

Using these new values, the probe tip distance is recalculated:

Table A.4: Recommended probtip distance for various window thinknesses for single point

Window Tickness $d_2\ [mm]$	*Vertical Window Distance* $y_2\ [mm]$	*Vertical Air Distance* $y_1\ [mm]$	*Probe Tip Distance* $d_1\ [mm]$
3	0.61	6.89	18.38
4	0.81	6.69	17.84
5	1.01	6.49	17.30
6	1.21	6.29	16.76
7	1.42	6.08	16.22
8	1.62	5.88	15.68

As shown by the table the probe tip distance does not vary much when assuming that the light all converges into a single point of negligible diameter.

Laser Angle Positioning

There are other factors that may also contribute to skewed results. For example it is known that sapphire exhibits birefringence, as such it is important that the laser is always perpendicular to the window or parallel to its crystal axis. In the event where it is not, the polarization state of the incoming light changes as it passes through the window resulting in a higher depolarization ratio as shown below.

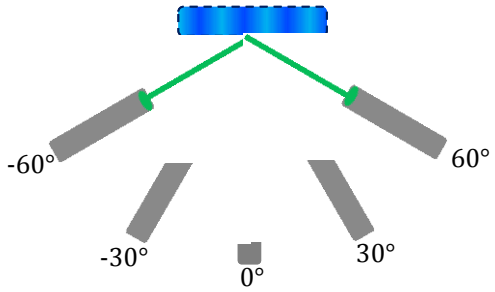

Figure A.10: Various tested angles for laser probe tip

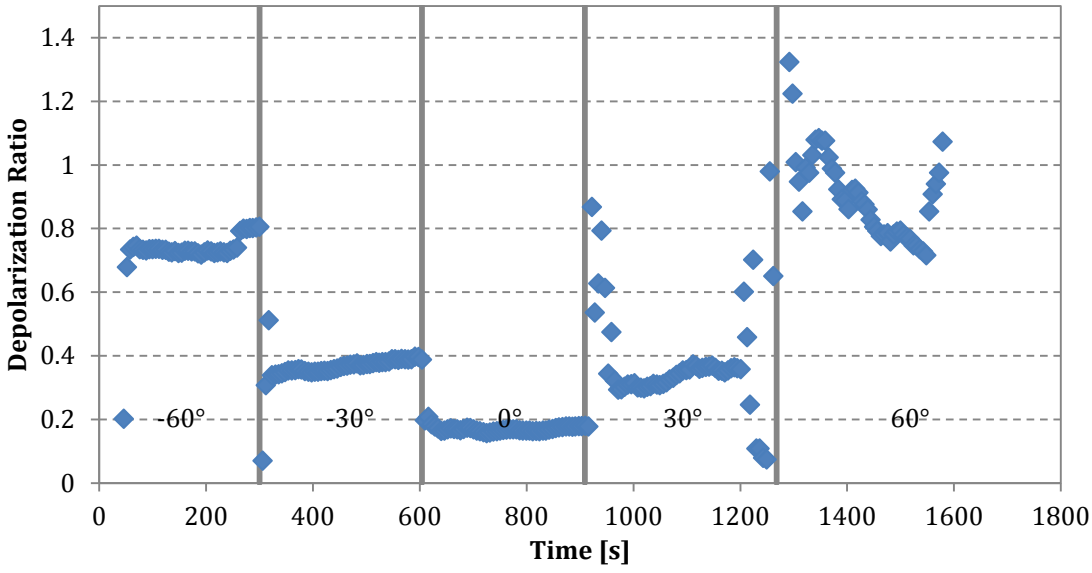

Figure A.11: Depolarization ratio at variuos probe tip angles

Power Ramp Curves

Another aspect of validation is the relationship between the power output of the supply and the actual output of the laser. Initially, it was hypothesized that the power output by the laser is proportional to the power output of the supply. However, experimental results shown in Figure A.6 show otherwise. The laser's power input was gradually increased while aiming the beam though protective eyewear, the attenuated beam then passes thru the lens on the detector. The attenuation the laser beam is required as the intensities greater than 5 W damages the detector. Using the lens with an optical density of 5, the laser's intensity is reduced by a factor of approximately 100000. Results show that the laser's intensity increases as the driver value increase to 1.0 (a dial value of 7) and then decreases until a driver value of 1.2 (a dial value of 8.5) at which the intensity of the laser continues to increase.

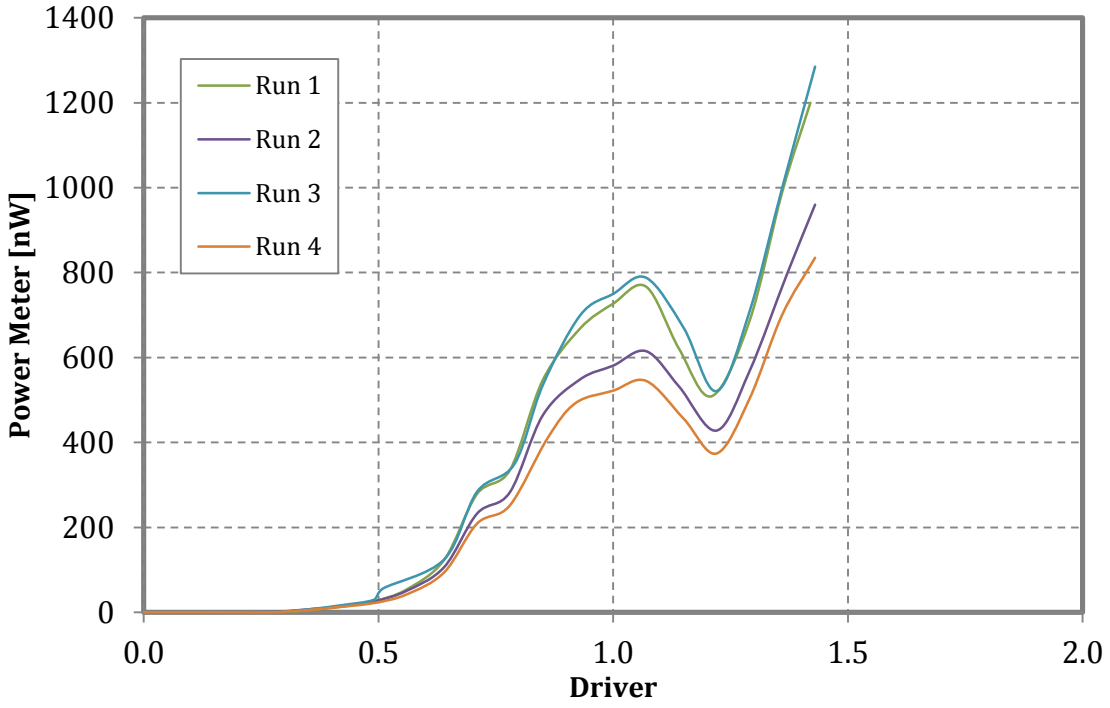

Figure A.12: Laser output intensity as a function of driver value

This phenomenon is known as a "dwell" in the power curve and occurs when the power emission of the TED cooler and the diode current are antagonistic. This contradiction can cause a plateau or an even a decline in the power emission in the laser as shown in Figure A.5. This is behavior is typical of most diode-pumped soild-state lasers (DPSSL).

Fiber Optics

Fiber optic cords are fragile and are to be handled with care. They should not be bent at sharp angles, instead they should be left slightly coiled without tension. The ends of each cord are metal connectors that can be attached to the probe or adaptors. It is essential to ensure that these ends are connected properly and tightly without causing any unnecessary tension in the cable.

Fiber optic cables were tested using the following procedure:

- The adaptor of the detector was removed and placed vertically
- The laser was placed 5.5" from the detector
- Starting on the lowest power setting the laser output was gradually increased in power until the threshold of 5mW is shown by the powermeter. It is important to not exceed this threshold as this will damage the detectors

Figure A.6 are the results obtained from testing two different optic cables. As the power driver is increased the detector readings increase accordingly. The graph indicates that this relationship is repeatable and is consistent for different cables as well. In addition, the light movement was applied to the cables near the power threshold of the detector to examine if small movement affects the readings, and no effect was found when this was carried out.

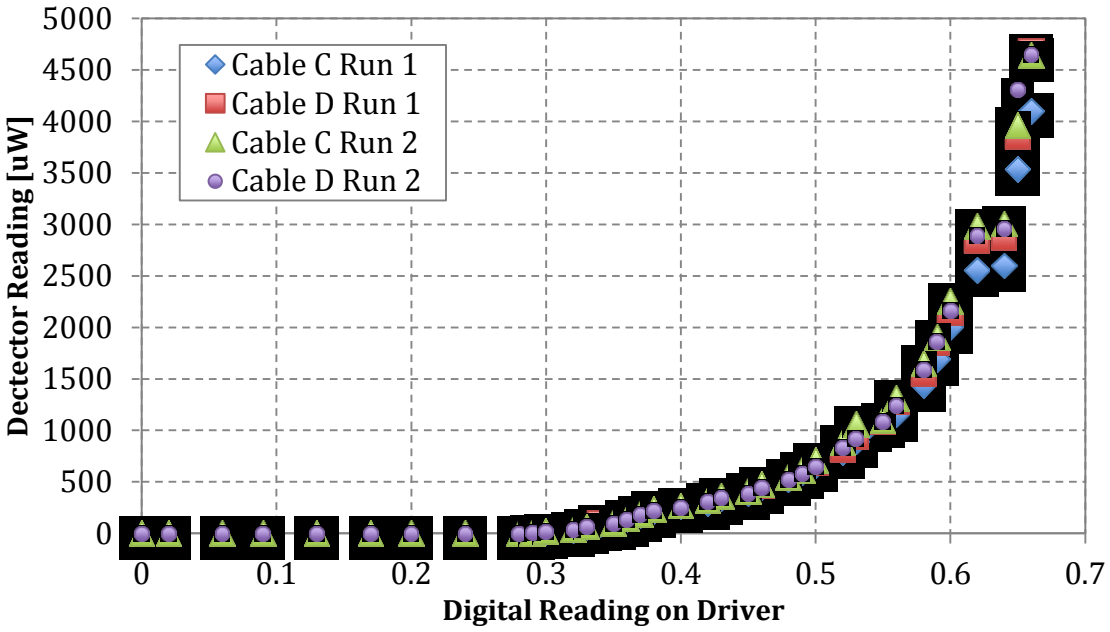

Figure A.13: Fibre optic cable testing

APPENDIX B: MICROREACTOR PARTS

This section of the appendix covers the different parts of the microreactors from Swagelok and other vendors. In the event that users need to order additional parts, part numbers are provided. Two options are presented for some of the parts shown below. The first option is for the low pressures from 0-5 MPa while the second is for operation at 5MPa-16MPa.

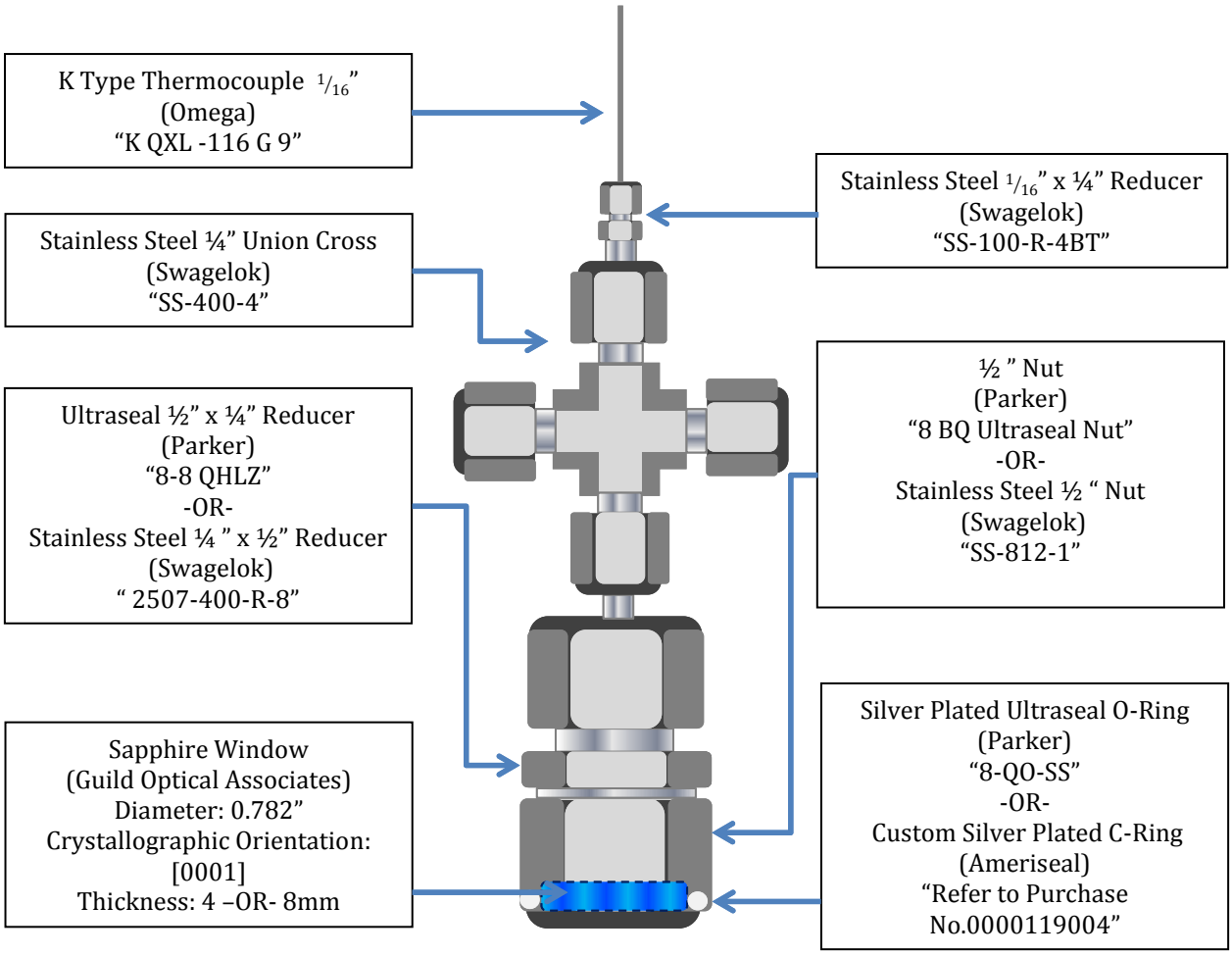

Figure A.14: Microreactor parts and their corresponding details

APPENDIX C: LOW TEMPERATURE ATHABASCA RUNS

Two other runs were also carried out on the microscope to better understand the system. Athabasca VR was also conducted at 350 °C and 370 °C and were ran for approximately five hours. The intention of running such experiments was to examine a threshold temperature at which cracking reactions start to occur. Figure A.8 is the MGV at 350 °C. It is seen that the value stabilizes after the initial decrease during the first 100 min period. The constant MGV at this point is indicative of the fact that the reaction medium is not undergoing further reactions. However, there is still an initial decrease suggesting there are possibly some reactions that are occurred initially. One possible explanation is that even at low temperatures at 350 °C, there is sufficient energy to react sulfur-carbons bonds. That is because sulfur-carbon bonds cleavage is likely to have lower activation energy than cracking reactions. Once these reactions with lower activation energy were completed the MGV reaches a constant and no longer evolves.

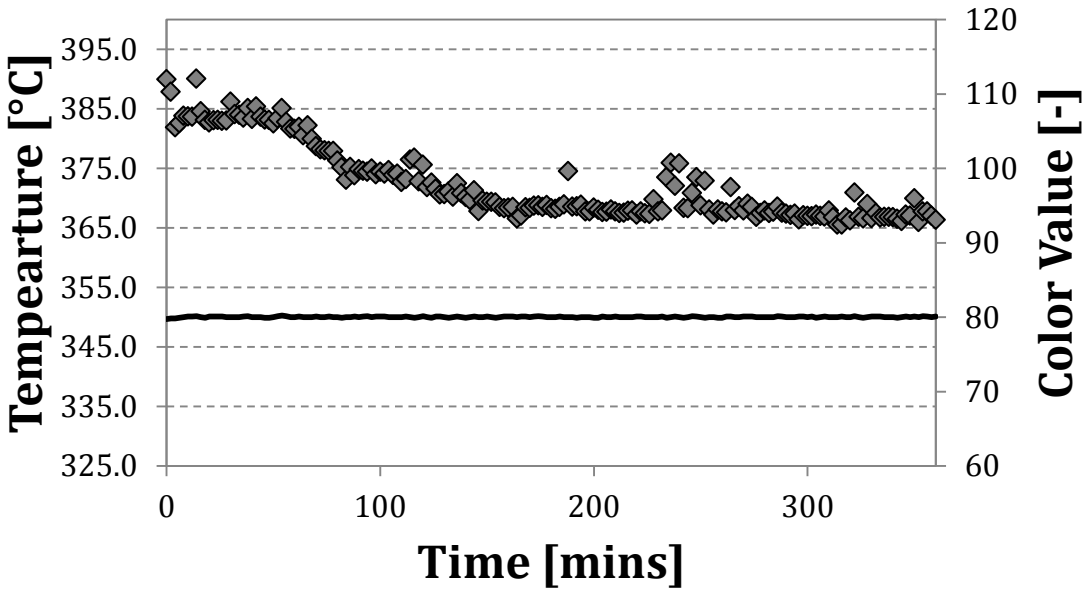

Figure A.8: Long term MGV evolution of Athabasca VR at 350 °C

Figure A.9, are results from the heating of Athabasca VR at 370 °C. At this point it can be seen that the MGV steadily declines over the 300 minuet period. This suggests that there is a cracking reactions occurring even if it is at a very slow rate.

It is concluded that even if there are reactions at this point the rate is very slow relative to the rate at the desired setpoint of 420 °C or higher, so that in the context of the heating ramp time frame it is assumed that reactions at this point are negligible.

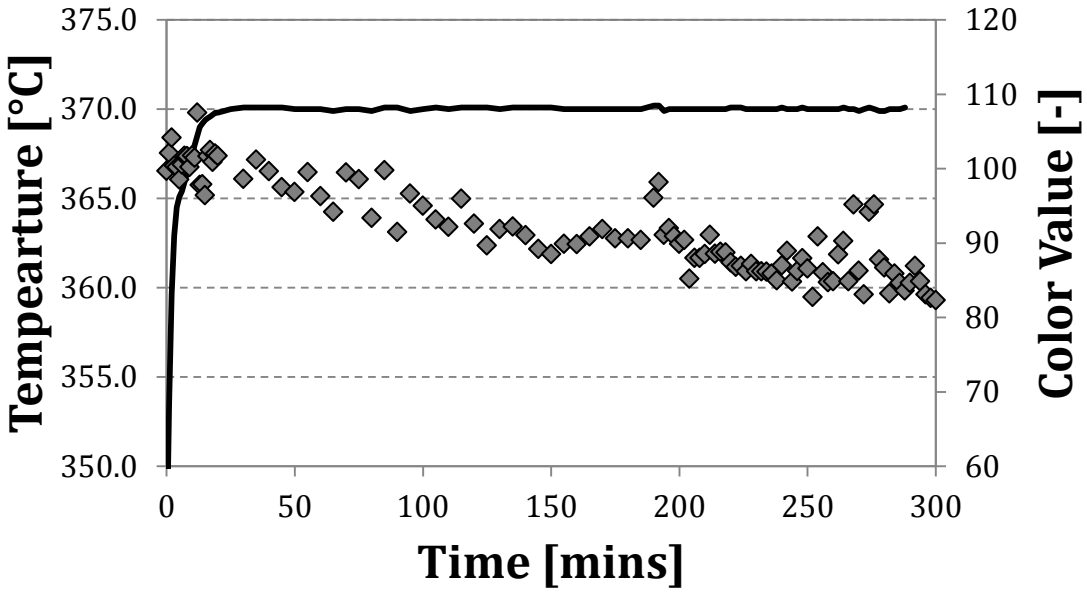

Figure A.9: Long term MGV evolution of Athabasca VR at 370 °C